

ADA037197

AFFDL-TR-76-147

(12) 8

APPLICATION OF AN ELECTRON BEAM TO HIGH DENSITY FLOWS OF N_2 , O_2 , AND NO

THE OHIO STATE UNIVERSITY
COLUMBUS, OHIO

DECEMBER 1976

TECHNICAL REPORT AFFDL-TR-76-147
FINAL REPORT FOR PERIOD APRIL 1974 - SEPTEMBER 1976

Approved for public release; distribution unlimited

DDC
RECEIVED
MAR 22 1977
A

AIR FORCE FLIGHT DYNAMICS LABORATORY
AIR FORCE WRIGHT AERONAUTICAL LABORATORIES
AIR FORCE SYSTEMS COMMAND
WRIGHT-PATTERSON AIR FORCE BASE, OHIO 45433

NOTICE

When Government drawings, specifications, or other data are used for any purpose other than in connection with a definitely related Government procurement operation, the United States Government thereby incurs no responsibility nor any obligation whatsoever; and the fact that the government may have formulated, furnished, or in any way supplied the said drawings, specifications, or other data, is not to be regarded by implication or otherwise as in any manner licensing the holder or any other person or corporation, or conveying any rights or permission to manufacture, use, or sell any patented invention that may in any way be related thereto.

This report has been reviewed by the Information Office (IO) and is releasable to the National Technical Information Service (NTIS). At NTIS, it will be available to the general public, including foreign nations.

This technical report has been reviewed and is approved for publication.

HeeneTul

HSUE-FU LEE
Project Engineer, R & D Group
Experimental Engineering Branch

FOR THE COMMANDER

Donald J. Harney

DONALD J. HARNEY
Asst For Experimental Simulation
Aeromechanics Division

NTIS	1/11/77
DOC	1/11/77
UNCLASSIFIED	
JUSTIFIED	
BY	
A	

Copies of this report should not be returned unless return is required by security considerations, contractual obligations, or notice on a specific document.

UNCLASSIFIED

SECURITY CLASSIFICATION OF THIS PAGE (When Data Entered)

9 REPORT DOCUMENTATION PAGE		READ INSTRUCTIONS BEFORE COMPLETING FORM	
1. REPORT NUMBER 18 AFDD TR-76-147	2. GOVT ACCESSION NO.	3. RECIPIENT'S CATALOG NUMBER	
4. TITLE (and Subtitle) APPLICATION OF AN ELECTRON BEAM TO HIGH DENSITY FLOWS OF N ₂ , O ₂ AND NO.		5. TYPE OF REPORT & PERIOD COVERED Final report. 1 Apr 1974 - 30 Sep 1975	
7. AUTHOR(s) S. L. PETRIE		6. PERFORMING ORG. REPORT NUMBER RF 3890	
14 O'SURF-3898		8. CONTRACT OR GRANT NUMBER(s) Contract F33615-74-C-3970 Contract F33615-76-C-3112	
9. PERFORMING ORGANIZATION NAME AND ADDRESS The Ohio State University Research Foundation 1314 Kinnear Road Columbus, Ohio 43212		10. PROGRAM ELEMENT, PROJECT, TASK AREA & WORK UNIT NUMBERS Project No. 1426 & 1926 Work Unit 19260414	
11. CONTROLLING OFFICE NAME AND ADDRESS Aeromechanics Division/FXN Air Force Flight Dynamics Laboratory Air Force Wright Aeronautical Laboratories (AFSC) Wright-Patterson Air Force Base, Ohio 45433		12. REPORT DATE December 1976	
14. MONITORING AGENCY NAME & ADDRESS (if different from Controlling Office) 12 94p.		13. NUMBER OF PAGES 92	
16. DISTRIBUTION STATEMENT (of this Report) Approved for public release, distribution unlimited.		15. SECURITY CLASS. (of this report) Unclassified	
		15a. DECLASSIFICATION/DOWNGRADING SCHEDULE N/A	
17. DISTRIBUTION STATEMENT (of the abstract entered in Block 20, if different from Report)			
19. SUPPLEMENTARY NOTES			
20. KEY WORDS (Continue on reverse side if necessary and identify by block number) Electron Beams; Molecular Nitrogen; Molecular Oxygen; Nitric Oxide; Arc Heated Wind Tunnels; Collision Quenching.			
20. ABSTRACT (Continue on reverse side if necessary and identify by block number) The electron beam fluorescence technique was investigated for measuring the vibrational temperatures and number densities of molecular nitrogen, nitric oxide, and molecular oxygen at densities up to those corresponding to a static pressure of 50 torr and a temperature of 300 K. Comparative tests were conducted in a static chamber and in an arc heated wind tunnel. Wind tunnel tests were conducted with reservoir temperatures varying from 1400 K to 5500 K and test section equivalent pressures from 0.12 to 26 torr.			

DD FORM 1 JAN 73 1473 EDITION OF 1 NOV 65 IS OBSOLETE

UNCLASSIFIED

SECURITY CLASSIFICATION OF THIS PAGE (When Data Entered)

267 360

43

UNCLASSIFIED

SECURITY CLASSIFICATION OF THIS PAGE (When Data Entered)

(20)

Severe overlap of the N_2^+ first negative system by vibrational bands of the N_2 second positive system and excessive excitation by low energy particles were observed in the static test chamber at pressures above 3 torr. The band overlap and excitation by low energy particles were not observed in the wind tunnel studies. Good agreement between the measured N_2 vibrational temperatures and the results of theoretical predictions were obtained in the wind tunnel experiments, indicating that nitrogen temperature measurements can be made at densities at least as high as those investigated in these studies. Poor agreement between the measured nitric oxide vibrational band intensity ratios in the gamma system and those computed from a direct excitation-emission model was observed in the wind tunnel experiments. A new theoretical model employing vibrational transitions in the upper electronic energy state was formulated to account for this disagreement. Sensitivity experiments for observation of the O_2^+ second negative system in the wind tunnel were conducted. Operating parameters for application of electron beams at high densities were delineated.

UNCLASSIFIED

SECURITY CLASSIFICATION OF THIS PAGE (When Data Entered)

FOREWORD

This final technical report was prepared by S. L. Petrie of The Aeronautical and Astronautical Research Laboratory (AARL) of The Ohio State University Research Foundation on Contracts F33615-74-C-3070 and F33615-76-C-3112. The project engineers were R. F. Carpenter and H.F. Lee of the Air Force Flight Dynamics Laboratory, Wright-Patterson Air Force Base, Ohio.

This report covers work conducted from 1 April 1974 to 30 September 1976 under Work Unit 19260414, "Development of High Density Gas Diagnostics for Re-Entry Aerodynamics".

This report was submitted by the author on 30 September 1976 for publication as a technical report.

TABLE OF CONTENTS

	<u>Page</u>
I INTRODUCTION	1
II THEORETICAL ANALYSES	3
A. MOLECULAR NITROGEN	3
B. NITRIC OXIDE	5
C. QUENCHING MECHANISMS	18
III EXPERIMENTAL APPARATUS AND PROCEDURES	22
A. TEST FACILITIES	22
1. Static Chamber	22
2. Arc-Heated Wind Tunnel	24
B. INSTRUMENTATION	26
1. General	26
2. Optical System	27
3. Data Acquisition System	27
IV RESULTS AND DISCUSSIONS	29
A. STATIC CHAMBER TESTS	29
B. WIND TUNNEL STUDIES	38
1. Nominal Run Conditions	38
2. Overall Spectral Features	43
3. N ₂ Results	43
4. Nitric Oxide Results	56
5. Molecular Oxygen Results	65
C. BEAM SHAPE	67
V EFFECTS ON PREVIOUS MEASUREMENTS	72
A. MOLECULAR NITROGEN	72
B. MOLECULAR OXYGEN	72
C. NITRIC OXIDE	74
VI CONCLUSIONS	74
REFERENCES	77

LIST OF FIGURES

<u>Figure</u>		<u>Page</u>
1	Spectrometer instrument function	6
2	Theoretical and experimental band profiles for the N_2^+ first negative (0,1) and (1,2) bands	7
3	Theoretical and experimental integrated band profiles for the N_2^+ first negative (0,1) and (1,2) bands	8
4	Integrated vibrational band intensity ratios for the N_2^+ first negative (0,1) and (1,2) bands	9
5	Theoretical and experimental band profiles for the NO γ (0,4) and (1,5) bands	13
6	Vibrational band intensity ratios for the NO γ (0,4) and (1,5) bands	17
7	Nondimensional band intensity ratios for the NO γ (0,4) and (1,5) bands	19
8	Static test chamber schematic	23
9	Arc-tunnel schematic	25
10	Instrumentation schematic	28
11	Rotational structure of the N_2^+ first negative (0,0) band	30
12	N_2^+ (0,0) line-slope plots from the static chamber	31
13	N_2 rotational temperatures measured in the static test chamber	32
14	N_2^+ (0,1)/(1,2) total intensity ratios measured in the static test chamber	35
15	N_2^+ first negative (0,1) band sequence intensity measured in the static test chamber	36
16	N_2^+ (0,1)/(1,2) P-branch intensity ratios from the static test chamber	37
17	Theoretical temperature distributions	41
18a	Typical pitot pressure surveys in nozzle N1	44
18b	Typical pitot pressure surveys in nozzle N2	45

LIST OF FIGURES - (Continued)

<u>Figure</u>		<u>Page</u>
19	Spectral scans of electron beam induced emission in the arc-heated wind tunnel for nozzle N1	47
20	Spectral scans of electron beam induced emission in the arc-heated wind tunnel	48
21	N_2^+ (0,0) band rotational structure from the wind tunnel	49
22	N_2^+ (0,1) band rotational structure from the wind tunnel	50
23	Line slope plot for data of Figure 21	51
24	Measured and predicted N_2 vibrational temperatures	55
25	Ratios of measured and predicted N_2 vibrational temperatures	57
26	Comparison of measured and predicted band profiles for NO γ (0,4) and (1,5) bands	60
27	Percent difference in theoretical and experimental intensity ratios for the NO γ (0,4)/(1,5) bands	62
28	Comparisons of measured and predicted band profiles for NO γ (0,4) and (1,5) bands	63
29	Spectral scans for wind tunnel and static chamber conditions	66
30	Correlations of beam half-width	70
31	Correlation of beam half-width increment	71

LIST OF TABLES

<u>Table</u>		<u>Page</u>
I	Molecular Constants for NO _x System	11
II	Nominal Run Conditions	46
III	Run Summary - N ₂ Data	53
IV	Run Summary - Nitric Oxide Data	58
V	Previous EGF Run Summary	73

LIST OF SYMBOLS

A	Total optical transition probability
a	Empirical constant (Eq. 35)
a_f	Frozen speed of sound
B_v	Rotator constant
c	Speed of light
C_ϕ	Constant for beam excitation process
C_k	Constant for vibrational relaxation model
C_a	Constant for emission process
D_v	Centrifugal force constant
E	Energy
F	Rotational term value
G	Vibrational term value
(G)	Rotational intensity factor
$H(v_0, K', T_R)$	Rotation-vibration function (Eq. 2)
h	Planck's constant
I	Intensity
I_0	Intensity without quenching
J	Total rotational quantum number
K	Rotational quantum number
k	Boltzmann constant
k_1	Absorption coefficient
k_{10}	Vibrational transition probability
L	Beam length
M	Molecular weight
m	Particle mass
N, n, n^*	Number density

LIST OF SYMBOLS - (Continued)

n_j	Quenching density
P	Hönl-London factor
p	Vibrational transition probability or static pressure
P_{EQ}	Equivalent pressure
P_{NO}	Nitric oxide partial pressure
P_{T_2}	Total pressure behind a normal shock wave
Q	Collision cross section or partition function
q	Franck-Condon factor
$R(n^*, X_{NO})$	Rate of re-absorption
R	Universal gas constant
S	Slit width
$S_{K'}$	Rotational line strength
T	Translational temperature
v	Velocity or vibrational quantum number
$W_{1/2}$	Beam half-width
W_0	Minimum beam half-width
X_i	Number density fraction of species i
Z	Atomic number
α_e	Rotational constant correction factor
β_e	Centrifugal force correction factor
γ	Ratio of specific heats
ν	Wavenumber
Ω	Mean number of collisions
θ	$h\nu_0/k$ or angle subtended by beam electrons

LIST OF SYMBOLS - (Continued)

Subscripts

τ	Rate of excitation
τ'	Rate of de-excitation
$\omega_e, \omega_e x_e, \omega_e y_e$	Vibrational term value constants
τ	Vibrational relaxation time
e	Primary electrons
g	Total gas
N_2	Molecular nitrogen
P	P-branch
R	R-branch or rotational mode
V	Vibrational mode
0	Reservoir condition
1	Free stream conditions
2	Conditions behind normal shock

Superscripts

$'$	For the $N_2^+ B'^+ \gamma^+$ state
$''$	For the $N_2^+ X'^+ \gamma^+$ state

I. INTRODUCTION

The electron beam technique is a well-established method for determining species concentrations and the rotational and vibrational temperatures of molecular nitrogen in low density flow fields. In this method, an electron beam generator produces a narrow column of electrons which is projected across the flow field of interest. The interaction of the accelerated electrons with gas particles produces a column of radiation which is nearly coincident with the beam of electrons. Under appropriate conditions, the fluorescence can be analyzed spectroscopically to determine the concentration and temperatures of the active species.

The predominant radiation due to excitation of air is the first negative system of the ionized nitrogen molecule. The most intense band of this system is the (0,0) band at 3914 Å. Much experimental work (summarized in Ref. 1) has been done with the first negative system in nitrogen and air to verify the applicability of the diagnostic technique at sufficiently low density and high temperatures. Details of the methods can be found in Refs. 1-4.

In addition to radiation in the N_2^+ first negative system, excitation of air flows also leads to observation of radiation in the nitric oxide γ system. The γ system may be useful for vibrational temperature and number density measurements at wavelengths below approximately 3044 Å. At higher wavelengths, the γ bands are overlapped by bands from N_2 and N_2^+ systems. Additional radiation in the Feast and Ogawa systems also appear at wavelengths between 5800 and 6100 Å; however, these systems are unsuitable for electron beam diagnostics because of their low radiation intensities and the paucity of information on the excitation-emission processes which lead to the radiation. (Details of the excitation-emission analysis for the NO γ system are given in Ref. 5 and typical application of the techniques for NO are given in Ref. 6.)

Electron beam excitation of air flows also yields radiation in the O_2^+ first and second negative systems. The first negative system occurs at wavelengths near 6000 Å and is not suitable for electron beam measurements because of the severe overlap of vibrational bands within the system. The O_2^+ second negative system occurs at wavelengths between 2060 and 3230 Å and is suitable for measurement of O_2 vibrational temperatures. (The basic character of the radiation in both the O_2^+ first and second negative systems is discussed in Ref. 7 and applications of the measuring techniques are given in Ref. 8.)

To apply the electron beam technique for measurement of rotational temperatures, vibrational temperatures, and number densities, a detailed analysis of the excitation-emission process which leads to the observed spectra must be available. It is common to assume that the emission is excited by collisions between beam electrons and gas molecules in their

ground electronic energy state. All other excitation processes (excitation by secondary electrons and low energy ions, double excitation, cascading, etc.) and all selective quenching mechanisms are ignored. In addition, the excitation is assumed to occur so rapidly that no perturbations in the rotational and vibrational population distributions in the ground electronic state occur during the excitation process; hence, the Franck-Condon principle is applied. Rotational transition probabilities are obtained by assuming that only those transitions occur which are allowed by optical selection rules.

At temperatures above approximately 10³ K and densities below those corresponding to a pressure of 1 torr at room temperature, the assumption of direct excitation and application of optical selection rules lead to high accuracy in density and temperature measurements. However, as the gas density is increased, both collision quenching and excitation by secondary particles generated by the primary excitation process occur with increasing importance. Both of these mechanisms invalidate number density measurements, since the radiation intensity is no longer a predictable function of gas density, rotational temperature, and vibrational temperature.

There is much interest in extending the density range over which the electron beam can be applied, particularly for temperature measurements. The technique is attractive for a variety of flow fields because the measurements yield temperatures and, in some cases, actual population distributions without causing measurable perturbations in the flow field.

Ashkenas⁹ reported the results of nitrogen rotational temperature measurements made in a static test chamber and in an un-heated free jet with equivalent pressures up to 6.34 torr. (Equivalent pressure is defined as the static pressure obtained from the actual gas density and a static temperature of 300 K.) Ashkenas found that the error in measured rotational temperature increased logarithmically with density. Similar results were reported by Hunter.¹⁰ Maguire¹¹ reported rotational temperature results obtained from a free jet with static temperature from 80 to 300 K and equivalent pressures up to 10 torr. These free jet data show that excitation by low energy secondary particles is not a likely cause for errors observed in rotational temperature measurements. Selective quenching of the rotational energy levels was believed to be the cause for differences between measured and predicted temperatures. If such selective quenching exists, certain rotational energy levels will be quenched more effectively than others, so that the excitation-emission analysis used to interpret the measured intensities in terms of rotational and vibrational temperatures cannot be applied.

While there have been many studies of the range of applicability of the method for nitrogen rotational temperature measurements (see Muntz¹), little attention has been focused on similar studies for the measurement of vibrational temperatures. The techniques have been widely applied in flows with high vibrational temperatures,^{4,5,8,12-16}

but the gas densities have been in the range where the techniques are known to apply with acceptable accuracy. Harbour¹⁷ examined vibrational band intensity ratios in low temperature N_2 for equivalent pressures up to 3 torr and found large variations in the ratio of the $N_2^+(0,1)$ and $(1,2)$ vibrational bands. However, there have been no experiments aimed at evaluating the accuracy with which vibrational temperature measurements can be made at high densities.

The present studies were motivated by a requirement to examine the accuracy with which vibrational temperatures can be measured with an electron beam in high density flow fields generated by facilities with high reservoir temperatures. Calibration experiments were conducted in a static test chamber and in an arc-heated wind tunnel facility. The equivalent pressures ranged from 0.12 torr to 50 torr with static temperatures from 300 K to 1000 K, and vibrational temperatures from 300 K to 3000 K. These studies were conducted to assess the relative importance of excitation by low energy particles and excessive collision quenching on the accuracy with which temperature measurements can be conducted in molecular nitrogen, nitric oxide, and molecular oxygen.

II. THEORETICAL ANALYSES

A. MOLECULAR NITROGEN

The first negative system in molecular nitrogen is due to radiative transitions from an electronically excited state of $N_2^+(N_2^+B^2\Sigma)$ to the ion ground state ($N_2^+X^2\Sigma$). The excitation results from collisions of the beam electrons with nitrogen molecules in their ground electronic state ($N_2X^1\Sigma$). With the assumption of direct excitation and the use of optical selection rules, the excitation-emission analysis predicts bands composed only of a single R-branch and a single P-branch.¹ The P-branch lines are very close together and form the band head, while the R-branch lines are farther apart with wavelength separations which increase with decreasing wavelength. The intensity of a particular line can be written as⁴

$$I = \frac{CS_{K'} v^4 q(v', v'')}{2K' + 1} \frac{N_{N_2}}{Q_V(T_V)} \sum_{v_0} \frac{q(v_0, v')}{Q_R(v_0, T_R)} \times \exp \left[-\frac{G(v_0)hc}{kT_V} \right] H(v_0, K', T_R) / \sum_{v''} q(v', v'') \frac{Kv_R^3 + (K+1)v_P^3}{2K+1} \quad (1)$$

where $S_{K'} = K'$ for R-branch lines and $S_{K'} = K' + 1$ for P-branch lines. The vibrational quantum numbers in the $N_2X^1\Sigma$, $N_2^+B^2\Sigma$, and $N_2^+X^2\Sigma$ states are denoted by v_0 , v' , and v'' , respectively. The rotational quantum number in the $N_2^+B^2\Sigma$ state is denoted by K' . The quantities of the form $q(v_1, v_{11})$ are the Franck-Condon factors for the $v_1 \rightarrow v_{11}$

vibrational transitions, Q_V and Q_R are the vibrational and rotational partition functions, and ν is the wave number of the line. The factor $H(\nu_0, K', T_R)$ is given by¹

$$(K' + 1) \exp \left[- \frac{B_{V_0}(K' + 1)(K' + 2)hc}{kT_R} \right] + K' \exp \left[- \frac{B_{V_0}K'(K' - 1)hc}{kT_R} \right] \quad (2)$$

The rotator constant, B_{V_0} , is

$$B_{V_0} = 2.010 - .0187(\nu_0 + 1/2) \quad (3)$$

An accurate approximation to Eq. 1 is obtained by neglecting the dependency of the rotator constant and the rotational partition function on the degree of vibrational excitation. In this case, Eq. 1 is written as¹

$$\ln \left[\frac{I}{S_{K'}(G)\nu^4} \right] = - \frac{K'(K' + 1)\theta}{T_R} \quad (4)$$

where $\theta = Bhc/k$ and (G) is a known function of T_R and K' . The rotational temperature is determined by measuring the relative intensities of the rotational lines and plotting $\ln [I/S_{K'}(G)\nu^4]$ versus $K'(K' + 1)$. The result of this plot is a straight line with a slope equal to $-\theta/T_R$.

Rotational and vibrational temperatures are determined with a spectroscopic instrument yielding line and band intensities in the spectral region of interest. The rotational temperatures are usually obtained from the rotational lines in the $N_2^+(0,0)$ band, while vibrational temperatures are determined from scans of at least two bands [typically $N_2^+(0,1)$ and $N_2^+(1,2)$]. For vibrational temperature measurement, integration of the band intensities should be used to obtain accurate total band intensities.

At high rotational temperatures, the rotational lines corresponding to high rotational quantum numbers overlap the low rotational quantum number lines of the next band in the sequence. For example, rotational lines in the $(0,1)$ band with rotational quantum numbers greater than 24 overlap the P-branch of the $(1,2)$ band. This overlap of rotational lines must be included in the theoretical analysis to allow unambiguous interpretation of the measured band intensities in terms of vibrational temperature.

The band overlap can be obtained by computing the detailed intensity distribution with wavelength and will depend upon the resolution of the spectrometer used. This requires reasonable knowledge of the instrument function. When the spectrometer has slit widths large enough that the measured line width is much greater than the line width resulting from broadening processes, the instrument function can be obtained by assuming that the intensity distribution within a line is flat-topped as the line leaves the grating of the spectrometer. As the line is moved past

the exit slit (by rotating the grating), the intensity passing through the exit slit increases linearly with wavelength until the image of the entrance slit exactly coincides with the exit slit. For equal entrance and exit slit widths, further grating rotation leads to a linear decrease in intensity with wavelength. As shown in Fig. 1, the ideal instrument function for equal entrance and exit slit widths is an isosceles triangle. The ideal line profile is degraded by the actual intensity distribution within the image of the entrance slit, astigmatism, coma, and improper focusing. The effective dispersion is obtained with the ideal instrument function and measurements of line widths.

Theoretical estimates of band profiles within the electron beam-induced radiation can be obtained with the line intensity formulas and the effective instrument function of the spectrometer. A given spectral region is divided into an arbitrary number of points (typically 500) at which intensities are calculated. At each of these points, the lines which contribute to the measured intensity are determined from the wavelength of the lines and the line width. The line intensities calculated from Eq. (1) are multiplied by the instrument function (Fig. 1) and summed to give the intensity at the specific point. The resulting intensity distribution is integrated to give the total band intensities. The calculations are easily performed with a digital computer.

Typical comparisons of measured and predicted vibrational band profiles for the (0,1) and (1,2) bands of the N_2^+ first negative system at vibrational and rotational temperatures of 300 K are given in Fig. 2. Comparisons of the measured and predicted integrated band intensities are given in Fig. 3. The only significant difference between the experimental and theoretical band profiles occurs at the band head. In this region, the electro-optical system used to obtain the experimental band profiles did not respond sufficiently to give a true measure of the intensity distribution within this high wavelength portion of the (0,1) band head. Except for this effect, the theoretical model gives an excellent representation of the measured band profiles for the N_2^+ first negative system.

The band intensity ratios for the (0,1) and (1,2) bands, including the effects of overlap due to high rotational temperatures, are given in Fig. 4. It is to be noted that significant errors in indicated vibrational temperature occur when the overlap accompanying high rotational temperatures is ignored. All of the vibrational temperature data reported here were obtained from Fig. 4 employing the measured rotational temperatures and the integrated (0,1) and (1,2) vibrational band intensities.

B. NITRIC OXIDE

The nitric oxide γ bands result from a ${}^2\Sigma^+ - {}^2\pi$ electronic transition and the rotational structure is quite complicated. In the ${}^2\Sigma^+$ state, the electronic orbital angular momentum is zero and the

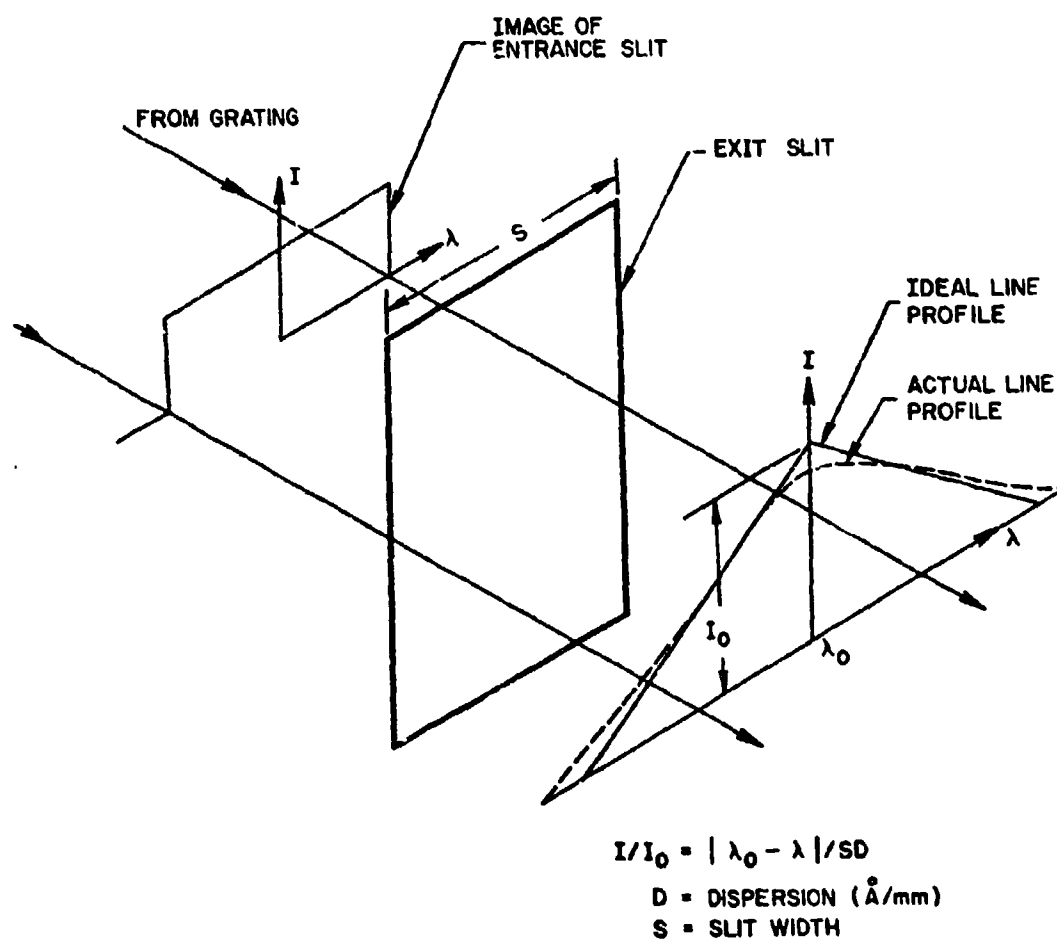


Figure 1. Spectrometer instrument function

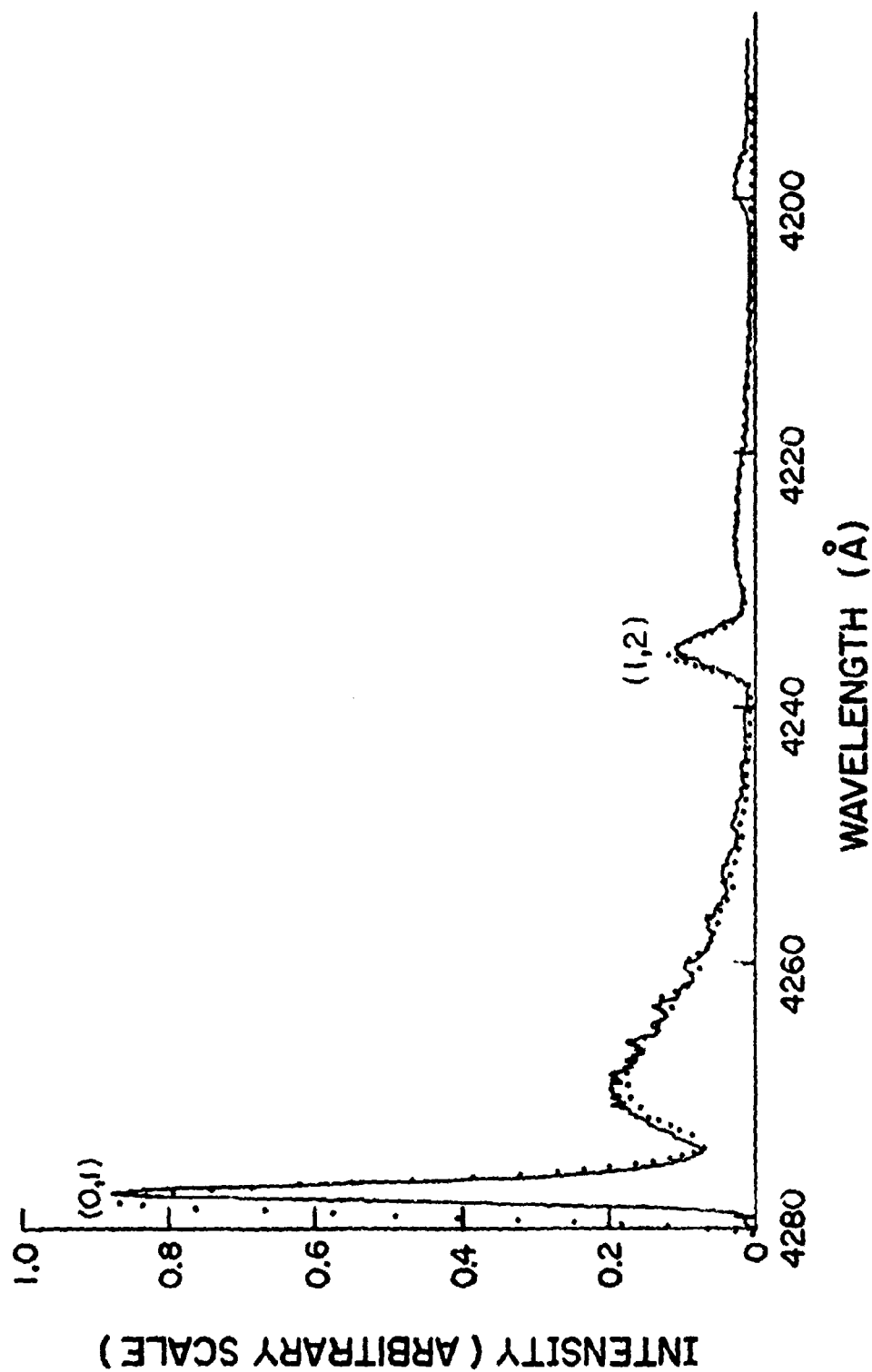


Figure 2. Theoretical and experimental band profiles for the N_2^+ first negative (0,1) and (1,2)_o bands;
 theoretical, dispersion = 14.7 Å/mm;
 — experimental, $P_{EQ} = 0.2$ torr, slit width = 150 μ m, $T_R = T_V = 300$ K.

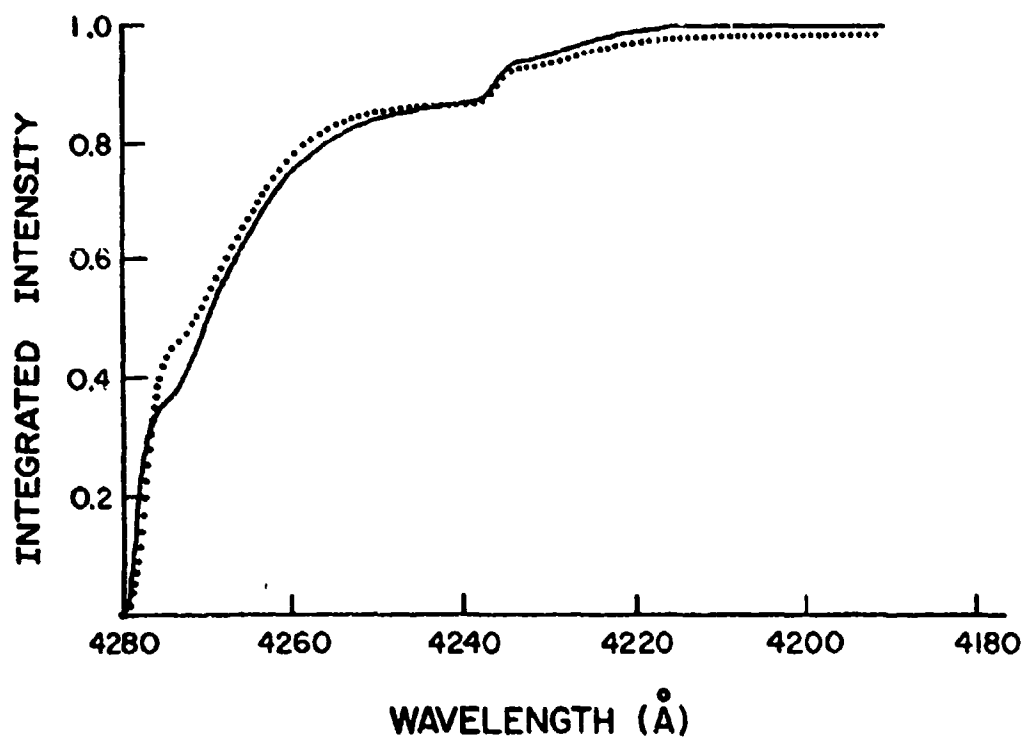


Figure 3. Theoretical and experimental integrated band profiles for the N_2^+ first negative (0,1) and (1,2) bands;
 theoretical, dispersion = 14.7 Å/mm;
 — experimental, $P_{EQ} = 0.2$ torr, slit
 width = 150 μ m, $T_R = T_V = 300$ K.

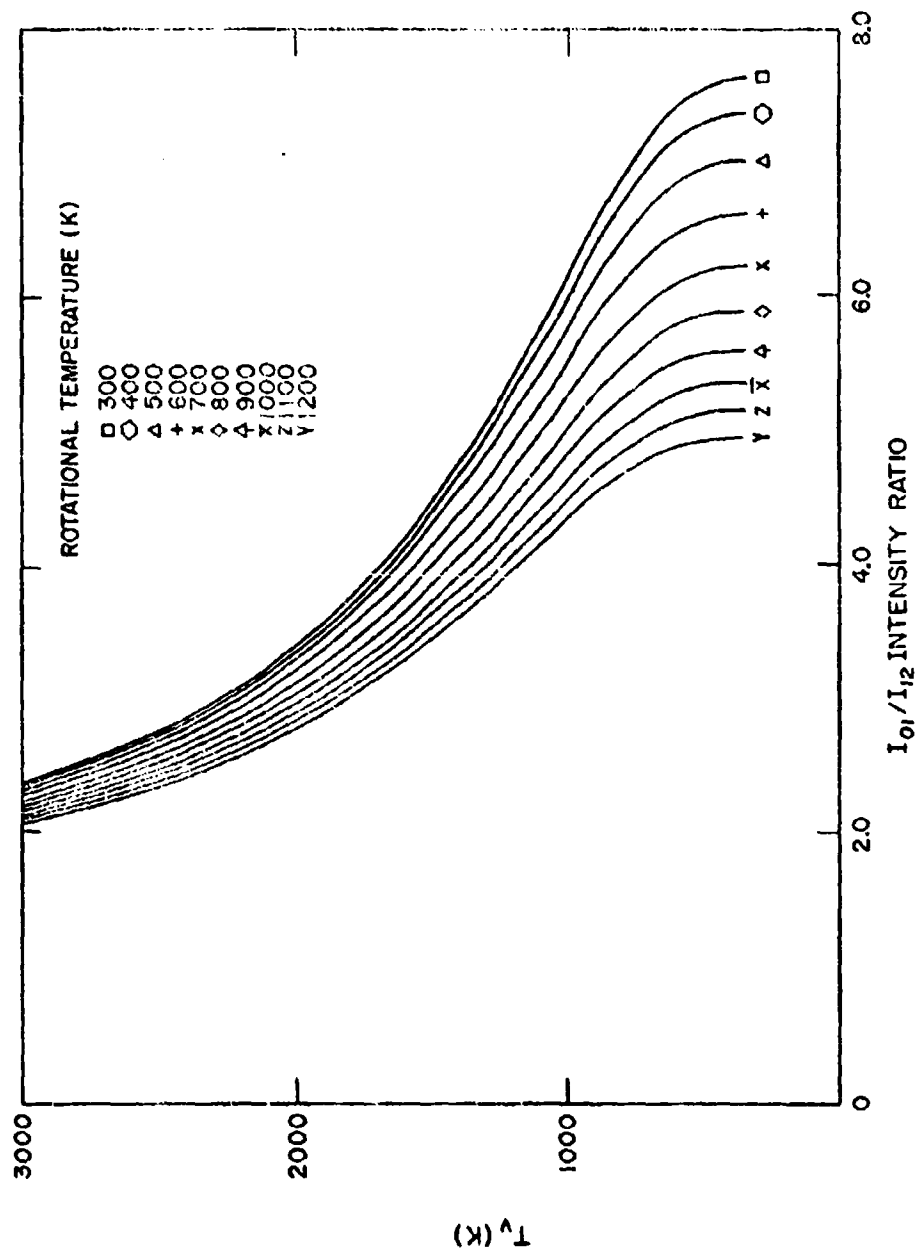


Figure 4. Integrated vibrational band intensity ratios for the N_2^+ first negative (0,1) and (1,2) bands

coupling between the various angular momenta can be assumed to follow Hund's case (b).¹⁸ The rotational energy levels in the ${}^2\Pi^+$ state consist of two components corresponding to $J = K \pm 1/2$, where \vec{K} denotes the angular momentum vector, apart from spin, and \vec{J} is the total angular momentum vector.

In the ${}^2\Pi$ ground state, the electronic orbital angular momentum is non-zero and the molecular coupling usually can be assumed to follow either Hund's case (a) or (b). In case (a), the rotational energy levels consist of two components denoted by ${}^2\Pi_{1/2}$ and ${}^2\Pi_{3/2}$, where the subscript gives the values of the quantum number associated with the sum of the components of electronic orbital angular momentum and spin in the direction of the internuclear axis. In case (b), the coupling is the same as for ${}^2\Sigma^+$ states and the multiple levels correspond to J values of $K \pm 1/2$. It is often found that the molecular coupling follows case (a) at lower rotational quantum numbers and approaches case (b) at higher quantum numbers. While such is the case for the NO γ bands, such a transition in coupling makes calculation of wavelengths difficult at intermediate quantum numbers. Churchill¹⁹ gives term values which apply throughout the NO γ bands, circumventing the need to choose between case (a) and case (b) in the calculation of line positions.

The selection rules for transitions between the two states in the NO γ system are $\Delta J = 0, \pm 1$. Hence, R, P, and Q branches exist for transitions from each multiplet level in the ${}^2\Sigma^+$ state to the ${}^2\Pi$ state. In addition, satellite lines appear corresponding to transitions for which ΔK is not equal to ΔJ .

The intensity of a rotational line in the NO γ system resulting from direct excitation of nitric oxide with an electron beam is given in Ref. 5 as

$$I = \frac{h\nu^4 p(v', v'') P(J', J'') \phi(v', J')}{\sum_{v''} \left[p(v', v'') \sum_{J''} P(J', J'') v^3 \right]} \quad (5)$$

where

$$\phi(v', J') = c \sum_{v''} p(v', v'') \left[\sum_{J''} N(v'', J'') P(J', J'') \right] \quad (6)$$

where $P(J', J'')$ is the properly normalized Hönl-London factor and $p(v', v'')$ is the vibrational transition probability, which is assumed equal to a constant times the Franck-Condon factor. The Hönl-London factors and Franck-Condon factors are summarized in Ref. 5. The term values used to calculate the line positions are given in Table I.

Table I. Molecular Constants for NO γ System

	$^2\Pi_{1/2}$	$^2\Pi_{3/2}$	$^2\Sigma^+$
T_e	0.0		43965.7
ω_e	1904.03	1903.68	2371.1
$\omega_e x_e$	13.97		14.48
$\omega_e y_e$	-0.00120		-0.28
B_e	1.7046		1.9930
α_e	0.0178		0.0198
D_e	5×10^{-6}		6.0×10^{-6}
β_e	---		0.3×10^{-6}

Vibrational Term Values:

$$G(v) = \omega_e(v + \frac{1}{2}) - \omega_e x_e(v + \frac{1}{2})^2 + \omega_e y_e(v + \frac{1}{2})^3$$

Rotational Term Values:

$$^2\Pi_{1/2} \quad , \quad ^2\Pi_{3/2}$$

$$F(J) = B_v \left\{ \frac{(J+1)^2}{J^2} - 1.0 + 0.5 \left[\frac{4(J+1)^2}{4J^2} + \frac{124.2}{B_v} \left(\frac{124.2}{B_v} - 4 \right) \right]^{1/2} \right\} \begin{matrix} \text{for } ^2\Pi_{3/2} \\ \text{for } ^2\Pi_{1/2} \end{matrix}$$

$$^2\Sigma^+$$

$$F(K) = B_v K(K+1) - D_v K^2(K+1)^2$$

$$D_v = D_e + \beta_e(v + \frac{1}{2})$$

The numerical methods discussed in the previous section were used to model the intensity distribution within the bands of the NO γ system. Detailed comparisons of the calculated wavelengths of the lines were made with the data given in Ref. 20. The present theory yields line positions with errors no greater than a few wave numbers. A typical comparison of predicted and measured vibrational band profiles for the (0,4) and (1,5) bands is given in Fig. 5. It can be seen that the theoretical model slightly underestimates the relative intensities of the rotational lines in the tail of the bands and that the predicted relative magnitude of the bands within a sequence (Δv = constant) are incorrect. At room temperature, the theory predicts that the (1, v'') bands will have the greatest intensity within all sequences. This results from a shift in the potential curves (energy vs. inter-nuclear separation) between the NO ground state and the Σ^+ upper state of the γ system. This shift causes the Franck-Condon factor for the $v'' = 0 \rightarrow v' = 1$ transition to be the largest for $v'' = 0$. At room temperature, populations of vibrational levels for $v'' > 0$ are negligible so that the excitation transitions primarily populate the $v' = 1$ level in the Σ^+ state. Hence, the theory predicts that the (1, v'') band will dominate each sequence. However, the experimental measurements clearly show that (0, v'') bands dominate at room temperature.

There are many possible causes for the discrepancies between the theoretical and experimental band intensities. Mechanisms such as cascading, selective quenching, self-absorption, excitation by secondary electrons, and upper-state relaxation are possible causes. Neither cascading, selective quenching, self-absorption nor excitation by secondary electrons are likely mechanisms causing inapplicability of the direct excitation-emission model. Cascading is possible because of the $E^{2,2+} \rightarrow A^{2,2+}$ transition of the Feast 1 system, which populates the $A^{2,2+}$ level. However, the spectral studies of Ref. 5 show that the radiation in the Feast system is extremely weak, indicating that relatively few molecules are excited to the $E^{2,2+}$ state.

Selective quenching of the vibrational energy levels within the Σ^+ state is also not a likely cause for the discrepancies between the theoretical and experimental relative band intensities. As shown in Ref. 5, the NO γ system has a relatively high self-quenching pressure of 2.35 torr and ratios of band intensities are constant over a range in pressure at least from 0.2 to 3.0 torr. In addition, the discrepancies are observed at low pressures where quenching can be ignored.

As discussed in Ref. 5, the NO γ system is a resonant transition so that radiation emitted in the region of the electron beam may be absorbed by NO molecules in the surrounding gas. This re-absorption can lead to induced radiative transitions and volume fluorescence throughout the gas. However, the total light intensity due to the volume fluorescence and induced emission can be only as large as the absorbed light intensity. Further, the fluorescence and induced emission are radiated spherically, so that only a small percentage of their total radiation can enter the optical system. Hence, fluorescence and induced emission can be ignored.

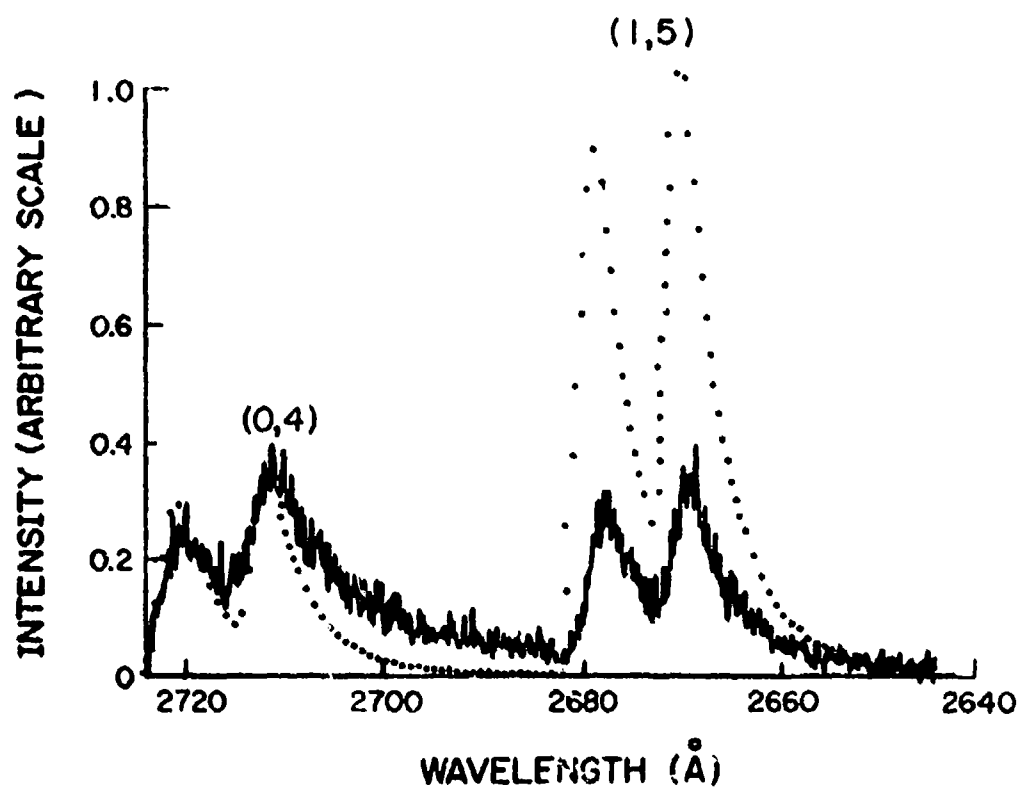


Figure 5. Theoretical and experimental band profiles for the NO γ (0,4) and (1,5) bands;
 theoretical, direct excitation, dispersion = 14.7 Å/mm
 ——— experimental, $P_{FQ} = 0.3$ torr, slit width = 150 μ m, $T_R = T_V = 300$ K.

Detailed calculations of the absorption to be expected in the NO γ system are given in Ref. 5 where it is shown that absorption can be neglected for NO number density-path lengths products less than 10^{17} cm $^{-2}$ when the emission transition is to vibrational energy levels other than the ground state ($v'' = 0$). In the present studies, the number density-path length product was always less than 10^{17} cm $^{-2}$, so that the effects of absorption can be neglected.

Excitation by low energy secondary electrons also is not likely. When the excitation is dominated by secondary electrons, the intensity of the radiation varies quadratically with density at densities low enough to avoid significant quenching.⁵ However, the results of Ref. 5 show that the variations of the band intensities with density are linear at equivalent pressure below 0.20 torr. Hence, excitation by low energy secondary electrons cannot be a predominant mechanism.

The apparent inapplicability of the direct excitation model for the NO γ system is most likely related to the polar nature of the molecule. Since vibration-rotation transitions can occur optically within an electronic energy state, redistribution of the energy can occur both in the $X^2\pi$ state in the early stages of excitation by the high speed electrons and in the $A^2\Sigma^+$ state before the electronic de-excitation transition has a chance to take place. Since the Born-Oppenheimer approximation is expected to be valid for excitation by beam electrons, redistribution of the energy within the $X^2\pi$ state prior to the $^2\pi - ^2\Sigma^+$ electronic transition is not likely. However, redistribution of the energy in the $^2\Sigma^+$ state due to vibration-rotation transitions appears quite likely and may influence the relative band intensities. In this case, the vibration-rotation transitions must occur within the lifetime of the $^2\Sigma^+$ state.

The influence of vibration-rotation transitions within the $^2\Sigma^+$ state prior to the $^2\Sigma^+ \rightarrow ^2\pi$ electronic transition can be estimated by including upper-state vibration-rotation transitions in the excitation-emission model. This is accomplished by assuming that the NO molecule in the $^2\Sigma^+$ state can be represented as a harmonic oscillator. In this case, vibrational transitions can occur only between adjacent vibrational energy levels and the transition probabilities are proportional to the vibrational quantum number of the initial state in the transition.²¹ Hence, the vibrational transition probabilities can be written as

$$p'(v', v' \pm 1) = k_{10} v' \quad (7)$$

where k_{10} is the probability for the $1 \rightarrow 0$ vibrational transition. The allowed rotational transitions are those for which $\Delta K = \pm 1$ and the corresponding transition probabilities are given by the usual Hönl-London factors.

The transitions in the upper-state are included in the excitation-emission model by assuming that only de-excitation transitions occur in the $^2\Sigma^+$ state. Hence, all collisional effects and absorption within

the $^2\Sigma^+$ state are ignored. With these assumptions, the rate of population of a particular (v', K') level in the $^2\Sigma^+$ state can be given by

$$\begin{aligned} \phi(v', K') = & C_\phi \sum_{v''} \left[\sum_{J''} N(v'', J'') P(J', J'') \right] p(v', v'') \\ & + C_K (v' + 1) k_{10} [N(v' + 1, K' + 1) P_R \nu_R^3 + N(v' + 1, K' - 1) P_P \nu_P^3] \end{aligned} \quad (8)$$

where P_R and P_P are the Hönl-London factors for the R-branch and P-branch rotational transitions and C_ϕ and C_K are constants independent of the quantum numbers. The first term on the right hand side of Eq. (8) accounts for the usual direct excitation from the $X^2\pi$ state while the second term accounts for vibrational de-excitation transitions within the $^2\Sigma^+$ state. Note that only P and R branches exist within the $^2\Sigma^+$ state and that the splitting accompanying the doublet structure is ignored. The rotational and vibrational quantum numbers in the $X^2\pi$ state are denoted by J'' and v'' , respectively, and the sum over J'' includes all branches in the composite model discussed above.

The total rate of depopulation of the (v', K') level is assumed to result only from optical transitions and can be written as

$$\begin{aligned} \psi(v', K') = & N(v', K') \left[C_a \sum_{v''} \sum_{J''} p(v', v'') P(J', J'') \nu_{v', v'', J', J''}^3 \right. \\ & \left. + C_K v' k_{10} (P_R \nu_R^3 + P_P \nu_P^3) \right] \end{aligned} \quad (9)$$

In the steady state, the total rate of excitation must be equal to the rate of de-excitation so that $\phi(v', K') = \psi(v', K')$. Hence, from Eqs. (8) and (9), the population of the $N(v', K')$ states are given by

$$\begin{aligned} N(v', K') = & \left\{ C_\phi \sum_{v''} \left[\sum_{J''} N(v'', J'') P(J', J'') \right] p(v', v'') \right. \\ & \left. + C_K (v' + 1) k_{10} [N(v' + 1, K' + 1) P_R \nu_R^3 + N(v' + 1, K' - 1) P_P \nu_P^3] \right\} / \\ & \left\{ C_a \sum_{v''} \sum_{J''} p(v', v'') P(J', J'') \nu_{v', v'', J', J''}^3 + C_K v' k_{10} [P_R \nu_R^3 + P_P \nu_P^3] \right\} \end{aligned} \quad (10)$$

Examination of Eq. (10) shows that it represents a hierarchy of equations for the populations of all the vibrational levels in the $^2\Sigma^+$ state. To obtain a solution, a maximum value for the vibrational quantum number in the $^2\Sigma^+$ must be chosen. Deezi²⁰ shows that the NO molecule dissociates into N(⁴S) and O(³P) at an energy slightly higher than that for the $v' = 3$ level. In addition, no vibrational bands for $v' > 3$ have been reported for the ν system.^{5, 20, 22} Hence, it is reasonable to terminate the vibrational quantum number at 3 in Eq. (10). For $v' = 3$ there is no population due to transitions from higher vibrational levels so that Eq. (10) can be written as

$$\frac{C_a}{C_p} N(3, K') = \frac{\sum_{v''} \sum_{J''} N(v'', J'') P(J', J'') p(v', v'')}{\sum_{v''} \sum_{J''} p(v', v'') P(J', J'') v^3 + 3(C_k/C_a) k_{10} [P_R v_R^3 + P_P v_P^3]} \quad (11)$$

Assuming a Boltzmann distribution for the $X^2\Pi$ state allows relative values for $N(v'', J'')$ to be obtained so that Eq. (11) can be solved for the relative value of $N(3, K')$. With this value, the population of the remaining vibrational energy levels can be solved sequentially for decreasing values of v' . Once the populations are obtained, the relative intensities of the rotational lines in the γ system can be obtained from

$$I = av^4 p(v', v'') P(J', J'') N(v', K') \quad (12)$$

where a is a constant of proportionality.

Explicit solution of Eq. (11) requires that the relative value of the vibrational transition probability $(C_k/C_a)k_{10}$ be available. The term C_k relates k_{10} to the absolute vibrational transitional probability, which can be obtained with good accuracy for the assumed harmonic oscillator model. However, C_a includes, in part, the electronic transition moment; its evaluation requires knowledge of the absolute electronic transition probabilities for the bands in the γ system.

Since little precision in the absolute electronic transition probabilities is available, an effective value for $(C_k/C_a)k_{10}$ was determined by comparing theoretical and experimental band profiles at room temperature. The value of $(C_k/C_a)k_{10}$ was adjusted until the integrated relative intensities of the (0,4) and (1,5) bands obtained from the theory agreed with those measured at pressures below 0.3 torr at room temperature. The appropriate value for $(C_k/C_a)k_{10}$ with the non-dimensionalizing scheme used in Eqs. (8-10) is 0.08.

Equations (10-12) were used to compute the variation of the ratio of the intensities of the (0,4) and (1,5) bands with rotational and vibrational temperatures. In addition, the band intensity ratio obtained with simple direct excitation ($k_{10} = 0$) was computed. The results are given in Fig. 6. It is noteworthy that for the spectrometer resolution used in these calculations there is no significant overlap of the (0,4) and (1,5) bands for rotational temperatures from 300 K to 1000 K. Hence, the band intensity ratios for the direct excitation model are independent of rotational temperature over this temperature range. However, when vibration-rotation transitions are allowed to occur in the $^2\Sigma^+$ state, the band intensity ratio depends upon both the rotational and vibrational temperatures. For rotational temperatures up to 1000 K, the theory results in negligible overlap of the high rotational quantum number lines of one band with the head of the next band in the sequence. Hence, the variation of band intensity ratio with rotational temperature implies that the transitions within the $^2\Sigma^+$ state alter both the rotational and vibrational population distributions prior to the emission transitions.

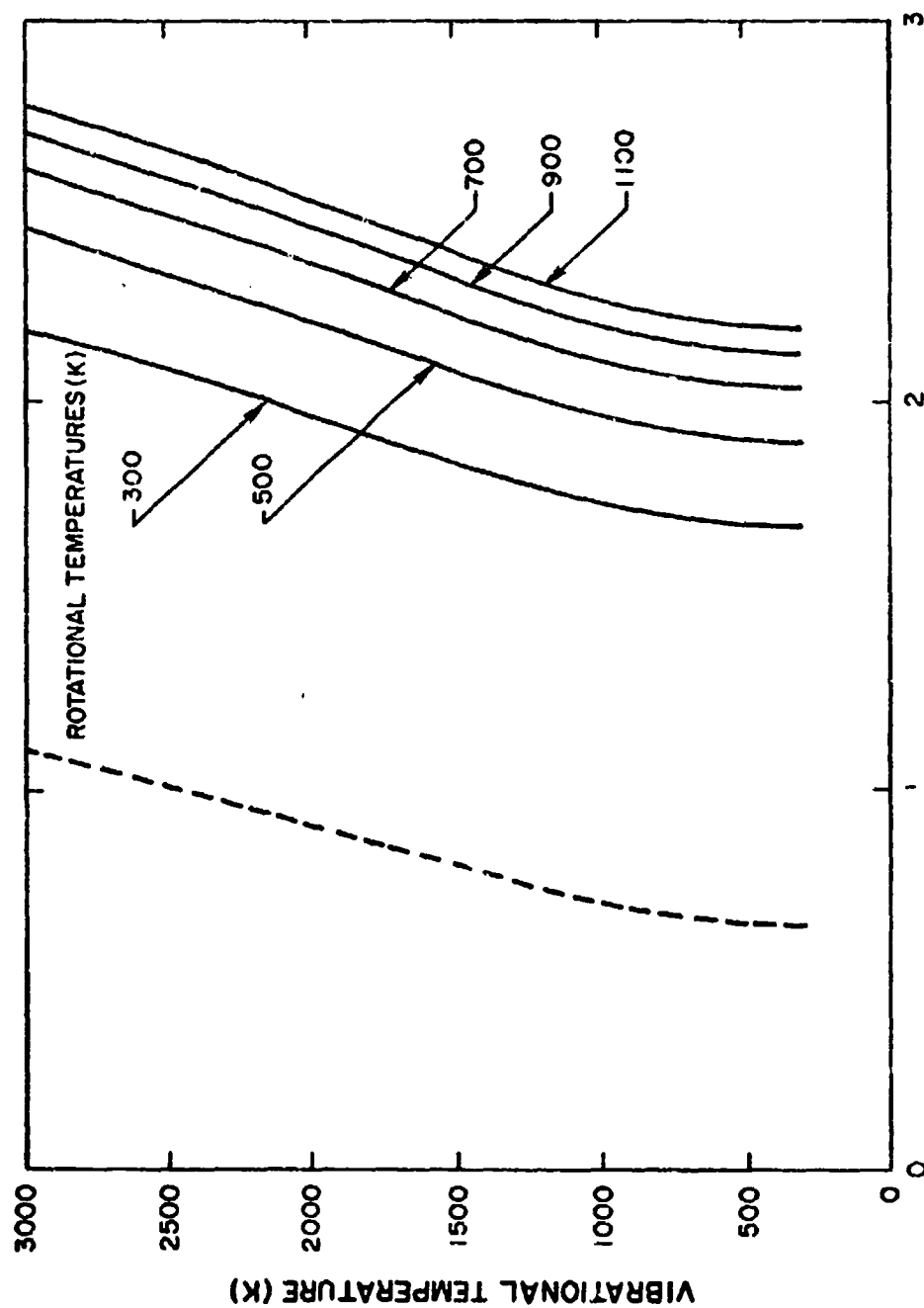


Figure 6. Vibrational band intensity ratios for the NO γ (0,4) and (1,5) bands; --- direct excitation; --- vibrational relaxation model

In practical applications of an electron beam to measuring vibrational temperature, the relative sensitivities of the optical system are obtained by measuring the relative band intensities at a known condition (usually room temperature). The resulting scale factor is used to convert the measured band intensities obtained in the unknown environment to vibrational temperature. In this manner, the technique always gives the correct temperature at the known condition. The effect is to non-dimensionalize the curves of Fig. 6 by their values at the known condition. The band intensity ratio curves of Fig. 6 non-dimensionalized by their respective values at rotational and vibrational temperatures of 300 K are given in Fig. 7. This displays the relative importance of vibrational relaxation in the $^2\Sigma^+$ state and it is seen that the non-dimensional variations of the band intensity ratios with vibrational temperature are altered only slightly by the vibrational relaxation. Hence, the main effect of the relaxation is to change the relative values of the band intensities and to introduce a rotational temperature dependence. There is little overall effect on the sensitivity of band intensity ratios to vibrational temperature when pre-run scaling of relative band intensities is employed.

Comparing Figs. 4 and 6, it can be seen that the band intensity ratios for the NO γ system are much less sensitive to vibrational temperature than are the ratios for the N_2^+ first negative system. Hence, extreme accuracy is required to obtain reasonable values for the nitric oxide vibrational temperature. An error in measured intensity ratio as small as 5% results in a vibrational temperature error near 20%.

The applicability of the excitation-emission model employing vibrational relaxation in the $^2\Sigma^+$ state can be determined only by detailed comparisons of theoretical and experimental results at elevated vibrational temperature. There is no guarantee that the model is correct since a one-point comparison was used to establish a single unknown relative transition probability. Certain comparisons of the results from this model with band profiles measured at moderate vibrational temperatures are given in the next section of this report.

C. QUENCHING MECHANISMS

The analyses of the preceding sections apply only when collision quenching can be ignored. A more general analysis can be formulated to include other excitation/de-excitation mechanisms. To allow specific equations to be formulated, the following analysis is presented for molecular nitrogen in an arbitrary gas mixture. However, the results are applicable in principle to any radiating species.

The important excitation processes are assumed to include only excitation by primary (beam) electrons and secondary electrons liberated by the bombardment of ground state particles by primary electrons. These processes are represented (for N_2) by:

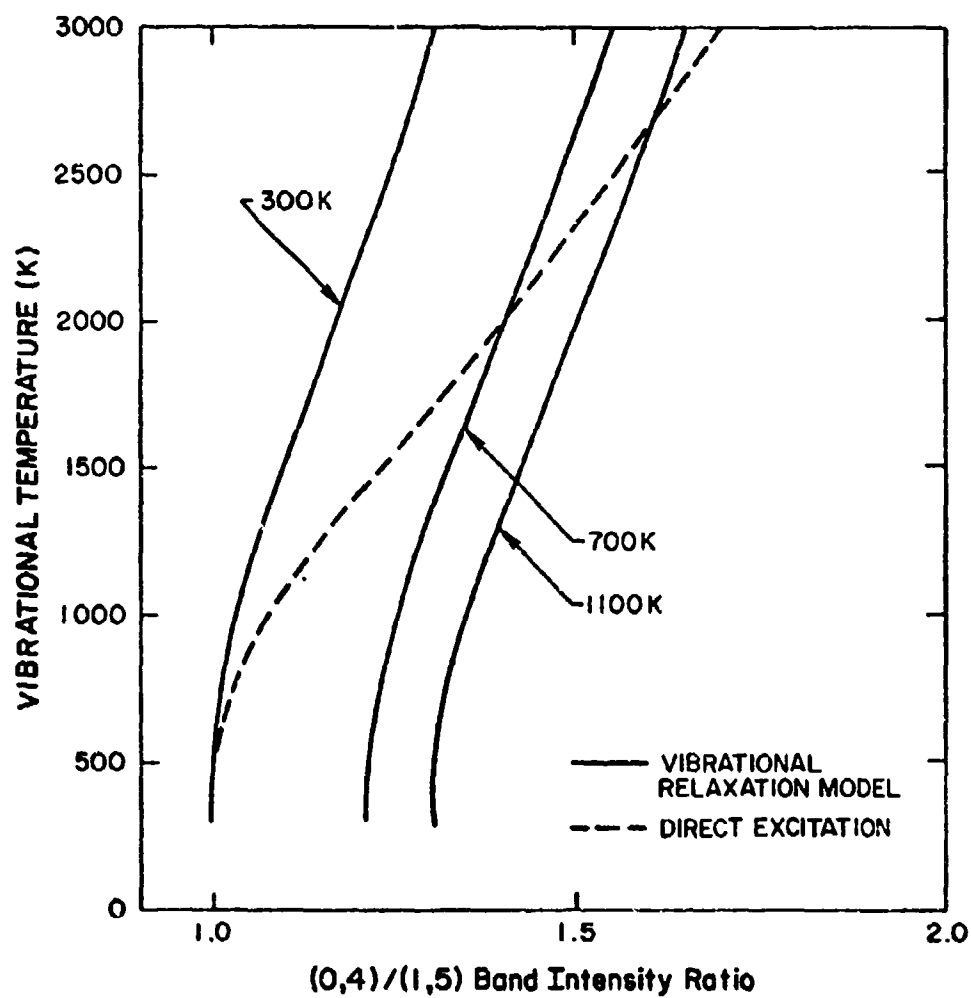


Figure 7. Nondimensional band intensity ratios for the NO γ (0,4) and (1,5) bands. Ratios nondimensionalized by their values at $T_R = T_V = 300$ K

$$N_2(X^1\Sigma) + e_p \xrightarrow{Q_0(v_e)} N_2^+(B^2\Sigma) + e_p + e_s \quad (13)$$

and

$$N_2(X^1\Sigma) + e_s \xrightarrow{Q_S(v_s)} N_2^+(B^2\Sigma) + 2e_s \quad (14)$$

where e_p and e_s denote, respectively, primary and secondary electrons and $Q_0(v_e)$ and $Q_S(v_s)$ are the cross-sections for excitation by primary electrons with velocity v_e and secondary electrons with velocity v_s , respectively.

Secondary electrons are ejected from the parent molecules in random directions and with a range of energy. Their distribution must be calculated by balancing the effects of diffusion, collisions, and space charge. An analysis sufficient to describe the local secondary electron concentration has been given previously⁷ and yields a rate of excitation given by

$$n_s v_s n_g Q_S(v_s) X_i = Q_S(v_s) X_i \left[\frac{n_s v_s n_g \sum_j X_j Q_{jT}(v_e)}{\sum_j X_j Q_{jS}(v_s) + \lambda_s^2 / n_g} \right] \quad (15)$$

where n_s and n_g are the secondary electron and total gas number densities and X_i is the number density fraction of N_2 molecules in the mixture. The total cross-section for excitation of species j by secondary electrons is given by $Q_{jS}(v_s)$, where X_j is the number density fraction of species j , and λ_s^2 is related to the diffusion coefficient. The term $Q_{jT}(v_e)$ is an effective ionization cross-section for production of secondary electrons in the energy range necessary to excite $N_2(X^1\Sigma)$ to the $N_2^+(B^2\Sigma)$ state.

De-excitation of the $N_2^+(B^2\Sigma)$ is assumed to result from radiative transitions and collision quenching. These are represented by

$$N_2^+(B^2\Sigma) \xrightarrow{A} N_2^+(X^2\Sigma) + h\nu \quad (16)$$

and

$$N_2^+(B^2\Sigma) + N_j \xrightarrow{Q_{jC}} N_2^+(X^2\Sigma) + N_j \quad (17)$$

where N_j denotes the concentration of species j , Q_{jC} is an effective quenching cross-section, and A is the sum of all the optical transition probabilities.

In the steady state, Eqs. (13-17) yield the population of the $N_2^+(B^2\Sigma)$ state as⁷

$$[N_2^+(B^2\Sigma)] = \frac{neve n g Q_0(v_e) X_{N_2}}{A \left[1 + n_g/A \sum_j X_j Q_{jc} \right]} + \frac{Q_s(v_s) X_{N_2} n_e n_g v_e \sum_j X_j Q_{jT}(v_e)}{A \left[1 + n_g/A \sum_j X_j Q_{jc} \right] \left[\sum_j X_j Q_{js}(v_s) + \lambda_s^2/n_g \right]} \quad (18)$$

For the present discussion, we ignore the detailed spectral structure of the radiation and write the radiation intensity as

$$I = h\nu^4 A [N_2^+(B^2\Sigma)] \quad (19)$$

combining Eqs. (18) and (19) gives

$$I = \frac{a n_g^J Q_0(v_e) X_{N_2}}{1 + \sum_j (n_j/n_j')} + \frac{a n_g^J Q_s(v_s) X_{N_2}}{1 + \sum_j (n_j/n_j')} \times \frac{\sum_j X_j Q_{jT}(v_e)}{n_g \sum_j X_j Q_{js}(v_s) + \lambda_s^2} \quad (20)$$

where J is the beam current and a is a constant depending, in part, on geometrical factors. The quantity n_j' is the quenching density of species j and in a single species gas gives the density at which the intensity is reduced to one-half the value obtained in the absence of collision quenching.

If excitation by secondary electrons can be ignored, the intensity expression degenerates to a Stern-Volmer²³ equation of the form

$$I = \frac{a_1 n_g X_{N_2}}{1 + \sum_j (n_j/n_j')} \quad (21)$$

At high densities, the terms in the summation of Eq. (21) dominate the denominator and the intensity can be written as

$$I = \frac{a_1 n_g X_{N_2}}{\sum_j (n_j/n_j')} \quad (22)$$

Note that if one term of the summation dominates, Eq. (22) becomes

$$I = a_1 n_j' X_{N_2} / X_j \quad (23)$$

while for a single species gas, the intensity is

$$I = a_1 n' \quad (24)$$

where n' is the self-quenching density. Under the conditions leading to either Eq. (23) or (24), the radiation intensity is independent of the absolute number density and becomes a function of temperature (through the unique dependence of n_j' on temperature) and the relative concentrations of N_2 and the quenching species.

It is clear that in the presence of severe collision quenching, measurements of the absolute N_2 number density cannot be made with an electron beam. It may be possible to determine relative concentrations, but only if the detailed dependencies of the quenching number densities (n_j') on temperature are known.

To evaluate the effect of selective quenching on temperature measurements, Eq. (21) is written as

$$I = \frac{I_0}{1 + \sum_j (n_j/n_j')} \quad (25)$$

where I_0 is the intensity which would be observed if there were no quenching and is given by Eq. (1). Rotational and vibrational temperatures are usually obtained from measurements of the relative intensities of rotational lines (or groups of lines). If the quenching is not selective, the denominator of Eq. (25) will have the same value for all lines and will not alter an intensity ratio. In other words, rotational and vibrational temperatures can be measured in the presence of quenching if the n_j' values do not depend upon the rotational and vibrational quantum numbers in the $N_2^+(B^2\Sigma)$ state. The experimental studies described in the following sections of this report were directed, in part, at examining the accuracy with which vibrational temperatures can be measured when the intensities resulting from electron beam excitation must be represented in the form of Eq. (25).

III. EXPERIMENTAL APPARATUS AND PROCEDURES

A. TEST FACILITIES

1. Static Chamber

A series of experiments was conducted in a static test chamber shown schematically in Fig. 8. The chamber consists of a cadmium plated steel cylinder 18 inches in diameter and 18 inches long. Vacuum conditions in the chamber are maintained by a mechanical vacuum pump. Pressures are measured with a thermocouple gage, Wallace and Tiernan absolute pressure gages, and variable reluctance pressure transducers. The electron beam is projected across the tank in a direction perpendicular to the tank axis. The drift tube of the electron beam generator

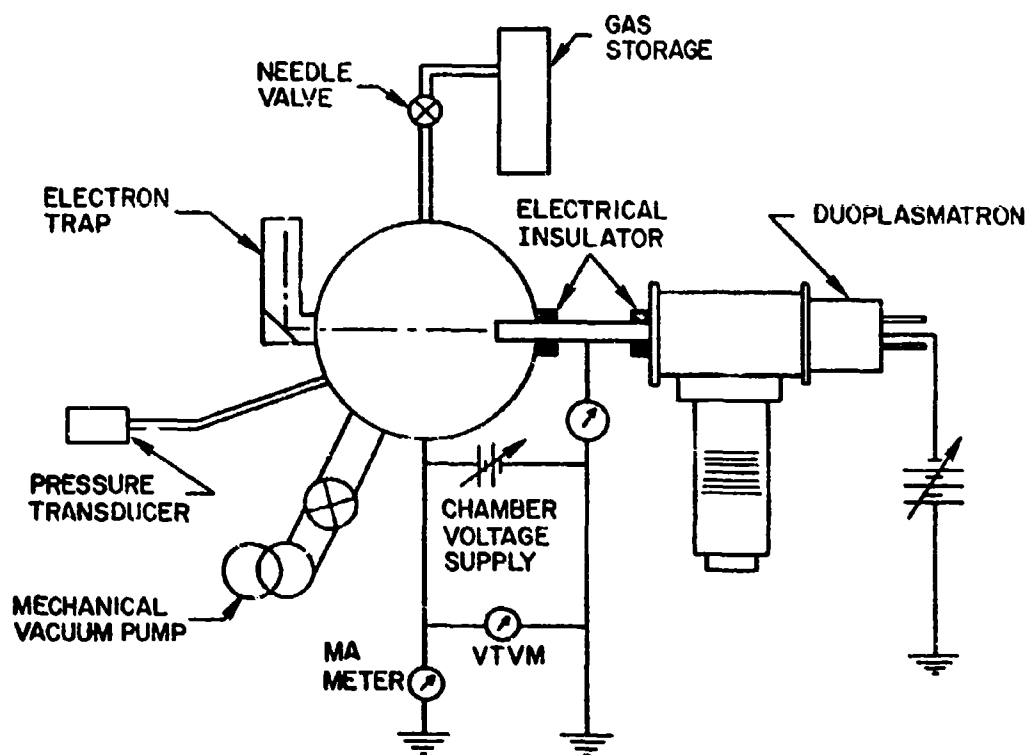


Figure 8. Static test chamber schematic

is electrically isolated from the chamber so that the entire chamber serves as the beam collecting device. A specially designed electron trap is used to reduce reflection of beam electrons back into the test chamber.

The electron beam generator employed for these tests utilized a duoplasmatron electron source and is described in detail in Ref. 5. The nominal beam voltage was 20 kV and the beam current was approximately 2 mA. Electron beam currents were measured with a standard milliammeter and were recorded by measuring the voltage drop across the meter resistor.

Experiments were conducted with nitrogen and air at static pressures up to 50 torr. Pressures were maintained by balancing the pumping rate of the vacuum system with gas injection controlled by a precision needle valve. For most experiments, the gas was injected at the top of the tank and the vacuum pump was connected near the bottom of the tank in an attempt to force direct flow across the region of observation.

At static pressures greater than approximately 10 torr, severe beam-plasma interactions were observed. These were manifested as large fluctuations in measured beam current. In most cases, negative beam currents were observed. The erroneous beam current signals resulted from potential differences between the insulated drift tube and the test chamber, so that the drift tube collected charged particles. This situation was alleviated by connecting a vacuum tube voltmeter and a dc power supply between the drift tube and the static chamber. The power supply potential was adjusted to maximize the beam current indication. However, the precise value of the beam current under these conditions was unknown.

2. Arc-Heated Wind Tunnel

An arc heated wind tunnel facility was employed to provide air flows at known thermodynamic conditions. The facility is shown schematically in Fig. 9 and consists of a direct current arc heater, a settling chamber, a conical convergent-divergent nozzle, a free jet test cabin, and a pressure recovery system. The settling chamber is employed to reduce spatial and temporal fluctuations in gas properties. In addition, several bare-tube heat exchangers consisting of water-cooled copper tubing were inserted in the flow to reduce the flow stagnation temperature. In certain cases, unheated air was admixed with arc heated air in the settling chamber upstream of the heat exchanger section. With this arrangement, the reservoir temperature could be varied from approximately 1400 K to 5500 K at a nominal reservoir pressure of 1.0 atmosphere.

Two conical nozzles were employed. The first nozzle (N1) had an expansion half angle of 3.5° and delivered a flow with a nominal Mach number of 2.0 and a static pressure of 60 torr. The vacuum pumping station maintained a pressure in the free jet test cabin of approximately

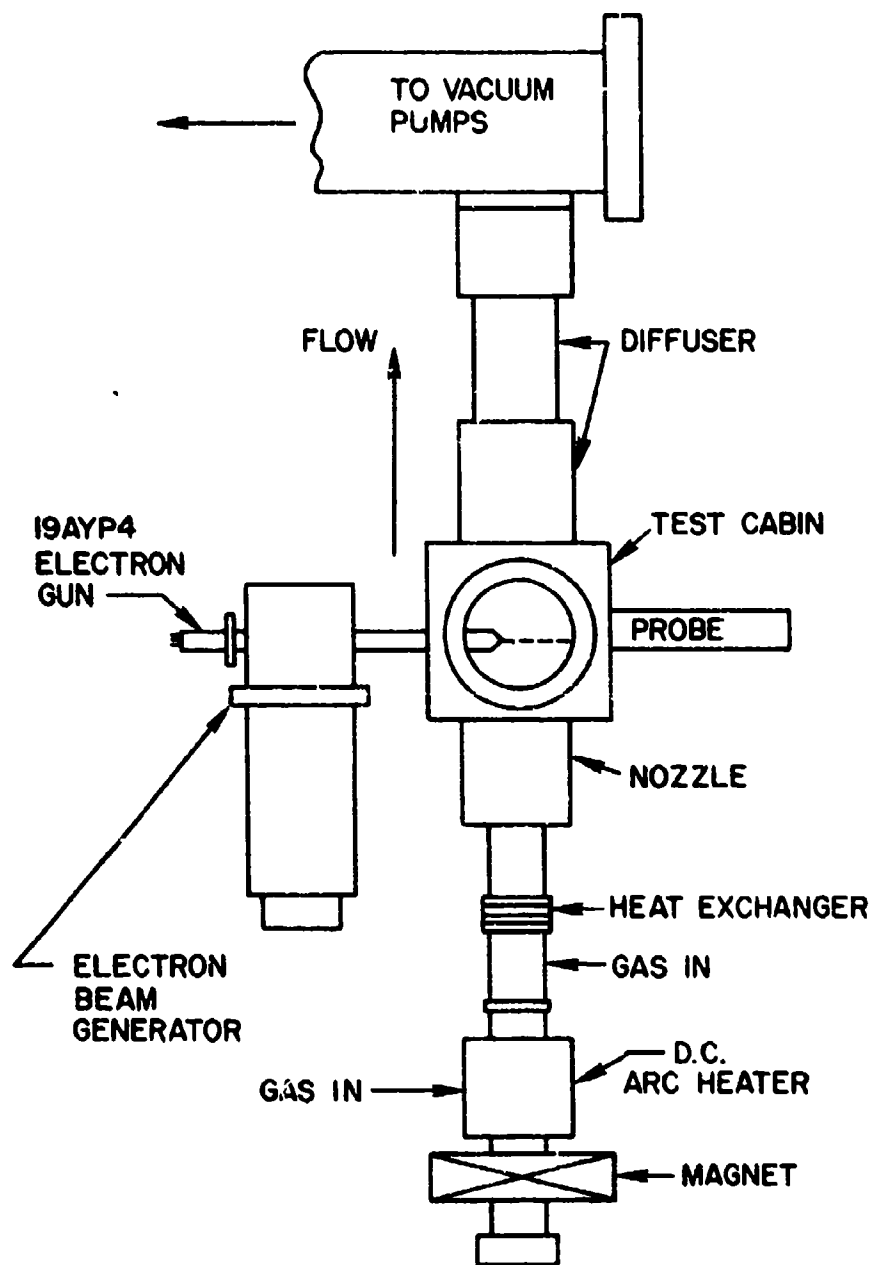


Figure 9. Arc-tunnel schematic

1 torr; hence, a "barrel-shock" system was generated by the highly under-expanded nozzle flow field. The electron beam was projected across the flow field at various distances downstream of the nozzle exit to provide test regions with static pressures varying from 1.5 to 60 torr and flow Mach numbers from 2.0 to 4.25.

The second nozzle (N2) had an exit expansion angle of 15° and delivered a flow with a nominal Mach number of 7.0. The nozzle exit diameter was 4.0 inches. Since the nozzle exit and test cabin pressures were nearly matched for this nozzle, the axial and radial gradients in flow properties were much less than those for the first nozzle. The electron beam was projected across this flow 1.0 inch downstream of the nozzle exit.

Wind tunnel reservoir conditions were determined by measuring the reservoir pressure and the total mass flow rate and assuming complete thermodynamic and chemical equilibrium from the reservoir to the nozzle throat. Under these conditions, the mass flow rate and reservoir pressure are uniquely related to the reservoir enthalpy.

In nozzle N1, the electron beam was generated by a commercially available 19AYP4 television electron gun. Beam currents of approximately 0.5 mA at voltages near 15 kV were employed. A detailed description of this beam generator and some of the special operating procedures required are discussed in Ref. 24. For nozzle N2, the electron beam was produced by a duoplasmatron generator described in Ref. 5. This generator provided beams with currents up to 10 mA at voltages near 20 kV. For both beam generators, the entire generator system was electrically isolated from the wind tunnel, so that no special beam collecting devices were required.

B. INSTRUMENTATION

1. General

The wind tunnel was instrumented to record static and total pressures, mass flows, and inlet gas temperatures. Reservoir pressures, test section pressures, and pitot pressures were obtained with variable reluctance differential pressure transducers. All pressure transducers were connected to a vacuum reference which was held at approximately .005 torr. The transducers were calibrated against a silicone oil micromanometer.

Primary (arc-heated) and secondary (cold gas injection) mass flow rates were monitored by measuring the differential pressure drop across calibrated orifice plates. The pressure drops were measured with variable reluctance pressure transducers.

2. Optical System

Rotational and vibrational spectra were obtained with a Jarrell-Ash 0.5 Meter Ebert scanning spectrometer. The grating was ruled with 30,000 lines/inch yielding a dispersion of 16 Å per millimeter and a maximum resolution of 0.2 Å. An uncooled EMI 6256 photomultiplier was used with the spectrometer. A schematic of the optical system is given in Fig. 10.

The image of the electron beam was focused on the entrance slit of the spectrometer by a 13 in. focal length, 2-1/2 in. diameter quartz lens. The electron beam was oriented perpendicular to the entrance slit. Photocurrents were measured and amplified by a Keithley Model 417 picoammeter. The output of the amplifier was entered into the signal conditioning system of the AARL Digital Computer and Data Acquisition System.

The electron beam current was continually monitored by a second photomultiplier-spectrometer system. Radiation from the electron beam was focused on the entrance slit of a 0.25 meter Jarrell-Ash spectrometer set to view the head of (0,0) band of the N_2^+ first negative system. During all spectral scans, the output from the 0.5 meter spectrometer was divided by that from the 0.25 meter spectrometer to account for variations in beam current and gas density during the wavelength scan. All data reported here were obtained in this manner.

3. Data Acquisition System

The experimental data were collected with the AARL Digital Computer and Data Acquisition System. This system is employed for on-line data acquisition, facility control and data reduction, as well as for conventional digital numerical processing. For these tests, a medium speed, auto-ranging amplifier and analog-to-digital (A/D) converter system was employed. The A/D converter resolves each data signal to 11 digital bits plus a sign bit. Hence, the accuracy of the converter is $\pm .0489\%$ of full scale on all gain ranges. Full scale voltage is adjustable from .005 to 1.0 V in 8 steps. The appropriate gain is automatically selected by the computer program operating the system to maximize data accuracy.

Data were obtained by scanning all data channels sequentially 20 times and averaging the recorded voltages for each channel. One scan sequence was completed in approximately 200 ms. The average voltages, percent deviation of voltage, and reduced data were displayed on a cathode ray tube terminal for operator inspection. The display was updated every 5 seconds. Selective scans were saved on magnetic tape and in a disc file for print-out at the conclusion of the run.

Pitot pressure surveys across the test section were obtained with an analog plotter driven by two digital-to-analog converters. The raw pressure data from the transducer were obtained, digitized, and reduced to pressure ratio (pitot pressure/reservoir pressure) on-line and the

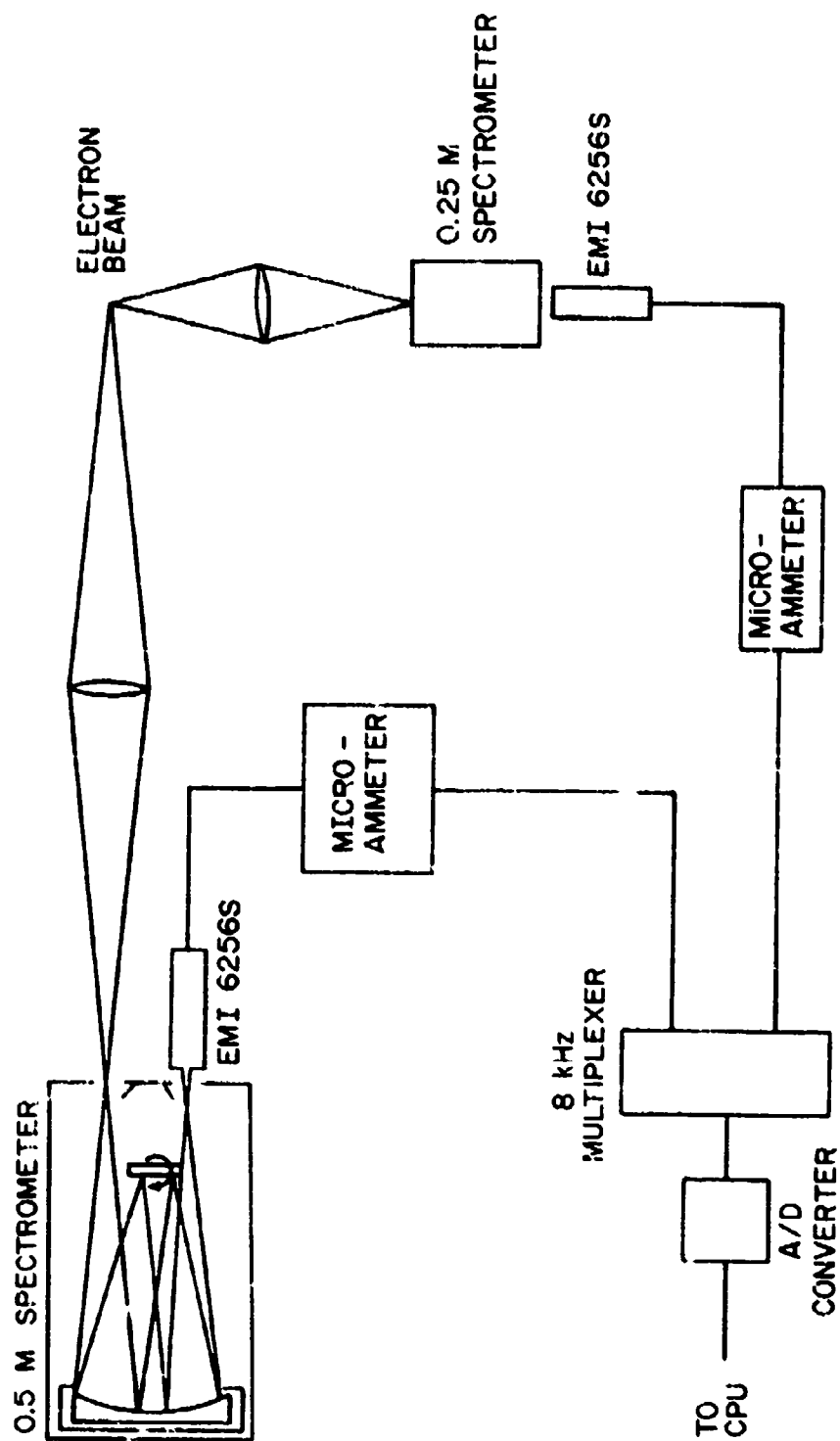


Figure 10. Instrumentation schematic

results were displayed on the plotter in real time. The local probe position within the test section was determined from the voltages obtained from a potentiometer connected to the probe drive mechanisms and were used to drive the horizontal axis of the plotter.

Wavelength scans were obtained by displaying the digitized photomultiplier outputs on the CRT screen. The spectrometer was scanned from high to low wavelengths at a constant speed. For rotational temperature measurements, the scan speed was 10 Å/min while for vibrational temperature measurements it was 50 Å/min. The corresponding slit widths were 50 and 150 μm, respectively. Reduced rotational temperatures and integrated vibrational band intensities were then computed on-line immediately after each data scan.

IV. RESULTS AND DISCUSSIONS

A. STATIC CHAMBER TESTS

The rotational structure of the bands in the N_2^+ first negative system were examined in detail in the static chamber at a static temperature of 290 K and with pressures ranging from 0.2 to 25 torr. Comparative scans of the rotational structure of the (0,0) band of the N_2^+ first negative system at low and high densities are shown in Fig. 11. The only apparent effect of elevated density on the rotational structure is the increased intensity of the rotational lines corresponding to K' values of 16-19. This is due to overlap by the (3,6) band of the N_2 second positive system. Line-slope plots for the data of Fig. 11 are given in Fig. 12. The plot of $\ln[I/S_K'(G)v^4]$ against $K'(K' + 1)$ should be linear with a slope inversely proportional to the rotational temperature. The low density data display such linearity. However, the linearity of the line-slope plots at high density is degraded due, in part, to the overlap by the (3,6) second positive band.

The measured rotational temperatures are plotted against the static pressure in Fig. 13. The indicated rotational temperature increases rapidly from the known value (290 K) as the pressure is increased, reaching a nearly constant value of 355 K at pressures over 3 torr. The scatter of the data in Fig. 13 increases rapidly as the pressure is raised above 3 torr. This scatter is greater than that attributed to basic uncertainties in determining the rotational temperature from the line-slope plots.

Various modifications to the test chamber were made in an attempt to reduce the rotational temperatures measured at high densities. In particular, the nitrogen test gas was injected into the chamber through a one-inch diameter copper tube oriented with its axis perpendicular to the electron beam and with the tube exit within approximately 0.5 in.

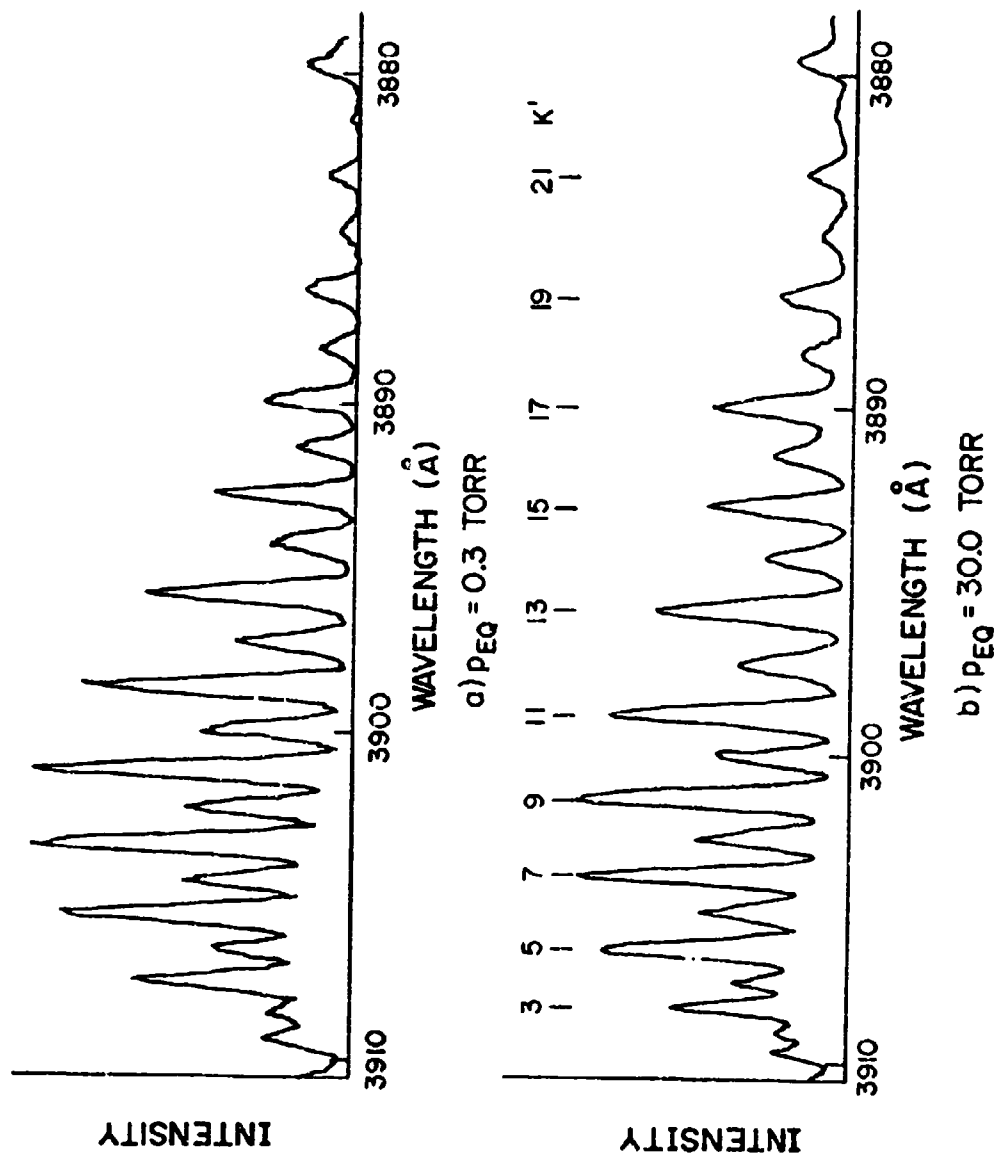


Figure 11. Rotational structure of the N_2^+ first negative (0,0) band

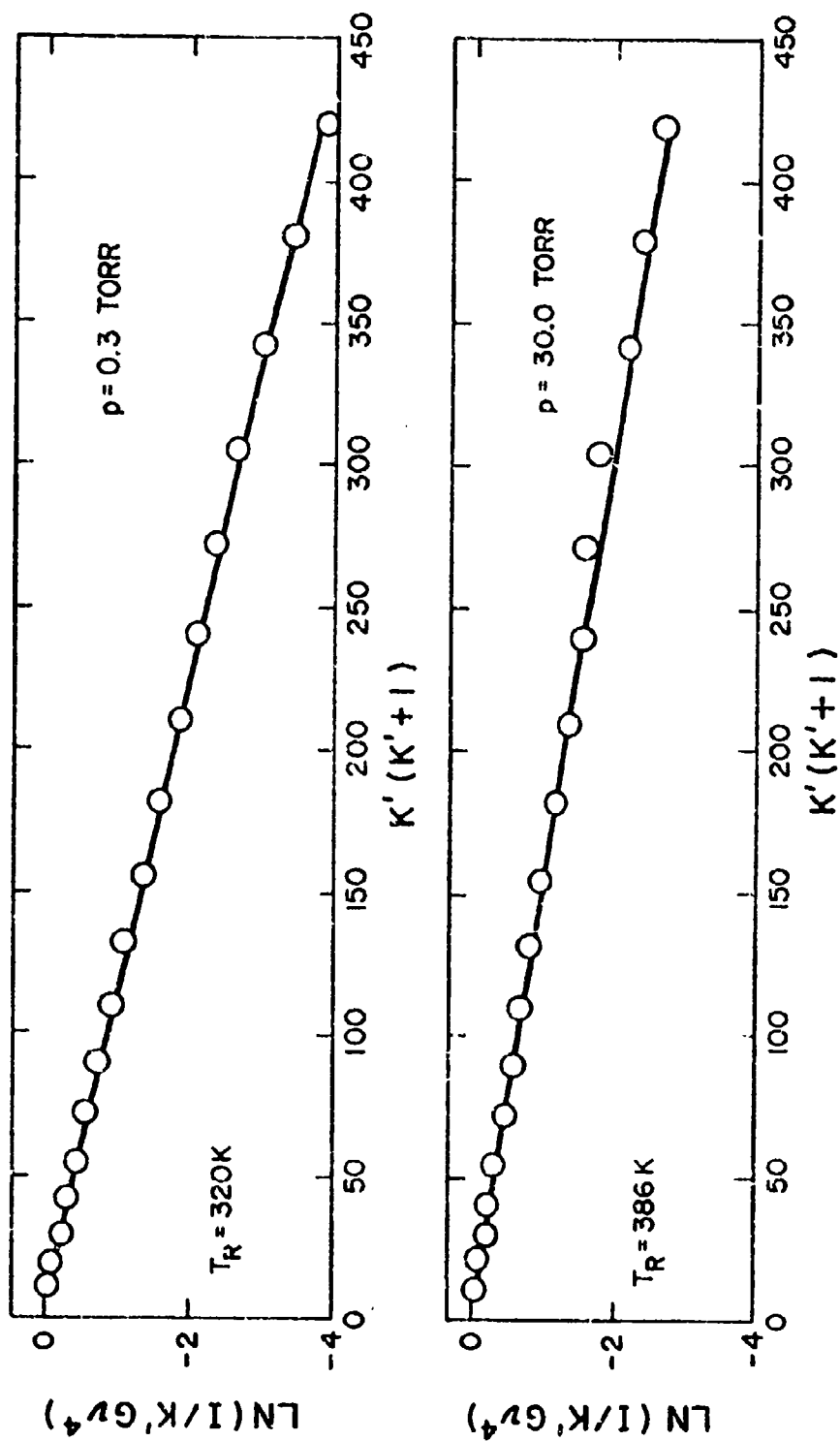


Figure 12. $N_2^+(0,0)$ line-slope plots from the static chamber

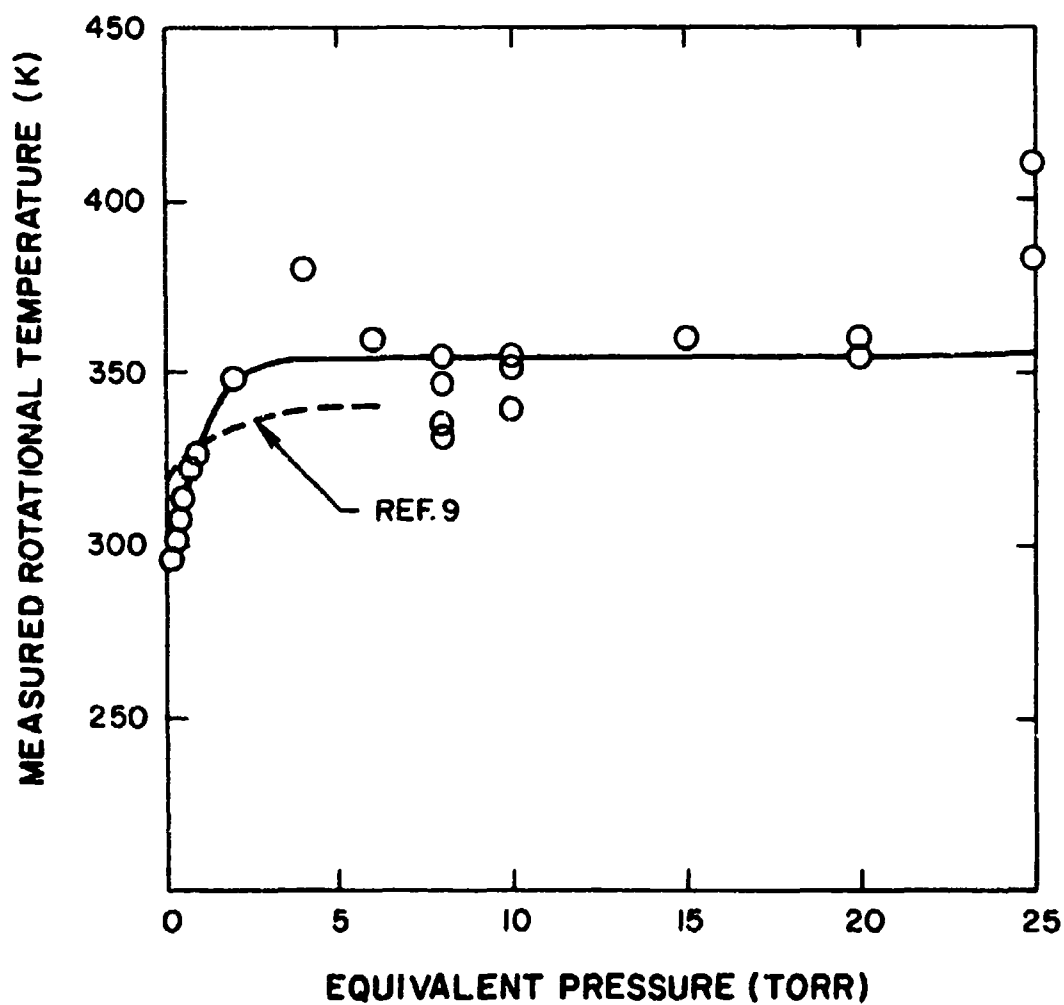


Figure 13. N_2 rotational temperatures measured in the static test chamber

of the beam. The flow velocity through the tube was estimated to be approximately 30 ft/s. This was done in an attempt to remove secondary electrons and low energy ions created by the beam excitation process from the region of observation and to reduce the possibility of heating of the ambient gas by the electron beam. This had a negligible effect on the measured rotational temperatures.

Excitation by low energy particles (secondary electrons, ions, and metastable molecules and atoms) and collision quenching are the most probable causes for errors in rotational temperature at high density. Of these two, excitation by low energy particles is the most likely. The line-slope plots of Fig. 12 display reasonable linearity when the overlap of the (3,6) band of the second positive system is systematically removed from the data. In addition, visual observations of the gas within the test chamber at high densities indicated a large degree of excitation occurred in regions far removed from the electron beam. This visual observation, coupled with the large number of charged particles collected by the drift tube of the electron beam generator (which necessitated control of the potential difference between the drift tube and test chamber), support the conjecture that the rotational temperature error in this case is due to excitation by low energy particles.

The data of Ashkenas⁹ obtained in a static chamber at a temperature of 300 K are compared with the present data in Fig. 13. The correlation formula developed by Ashkenas over-estimates the rotational temperature error of low densities and is in qualitative agreement with the errors observed here at high densities. However, if the errors are due to excitation by secondary particles, the amount of excitation will depend strongly on the geometry of the test chamber, the method of gas injection, the electrical condition of the chamber walls, the method of collection of the high energy electrons, etc.

It is notable that there are about as many empirical corrections to convert measured rotational temperatures to actual gas temperatures as there are investigators who have reported such results. Maguire¹¹ obtained different errors than those reported by Ashkenas⁹ and Robben and Talbot.² Hickman¹⁵ modified Muntz's original model of the excitation-emission process in an attempt to describe the rotational temperature errors, particularly for temperatures below 100 K. However, the Hickman model removes only some of the error. Maguire's free jet data indicate that the errors are due to selective quenching of the rotational energy levels, rather than excitation by low energy particles.

The cause for the errors in rotational temperature measurement at low static temperatures is still unresolved and no attempt has been made here to contribute to the understanding of this problem. However, it is clear that all measurements taken in a static test chamber are suspect due to excessive excitation of the N_2^+ first negative system by low energy particles which remain within the region of observation for undetermined lengths of time. Since the energy (velocity) of these

exciting particles is low, the excitation process occurs over a much greater time span than the excitation by beam electrons. Hence, there is a high probability that energy will be exchanged between the exciting particle and the rotational and vibrational energy modes of the molecule before the electronic transition occurs. In this case, the rotational and vibrational population distributions can be altered, leading to indicated rotational and vibrational temperatures which bear little relationship to the gas transitional temperature. The excitation may also result in a non-Boltzmann population distribution so that a temperature for the affected energy mode cannot be defined.

The ratio of intensities of the (0,1) and (1,2) bands of the first negative system is plotted vs. pressure in Fig. 14. The theoretical analysis predicts a band intensity ratio equal to 7.60. However, the ratios measured in the static chamber monotonically increase as the pressure is raised.

A dramatic change in the structure of the (0,1) band is observed as the pressure is increased. Comparing the low-density profiles of Fig. 2 with the same band intensity distribution at 20 torr given in Fig. 15 shows a large increase in the apparent intensity of the R-branch. This is due to overlap by the (1,5) band of the N_2 second positive system. It is well known that the second positive system is excited primarily by low energy (3 eV) electrons.¹¹ Hence, an abnormally high secondary electron concentration trapped within the static test chamber will lead to large intensities in the second positive system.

It is observed (Fig. 15) that the P-branch of the (0,1) band is largely unaffected by the overlap of the (1,5) band. Hence, the ratios of intensities of the P-branch portions of the bands were investigated as a means of determining vibrational temperatures in the presence of overlap due to the second positive bands. Theoretical predictions of integrated P-branch intensity ratios were made with results similar to those given in Fig. 4.

The ratio of integrated P-branch intensities for the (0,1) and (1,2) bands measured in the static test chamber are shown in Fig. 16. The P-branch ratio is seen to be nearly constant for equivalent pressures up to 35 torr, although there is a large amount of scatter in the data. This scatter is due primarily to difficulties in determining the (1,2) P-branch intensity. The P-branch intensity was assumed to include the band from the head to the point of minimum intensity between the P and R branches. As seen in Fig. 2, the division between the two branches is well defined for the (0,1) band but not for the (1,2) band. However, since the integrated P-branch ratio shows no trend with density, it may provide a means of measuring N_2 vibrational temperature in the presence of band overlap providing the scatter in the intensity measurements can be reduced to an acceptable value.

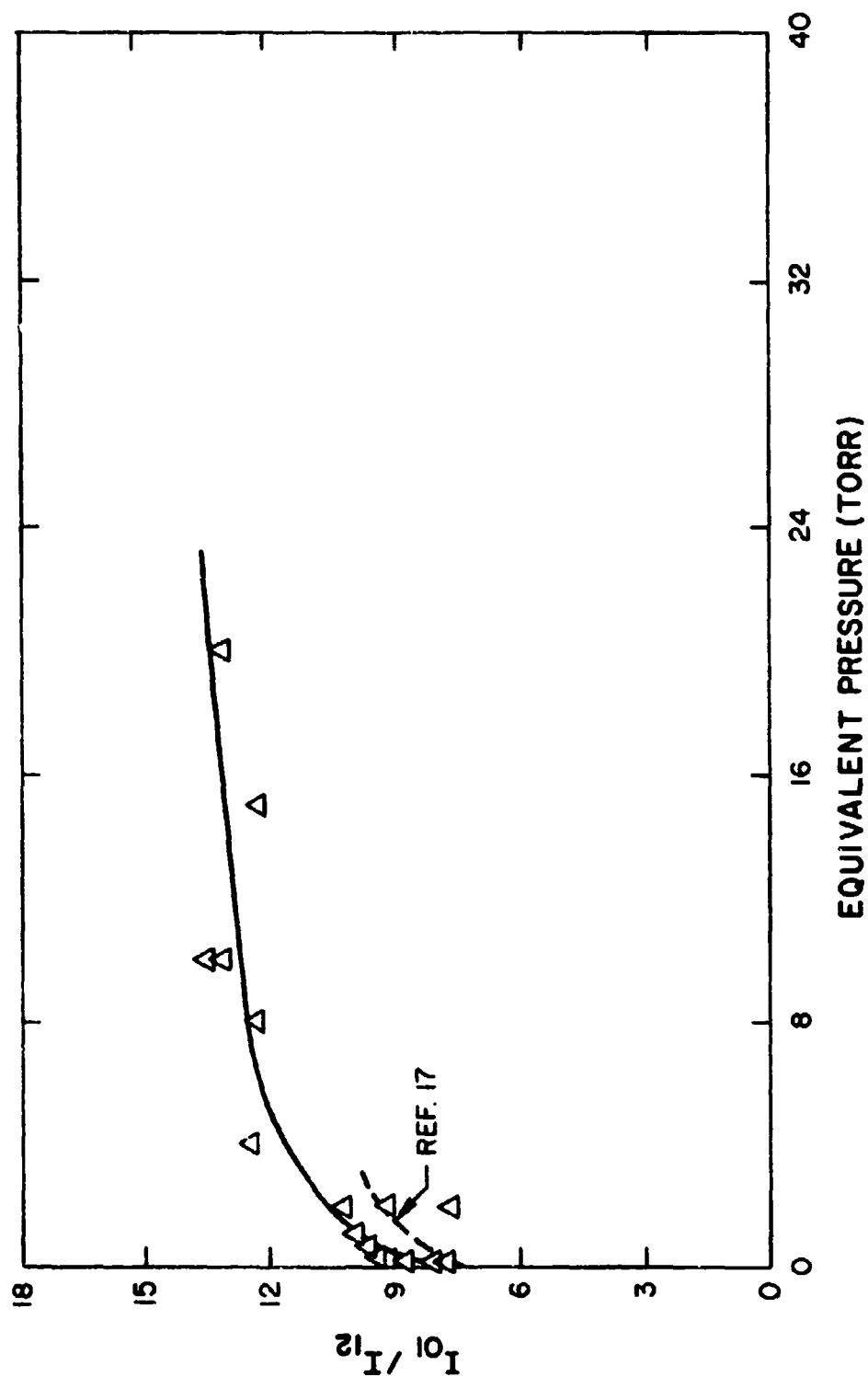


Figure 14. N_2^+ (0,1)/(1,2) total intensity ratios measured in the static test chamber

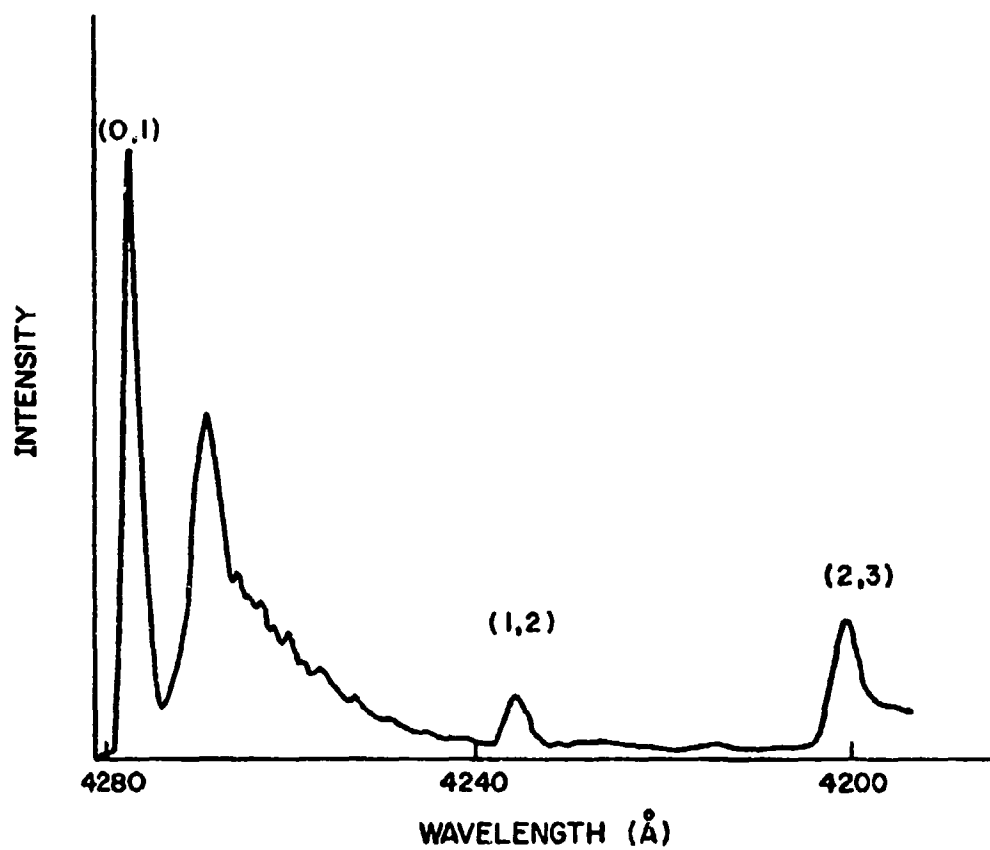


Figure 15. N_2^+ first negative (0,1) band sequence intensity measured in the static test chamber

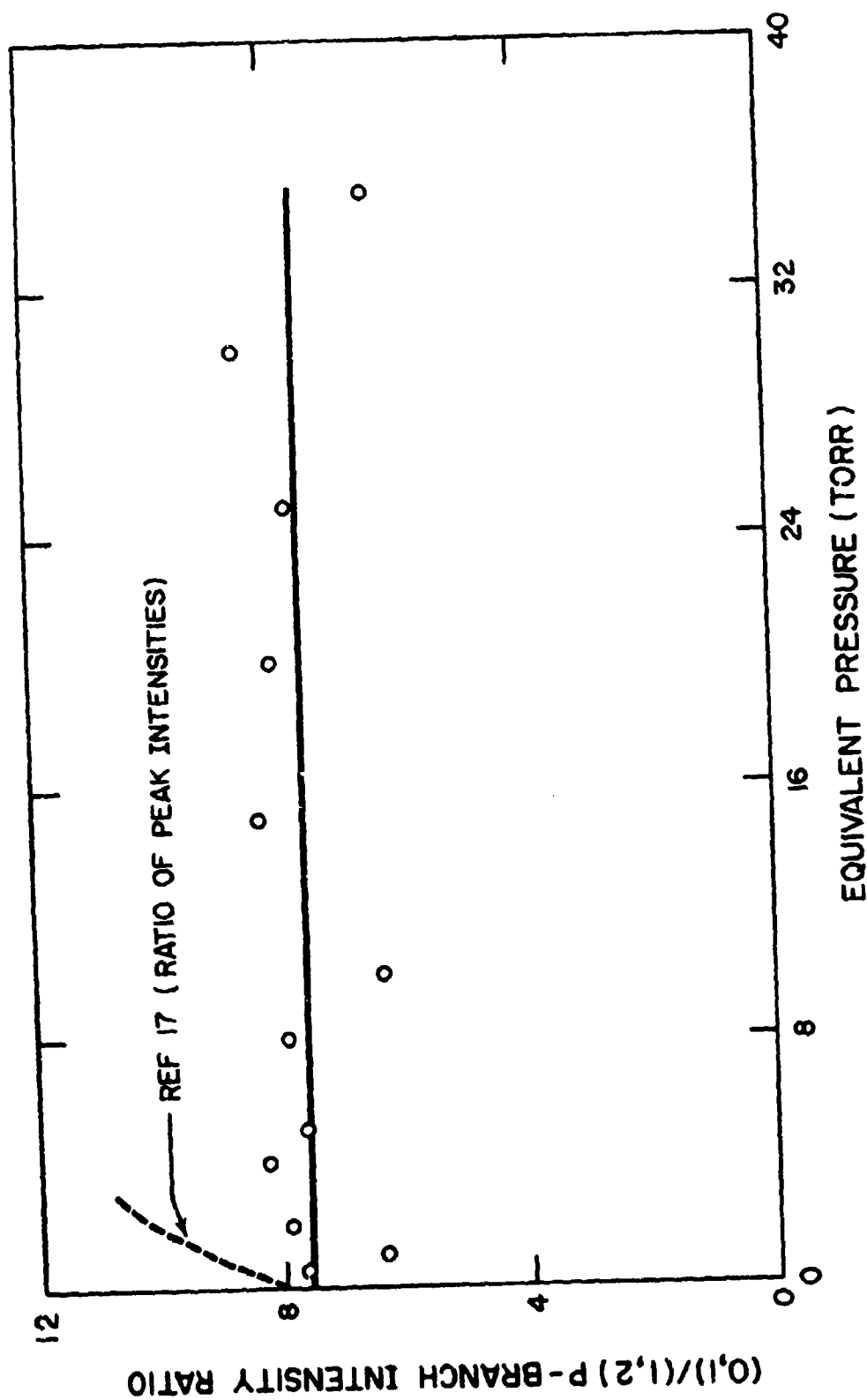


Figure 16. N_2^+ (0,1)/(1,2) P-branch intensity ratios from the static test chamber

Data obtained by Harbour¹⁷ are compared with the present data in Figs. 14 and 16. Harbour performed experiments in a static chamber with molecular nitrogen at a temperature of 296 K, a beam voltage of 15 kV, and beam currents near 0.15mA. Both total band intensities and band peak intensities were measured for the (0,1) and (1,2) bands. Harbour's data display the same basic trend as reported here - an increase in intensity ratio with increasing gas density. Harbour's ratio of band peaks should be free of overlap by the (1,5) band of the second positive system and should vary with gas density in the same manner as does the ratio of P-branch intensities, if there are no mechanisms other than band overlap which contribute to the variation in intensity ratios with density. However, Harbour's ratio of band peaks increases more rapidly with density than does the P-branch intensity ratio of the present studies. Since the rotational temperature measurements show an apparent change in the rotational intensity distribution within the (0,0) band at high densities, it is likely that similar changes occur in all bands of the first negative system. Hence, band peak intensities and integrated intensities may not vary in the same fashion as the gas density is increased.

It is concluded that the static test chamber experiments are of little value in judging the overall applicability of the electron beam method at high density. The no-flow conditions within the chamber lead to excessively high concentrations of secondary electrons, low energy ions, and molecules in metastable energy states. These particles will excite ground state nitrogen molecules with a "collision-time" which is much longer than that associated with excitation by beam electrons. During the relatively long excitation time, re-distribution of the energy within the rotational and vibrational energy states can occur before the molecule makes a transition to the $N_2^+B^2\Sigma$ state. Hence, the basic assumptions of the excitation-emission analysis used to interpret the observed line and band intensities in terms of rotational and vibrational temperatures are no longer applicable. It is apparent that reliable calibration experiments can be conducted only in flow fields with velocities sufficient to sweep the low energy particles out of the region of observation.

In the present studies, the apparently large contribution of excitation by low energy particles to the observed radiation which causes significant overlap of the N_2^+ system by bands of the N_2 second positive system completely overshadows any effects of selective quenching of the particles in the $N_2^+B^2\Sigma$ state.

B. WIND TUNNEL STUDIES

1. Nominal Run Conditions

For nozzle N1, wind tunnel data were obtained at nominal axial locations downstream of the nozzle exit equal to 0.10, 1.5, and 2.0 inches. Since much lower axial gradients in flow properties existed in

nozzle N2, data were collected for this nozzle only at a location 1.0 inch downstream of the nozzle exit.

The 1.5 and 2.0 inch stations of N1 were within the strong expansion system emanating from the nozzle exit caused by the large pressure unbalance between the nozzle exit and test cabin static pressures. In this region of the flow field, large axial and radial gradients in all flow properties exist. To ensure that probe and electron beam data were taken at the same position within the flow field, the electron beam was always positioned such that it intersected the tip of the probe while the probe was positioned on the tunnel centerline. The beam position was adjusted with a deflection coil mounted between the exit orifice of the drift tube and the test region. Once the proper alignment was achieved, the pitot probe was withdrawn and spectral data were collected.

To evaluate the accuracy of the electron beam measurements taken in the arc-heated facility, a reliable model of the expansion process from the reservoir to the measuring station must be available. Computations with a computer program which is a modification of that described by Lordi²⁶ showed that chemical freezing was to be expected early in the expansion process. Hence, vibrational relaxation was the only kinetic mechanism of importance.

Theoretical estimates of gas properties including the effects of vibrational relaxation were obtained from a modification of the time dependent method of Anderson as summarized in Ref. 27. In this case, the relaxation of the vibrational energy mode is assumed to be described by the harmonic oscillator model. That is,

$$dE_v/dt = (E_v^e - E_v)/\tau_e \quad (26)$$

where E_v is the local vibrational energy, E_v^e is the vibrational energy evaluated at the local translational temperature, and τ_e is the effective vibrational relaxation time. In a multi-species gas it is common to evaluate τ_e with a "parallel resistance" mixture rule. For example, in N_2 - O_2 mixtures, τ_e would be given by

$$1/\tau_e = X_{N_2}/\tau(N_2-N_2) + X_{O_2}/\tau(N_2-O_2) \quad (27)$$

In mixtures of N_2 and O_2 , theoretical and experimental results¹⁶ show that both gas species relax with the same effective relaxation time.

Values for τ_e have recently been determined by Sebacher¹⁶ for N_2 relaxing in both pure N_2 and in air. The N_2 - N_2 and N_2 -air rates are given by

$$P\tau_{N_2-N_2} = 3.4 \times 10^{-12} \exp(195T^{-1/3}) \quad (28)$$

and

$$p\tau_{N_2-air} = 1.2 \times 10^{-10} \exp(130T^{-1/3}) \quad (29)$$

where τ is in seconds, p is in atmospheres, and T is in degrees kelvin. These rates were determined in Ref. 16 from a set of measurements obtained with an electron beam in high speed N_2 and air flows at gas densities well below those necessary to apply the electron beam method without complications due to quenching and excitation by secondary particles. Further experiments are reported in Ref. 29 where the N_2 rate of Ref. 16 was employed with the computer program of Ref. 27 to establish N_2 vibrational relaxation rates. The notable feature of the relaxation rates given in Refs. 16 and 29 is that they distinguish between relaxation of N_2 in air and in pure N_2 . This is contrasted with the earlier correlations of Ref. 15 where a single vibrational relaxation rate was used for both gases. The rate given in Ref. 15 to be applied to both N_2 and air flows is

$$\tau_p = 3 \times 10^{-12} \exp(181 T^{-1/3}) \quad (30)$$

The relative influences of the rates given by Eqs. (28) and (30) on the predicted N_2 vibrational and gas translational temperatures are shown for nozzle N1 in Fig. 17. It can be seen that the single rate given by Eq. (30) leads to less vibrational relaxation and, hence, to a higher vibrational temperature than does the rate of Eq. (28). Since different rates of N_2 vibrational relaxation in air and N_2 flows are anticipated, the appropriate rate of Eq. (28) or (29) was used in all calculation of these studies.

The computer program of Ref. 27 was employed for these studies because it includes the effects of vibrational relaxation on the entire flow field; that is, the energy changes accompanying vibrational relaxation are included in the overall energy balance for the system. The various kinetic rates given in Ref. 28 were employed except for the N_2 - N_2 rate. The rate given by either Eq. (28) or (29) was used in place of the N_2 - N_2 rate and the vibrational energy of O_2 was assumed equal to that of N_2 . While this latter assumption gives a poor representation of the O_2 vibrational energy, the overall effects of the vibrational relaxation on the translational energy are minor. This can be seen in Fig. 17 where the effects of varying the N_2 rate lead to very little change in the translational temperature.

The conditions of Fig. 17 correspond to the highest reservoir temperature encountered before significant oxygen dissociation occurs in the flow field. As the reservoir temperature decreases, the amount of vibrational relaxation present in the flow decreases, as does the sensitivity to the particular rate equation used. For many of the wind tunnel run conditions of these studies, little differences exist between the test-section vibrational and translational temperatures predicted with any of the rate equations.

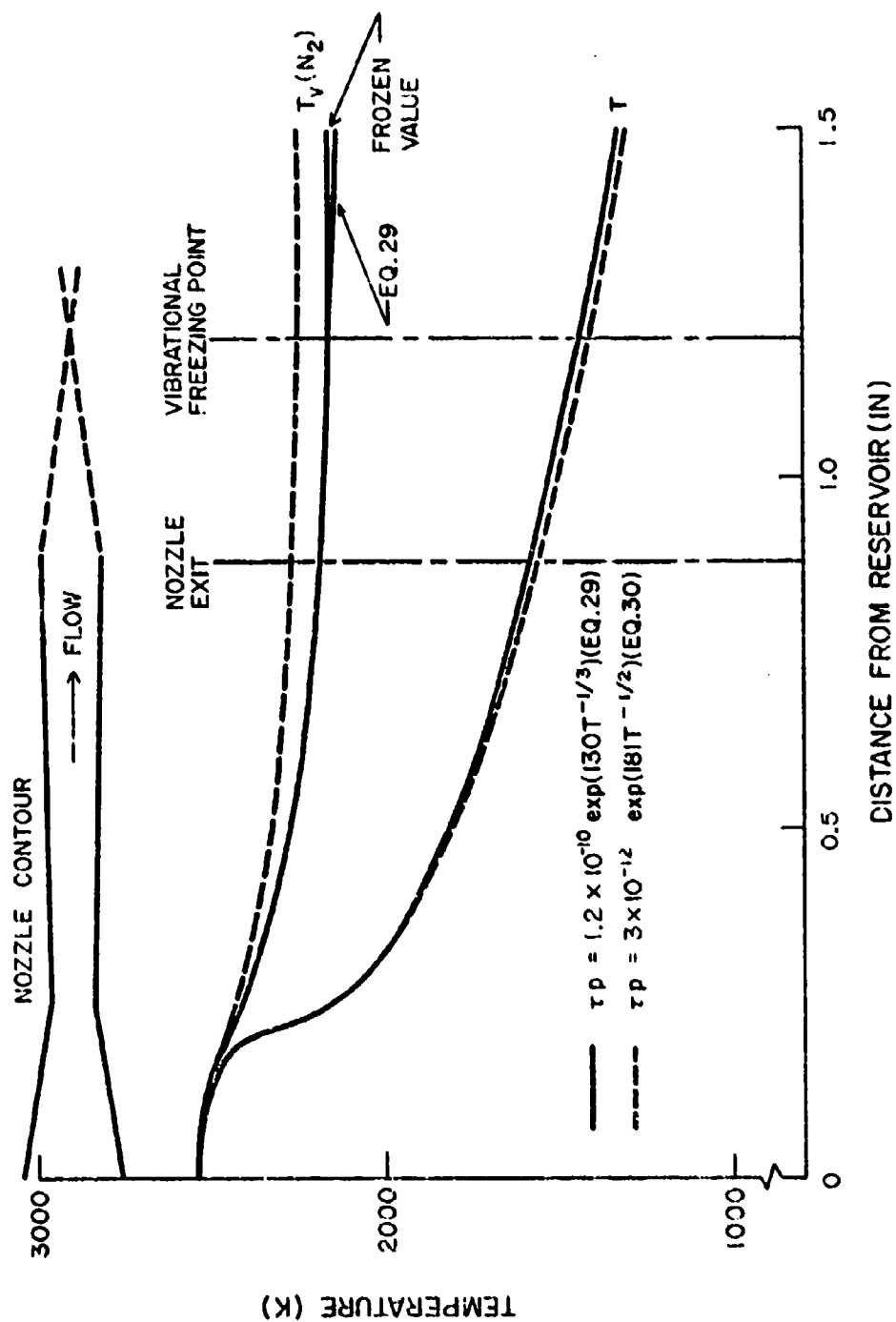


Figure 17. Theoretical temperature distributions; $p_0 = 0.8$ atm; $T_0 = 2560$ K; run 52; nozzle NI.

At reservoir temperatures much higher than that of Fig. 17, significant oxygen dissociation occurs so that the assumption of equal nitrogen and oxygen vibrational energies has even less effect on the overall energy balance. The main effect of high reservoir temperatures is to decrease the oxygen concentration so that the second term in Eq. (27) becomes negligible. In this case, the rate given by Eq. (28), rather than that of Eq. (29), should be used.

To implement the computer program of Ref. 27 for the present studies, the CO_2 and H_2O concentrations inherent in the program must be set to small values. No difficulties were encountered in setting the H_2O mole fraction to zero. However, numerical difficulties were encountered when the CO_2 concentration was set to zero. A brief set of numerical experiments was performed to establish a minimum mole fraction of CO_2 which would allow execution of the program. This value was determined to be approximately 10^{-15} . Increases in the minimum value by at least seven orders of magnitude had no effect on the N_2 vibrational and translational temperatures to four significant digits.

When the low area ratio wind tunnel nozzle (N1) was used, the high pumping capacity of the vacuum system led to a strong expansion system at the nozzle exit for all run conditions. Since the expansion system causes very rapid decreases in flow temperature and density, it is unlikely that the vibrational energy mode will relax sufficiently fast enough to respond to these rapid changes in flow properties. Hence, the vibrational relaxation was assumed to proceed only downstream to the point where the leading expansion wave from the nozzle exit crossed the nozzle centerline. All vibrational temperatures downstream of this freezing point were assumed to be equal to their values at the freezing point. As can be seen in Fig. 17, the effect of this freezing is relatively minor and is important only for the data obtained at the farthest downstream axial position. For the high area ratio nozzle (N2) vibrational relaxation was assumed to proceed from the reservoir to the measuring station.

The gas conditions at the test stations were determined by measuring the local pitot pressures (p_{T2}). The theoretical model of Ref. 27 was modified to include a pitot pressure calculation. This was accomplished by assuming that the flow through the pitot probe shock wave was vibrationally frozen. A frozen speed of sound was calculated from

$$a_f = (\gamma R/MT)^{1/2} \quad (31)$$

where γ is the frozen ratio of specific heats, M is the molecular weight of the gas mixture, and T is the local static temperature. The Mach number obtained from a_f and the local velocity was then used in the isentropic formula for p_{T2}/p_1 , where p_1 is the static pressure upstream of the probe shock wave. The ratio of pitot and reservoir pressures was then obtained from $p_{T2}/p_0 = p_{T2}/p_1 \times p_1/p_0$; where p_0 is the reservoir pressure. The pitot pressure ratios measured on the tunnel centerline were matched with

those of this theoretical model to give all flow conditions at the measuring stations.

Typical pitot pressure surveys taken at the 0.1 and 2.0 inch stations of nozzle N1 are given in Fig. 18a while a typical survey for nozzle N2 is given in Fig. 18b. Representative reservoir conditions and predicted test section gas properties are summarized in Table II.

2. Overall Spectral Features

A wavelength scan of the entire spectral region of interest is shown in Fig. 19. These data were obtained at the 0.10 inch axial station of N1 at a reservoir temperature of 1600 K, a reservoir pressure of 0.8 atm, and an equivalent pressure near 20 torr. Hence, they correspond to the maximum gas density investigated in these studies. The scan is uncorrected for the spectral response of the optical system. Vibrational bands due to the N_2^+ first negative, N_2 second positive, and NO γ systems dominate the spectrum. Bands from the O_2^+ second negative system were also observed but with intensities much less than those of the N_2 and NO bands.

The radiation intensities observed at high densities are compared with those at the lower densities obtained with nozzle N2 in Fig. 20. The most notable difference between these two scans is the obvious appearance of relatively intense radiation in the O_2^+ second negative bands (particularly the (3,3) band) in the lower density data. This implies a significant difference in the relative quenching of the NO γ and O_2^+ second negative bands at high density which leads to severe overlap of the O_2^+ bands by those of the NO γ system. Sensitivity experiments were conducted to determine the operating conditions which allow O_2 vibrational temperature measurements to be made in the presence of NO and are discussed below.

3. N_2 Results

The rotational structures of the (0,0) and (0,1) bands of the N_2^+ first negative system were examined in detail to determine if excitation by secondary particles and preferential collision quenching disturb the band structure in a flow with high gas velocity. Scans of the R-branches of the (0,0) and (0,1) bands obtained in nozzle N1 at an equivalent pressure of approximately 20 torr and a rotational temperature of 786 K are shown in Figs. 21 and 22. The changes in the intensities of the rotational lines in the (0,0) band with rotational quantum numbers greater than 15 due to overlap by the (3,6) band of the N_2 second positive system are barely discernible in Fig. 21. In addition, there is no evidence of significant overlap of the (0,1) band by the (1,5) band of the second positive system.

The line-slope plot for the data of Fig. 21 is shown in Fig. 23. The departure from linearity is due primarily to interference of the P-branch lines with the R-branch lines caused by the high rotational temperature.

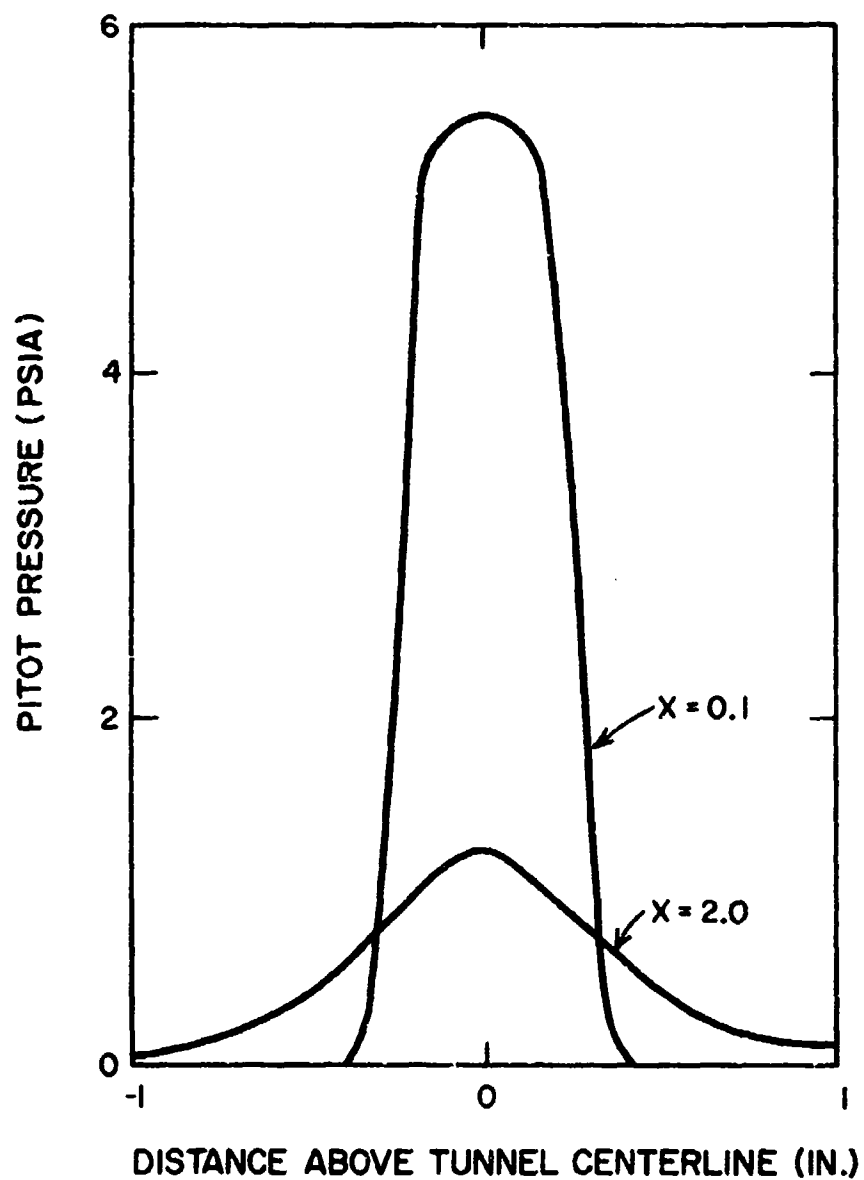


Figure 18a. Typical pitot pressure surveys in nozzle N1.
 X = distance downstream of nozzle exit in inches.

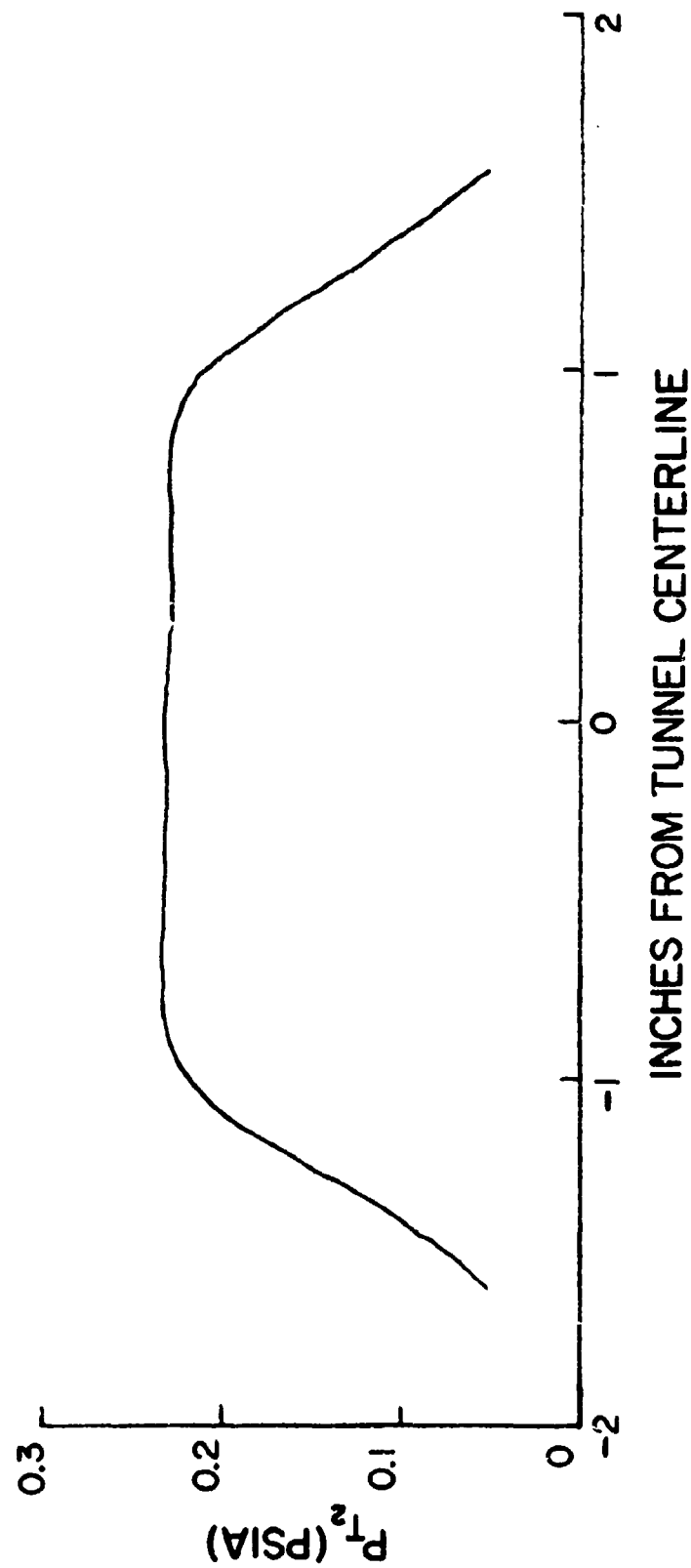


Figure 18b. Typical pitot pressure survey in nozzle N2;
1.0 inch downstream of nozzle exit.

Table II. Nominal Run Conditions

Inches Downstream Nozzle Exit	T ₀ (K)	P ₀ (atm)	p (torr)	T (K)	P _{EQIV} (torr)	Mach No.
Nozzle N1:						
0.1	2100	0.66	38.04	1006	11.3	2.3
	1700	0.95	59.3	809	22.0	2.3
1.5	1500	1.02	14.0	476	8.8	3.3
2.0	2600	0.82	4.7	648	2.2	4.0
	2100	0.70	1.63	401	1.2	4.6
	1700	0.89	1.92	318	1.8	4.7
Nozzle N2:						
1.0	5500	1.20	0.234	579	0.121	6.7
	3700	0.74	0.144	381	0.113	6.8
	2900	0.60	0.113	284	0.119	6.8

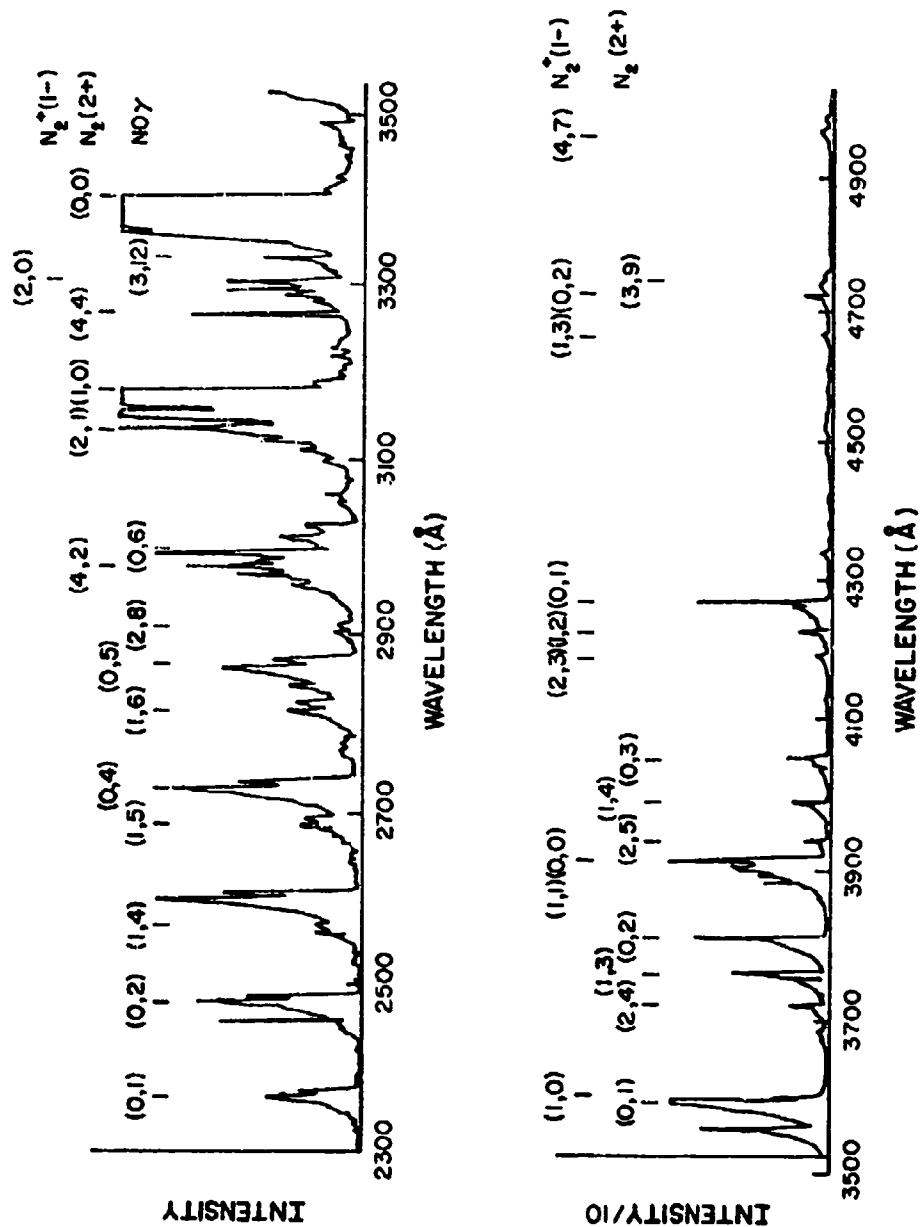
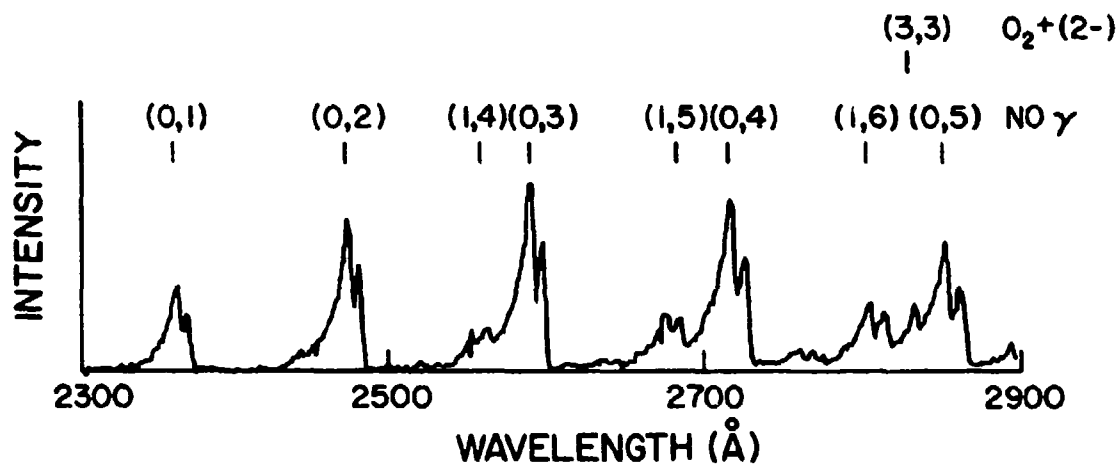
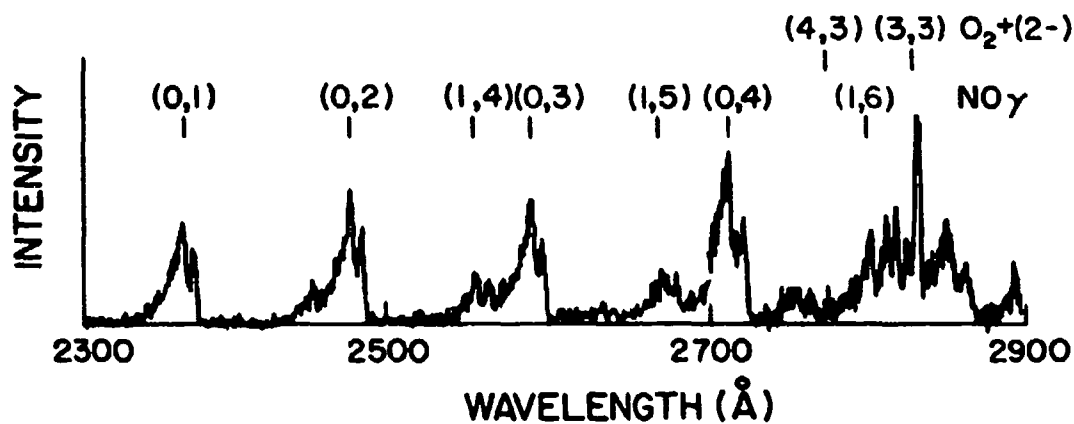


Figure 19. Spectral scans of electron beam induced emission in the arc-heated wind tunnel for nozzle N1; $P_{EQ} = 20$ torr.



a. Nozzle N1; $P_{EQ} = 20$ torr



b. Nozzle N2; $P_{EQ} = 0.18$ torr

Figure 20. Spectral scans of electron beam induced emission in the arc heated wind tunnel.

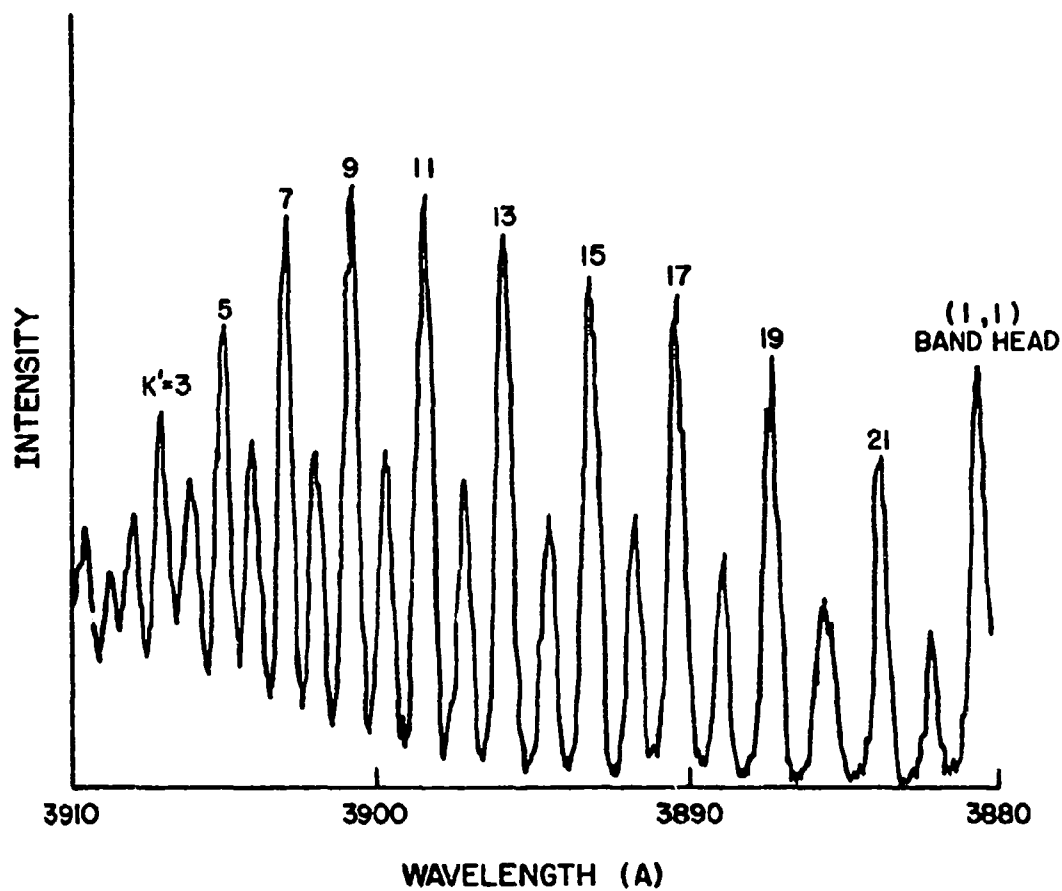


Figure 21. N_2^+ (0,0) band rotational structure from the wind tunnel; $p_{eq} = 20$ torr; nozzle N1.

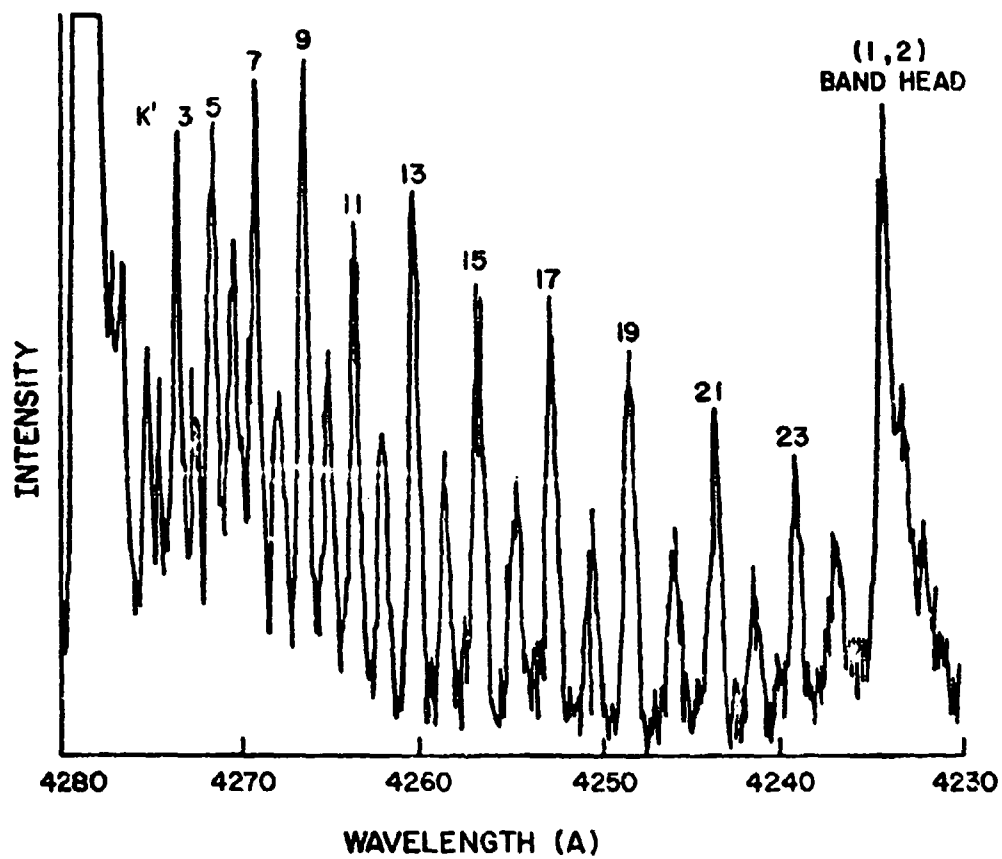


Figure 22. N_2^+ (0,1) band rotational structure from the wind tunnel; $p_{EQ} = 20$ torr; nozzle N1.

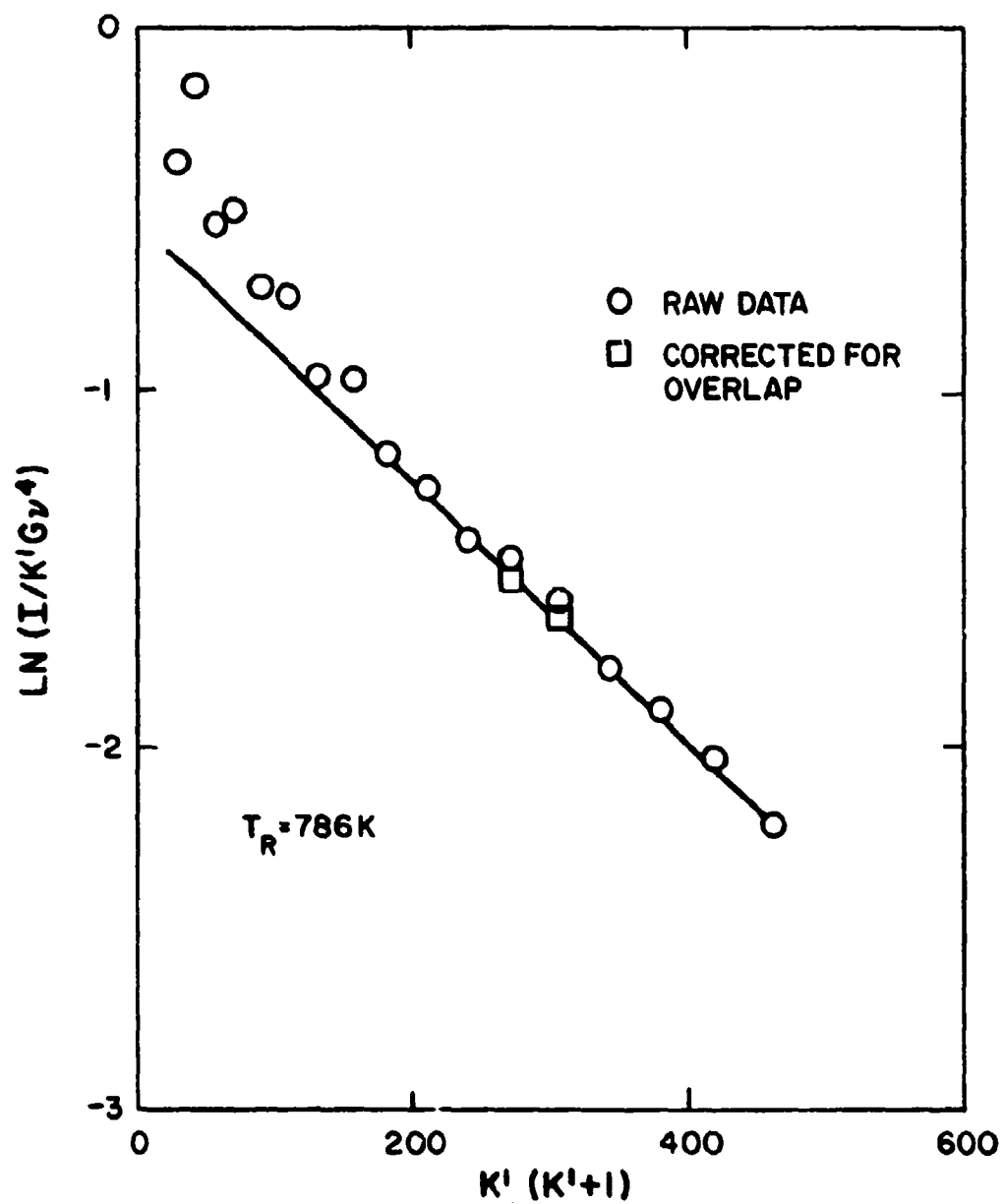


Figure 23. Line slope plot for data of Figure 21.

However, lines in the tail of the band which are relatively free of interference from the P-branch lines show reasonable linearity.

Analyses of these spectral details show that the excitation by secondary particles which dominate the measurements in the static chamber at these densities are not observable in the wind tunnel data. In addition, the significant overlap by the bands of the second positive system, which are excited primarily by secondary electrons, do not appear to contaminate the first negative bands in any significant manner.

A summary of the N_2 data obtained from the wind tunnel experiments is given in Table III. The measured vibrational temperatures are compared with the theoretical predictions in Fig. 24. The maximum scatter in the data of Fig. 24 amounts to $\pm 6\%$ and is due to accumulation of errors in determining the reservoir temperature from the measured mass flow rates and reservoir pressure, uncertainties in determining the rotational temperature from the line slope plot (for use with Fig. 4 to determine vibrational temperature), and inaccuracies in obtaining integrated band intensities.

A 5% error in mass flow rate will result in a 10% error in reservoir temperature. For these studies, errors in the measurement of both the primary and secondary mass flow rates contribute to the total error in reservoir temperature. Errors in determining the rotational temperature from the line slope plot are due primarily to uncertainties in fitting a straight line through the data. At high rotational temperatures (800 K), the interference of P-branch lines with the R-branch lines makes this determination more difficult than it is at lower temperatures. Under these conditions, the accuracy in measured rotational temperature is no better than approximately $\pm 6\%$. Hence, the scatter of the data evident in Fig. 24 is within the combined accuracy with which the measured and predicted vibrational temperatures can be determined with the present system.

The comparisons of the theoretical and experimental N_2 vibrational temperatures shown in Fig. 24 demonstrate the effect of gas composition on the rate of N_2 vibrational relaxation. In air flows, the τ_e given by Eq. (27) describes the rate of relaxation of both the N_2 and O_2 . Its value is less than that for pure N_2 but greater than that for pure O_2 . As the O_2 concentration decreases due to dissociation, τ_e increases, leading to less vibrational relaxation in the flow field.

The O_2 mole fractions at the various test conditions of these studies are shown as functions of the reservoir temperatures in Fig. 24. The data obtained with nozzle N1 correspond to O_2 mole fractions near 0.20, typical of low temperature air and the N_2 -air rate of Eq. (29) is expected to apply. However, the test conditions of nozzle N2 resulted in significant oxygen dissociation so that the N_2 - N_2 rate of Eq. (28) should apply, particularly at the higher reservoir temperatures. The measured N_2 vibrational temperatures shown in Fig. 24 agree with these

Table III. Run Summary - N₂ Data

Run	T ₀ (K)	P ₀ (atm)	P (torr)	PEQ (torr)	T _R (N ₂) (K)	T _V (N ₂) (K)	T _V (THEORY) (K)
Nozzle N1:							
52	2561	0.799	5.00	2.18	600	2182	2135
60	2106	0.658	39.5	11.3	902	1897	1914
61	1814	1.047	61.6	20.7	839	1634	1647
64	2104	0.724	43.6	12.5	-	1740	1898
68	2136	0.704	1.68	1.19	453	2000	1924
	1766	0.892	2.03	1.78	371	1701	1637
70	1456	1.020	14.48	9.18	626	1358	1377
85	2086	0.688	4.30	2.62	492	1890	1890
86	1497	1.024	6.40	4.81	398	1430	1416
	2121	0.671	4.20	2.52	498	1780	1909
87	1763	0.652	38.4	13.4	915	1620	1663
	1392	1.024	59.0	26.1	754	1189	1331
88	1973	0.672	2.23	1.56	452	1880	1817
	1616	1.048	3.38	2.42	419	1590	1510
Nozzle N2:							
3	4258	1.032	0.267	0.179	449	3300	3500
5	2866	0.594	0.111	0.119	279	2750	2650
	2974	0.615	0.116	0.119	292	3000	2730
6	3764	0.714	0.139	0.107	390	3250	3252
	3685	0.700	0.136	0.107	380	3430	3225

Table III. Run Summary - N₂ Data - (Continued)

Run	T _O (K)	P _O (atm)	P (torr)	P _{EQ} (torr)	T _R (N ₂) (K)	T _V (N ₂) (K)	T _V (THEORY) (K)
Nozzle N2: (Continued)							
7	3680	0.744	0.144	0.114	379	3260	3220
	3725	0.756	0.147	0.115	384	3330	3250
8	3686	0.988	0.192	0.152	380	3230	3230
	3825	1.013	0.198	0.149	397	3300	3280
9	3592	0.908	0.176	0.143	368	3120	3150
	3636	0.913	0.177	0.142	373	2600	3180
10	3427	0.745	0.143	0.124	346	3270	3005
	3514	0.768	0.148	0.124	358	3240	3100
12	3336	0.760	0.145	0.130	336	3070	3000
13	3541	1.036	0.200	0.166	361	3110	3110
	3584	1.061	0.205	0.168	367	3220	3130

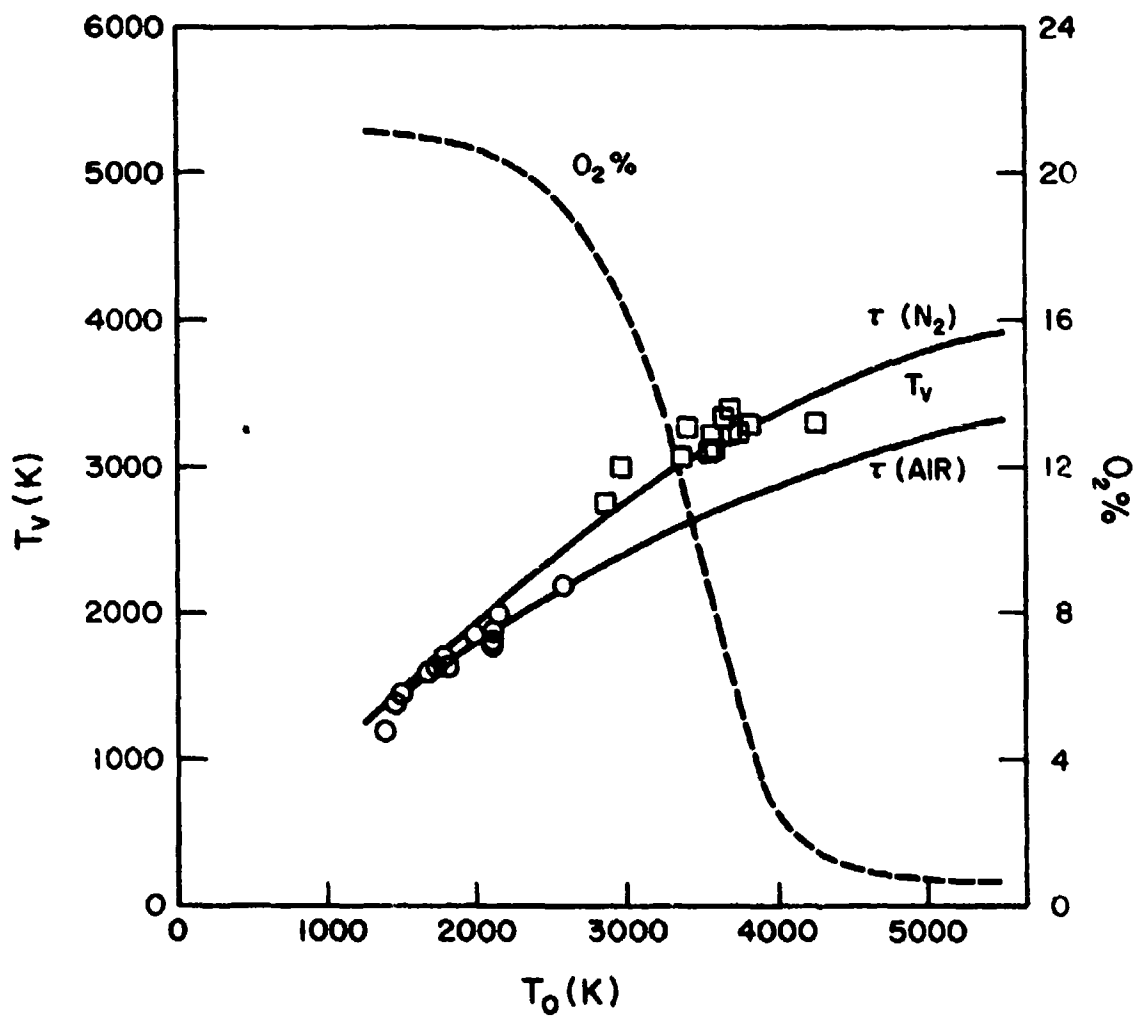


Figure 24. Measured and predicted N_2 vibrational temperature;
 ○ nozzle N1; □ nozzle N2; — theoretical T_v ;
 --- theoretical % O_2 .

trends. The low temperature data agree with theoretical predictions employing the N_2 -air rate while the high temperature data are in better agreement with theoretical results obtained with the N_2 - N_2 rate.

The analysis of the N_2 vibrational relaxation process used here allows for only one effective collision partner in de-activating the N_2 vibrational energy mode. A more general analysis should be formulated employing a rate in the form of Eq. (27) which allows for varying O_2 concentrations throughout the flow field. However, the aim of the present studies is to determine the accuracy with which vibrational temperatures can be measured over a wide range of flow densities. Hence, it was considered sufficient to obtain theoretical estimates of flow properties with the N_2 -air rate at the low reservoir temperatures of nozzle N1 while the N_2 - N_2 rate was used for the high reservoir temperatures of nozzle N2.

To investigate the possible effects of gas density on the measured N_2 vibrational temperatures, the ratios of the measured and predicted vibrational temperatures listed in Table III are plotted in Fig. 25 against equivalent pressure. No specific trend in the ratio of the measured and predicted temperatures with gas density is evident. At equivalent pressures greater than approximately 1 torr, the radiation in the N_2^+ first negative system is highly quenched by collisional mechanisms. However, the data of Fig. 25 demonstrate that the rotational and vibrational energy levels in the $N_2^+(B^2\Sigma)$ electronic energy state are not preferentially quenched nor are the data influenced by excitation by secondary particles in any measurable amount for equivalent pressures at least up to 20 torr.

4. Nitric Oxide Results

The ratios of intensities of the NO γ (0,4) and (1,5) bands obtained in the wind tunnel experiments are summarized in Table IV. The band intensity ratios are scaled by the value at 300 K as discussed previously to account for variations in the spectral sensitivity of the optical system. The corresponding N_2 theoretical vibrational temperatures are included to give an indication of the NO vibrational temperature. The theoretical N_2 vibrational temperatures are used because of the uncertainty in the vibrational relaxation rate for NO in expansion flows. While experimental excitation rates for NO are available from shock tube studies, the applicability of these rates in expansion flows is uncertain. It is well-known¹³⁻¹⁶ that vibrational excitation rates for N_2 greatly underestimate the vibrational relaxation in expansion flows. It is likely that similar effects occur in expanding NO.

The (0,4) and (1,5) band intensity ratios obtained at all run conditions are plotted in Fig. 26 against the N_2 theoretical vibrational temperature. Included in Fig. 26 are the theoretical band intensity ratios. The theoretical band intensity ratio for direct excitation is also shown scaled such that its room temperature value is equal to that

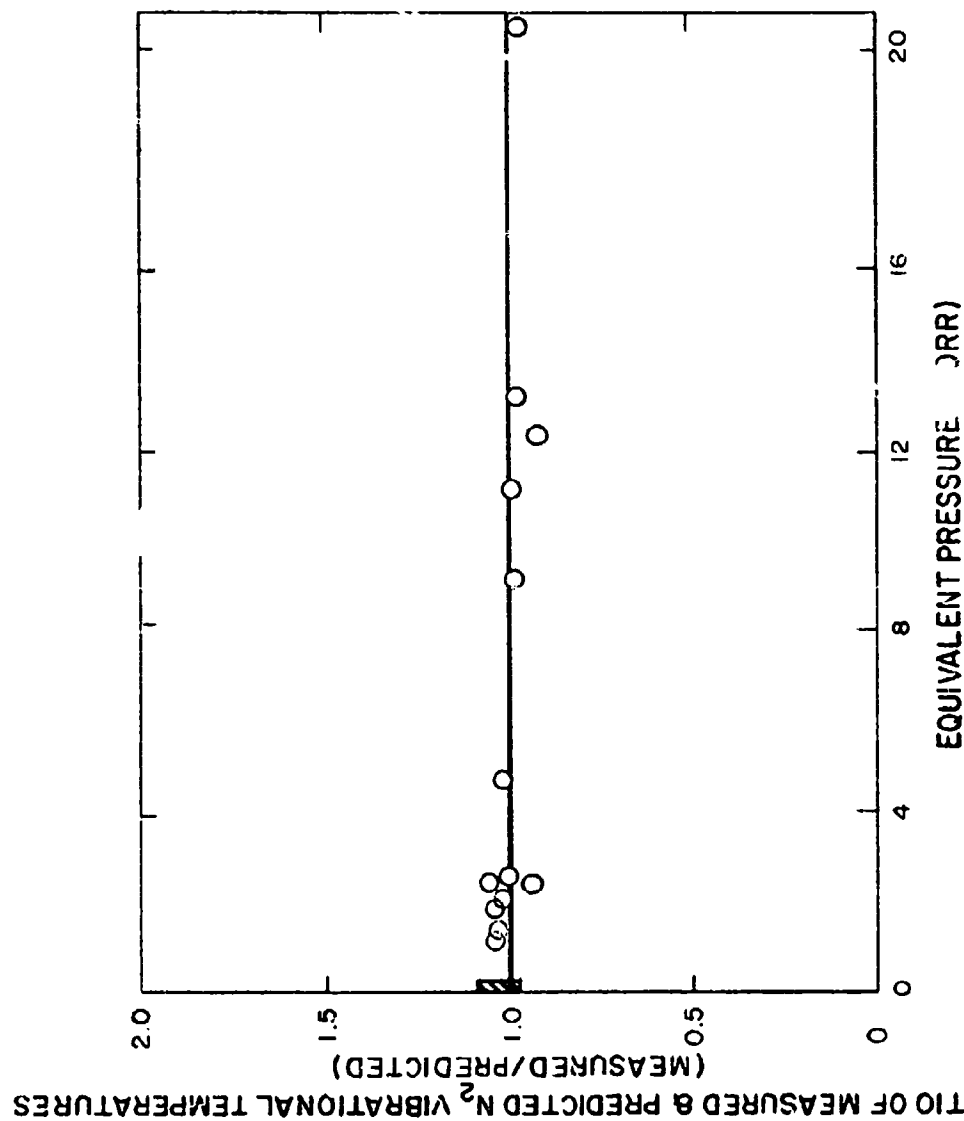


Figure 25. Ratios of measured and predicted N₂ vibrational temperature; O nozzle N1; [shaded rectangle] range of data for nozzle N2 (except second condition of Run 9)

Table IV. Run Summary - Nitric Oxide Data

Run	T _O (K)	P _O (atm)	P (torr)	P _{EQ} (torr)	T _R (N ₂) (K)	T _V (N ₂ ,THEORY) (K)	I _{C4} /I ₁₅
Nozzle N1:							
73	1488	0.942	19.6	10.9	537	1416	1.918
77	2083	0.756	16.4	6.4	776	1880	1.847
79	1561	0.983	74.1	27.3	815	1472	1.989
81	1654	0.997	2.41	2.22	325	1547	2.088
85	2063	0.687	4.29	2.64	487	1870	2.068
86	1572	1.041	6.51	4.66	418	1487	2.119
	2121	0.670	4.20	2.52	500	1909	1.964
87	1807	0.671	39.5	13.5	939	1704	1.645
	1392	1.024	59.0	26.1	754	1331	1.835
88	1973	0.672	2.23	1.56	452	1817	1.700
	1616	1.048	3.38	2.42	419	1510	2.035
Nozzle N2:							
3	4053	1.012	0.199	0.140	425	3400	1.869
	3155	1.019	0.138	0.138	437	3450	1.681
5	2949	0.609	0.114	0.119	289	2730	2.052
	2986	0.614	0.115	0.118	294	2750	2.064
6	3679	0.704	0.137	0.108	380	3240	2.027
	3770	0.707	0.137	0.106	388	3280	2.108
7	3680	0.753	0.146	0.116	379	3220	1.968
	3725	0.755	0.147	0.115	384	3240	1.752

Table IV. Run Summary - Nitric Oxide Data (Continued)

Run	T _O (K)	P _O (atm)	p (torr)	P _{EQ} (torr)	T _R (N ₂) (K)	T _V (N ₂ , THEORY) (K)	I ₀₄ /I ₁₅
Nozzle N2: (Continued)							
8	3732	0.982	0.191	0.149	385	3230	1.766
	3778	0.992	0.193	0.148	391	3260	1.732
9	3592	0.910	0.176	0.143	368	3160	1.953
	3592	0.911	0.176	0.143	368	3160	1.917
10	3427	0.746	0.143	0.124	347	3050	2.010
	3427	0.746	0.143	0.124	347	3050	2.030
	3514	0.769	0.148	0.124	358	3100	1.939
12	3336	0.760	0.145	0.129	339	3000	2.173
	3302	0.756	0.144	0.130	332	2990	2.180
13	3541	1.052	0.203	0.169	360	3110	2.046
	3585	1.057	0.204	0.167	366	3140	1.933

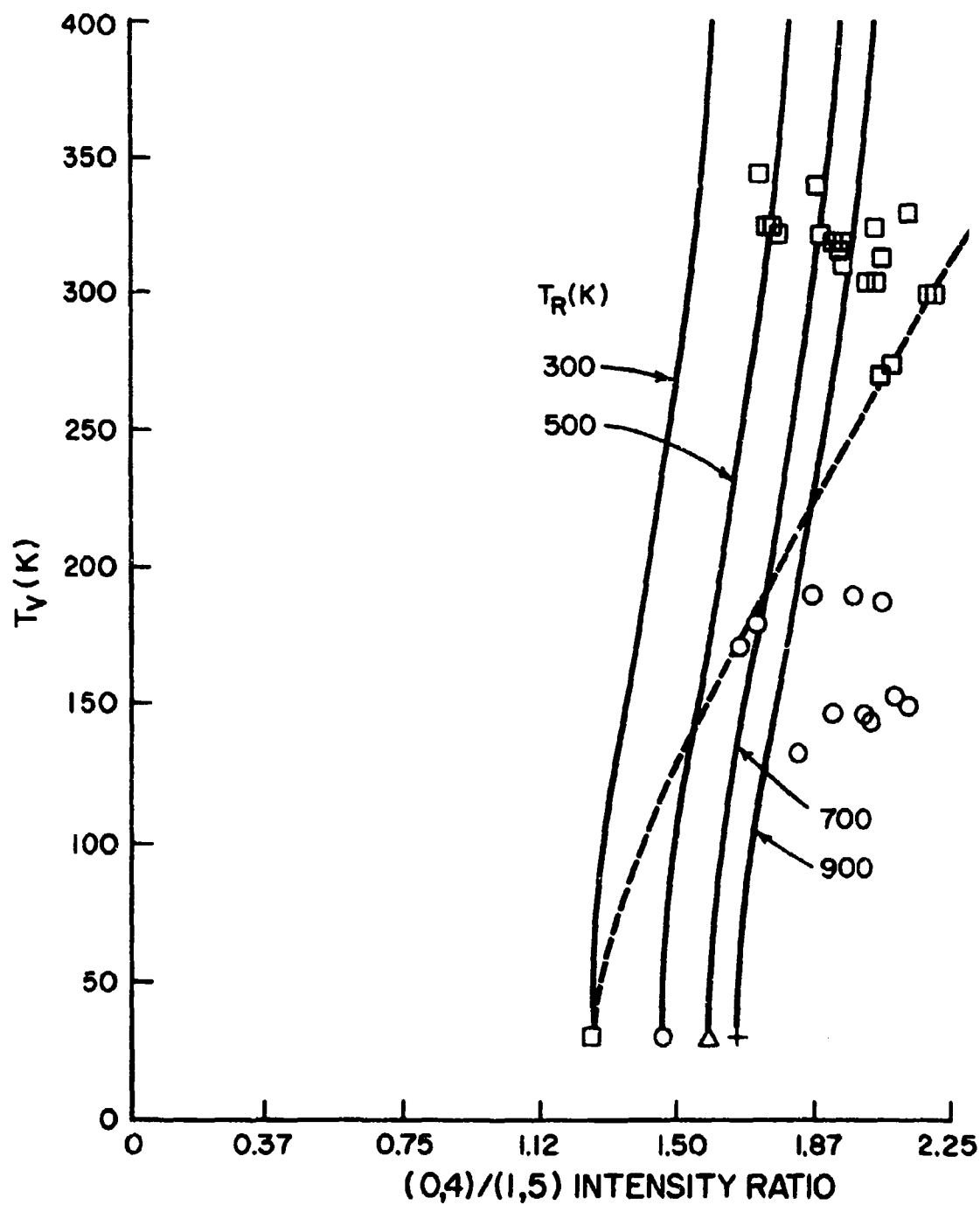


Figure 26. Comparison of measured and predicted band profiles for NO γ (0,4) and (1,5) bands; --- direct excitation; — vibrational relaxation model; \circ nozzle N1; \square nozzle N2.

from the vibrational relaxation model. This scaling has been discussed previously with reference to Fig. 7 and is equivalent to non-dimensionalizing the measured intensities by their room-temperature values.

The direct excitation model (unscaled) greatly under-estimates the band intensity ratios at all run conditions. Hence, the effects observed in the static chamber are repeated even when high gas velocities are present within the beam excitation region.

The band intensity ratios scaled by their room temperature values obtained with nozzle N1 under high density conditions are under-estimated by the vibrational relaxation theory. However, the agreement between the theoretical and experimental ratios at the lower density conditions of nozzle N2 is much better. In this case, the direct excitation model gives as good a representation of the scaled ratios as does the vibrational relaxation model.

The percent difference between the theoretical and experimental band intensity ratios are plotted in Fig. 27 against the rotational temperature. It has been assumed that the N_2 and NO rotational temperatures are equilibrated and are equal to the translational temperature. Except for a few isolated points, a definite trend in the difference is evident in Fig. 27. In addition, there is no apparent effect of the gas density level on the differences between the theoretical and experimental ratios of band intensities shown in Fig. 27. The correlation of the difference with rotational temperature indicates that the theoretical model does not give the correct intensity distribution for the rotational lines within the bands. This can be observed more clearly in the comparative band profiles of Fig. 28.

The most notable difference between the experimental profile and that obtained with the relaxation model shown in Fig. 28 is that the experimental results display a larger amount of energy at high rotational quantum numbers in both bands. This energy is sufficient to introduce measurable overlap of the (0,4) band with the (1,5) band. The inapplicability of the direct excitation-emission model is also evident in Fig. 28.

The difference between the theoretical and experimental band profiles are not large considering the assumptions employed in the theory. The transition probability $(C_k/C_a)k_{10}$ is determined from room-temperature, static calibrations and the results are applied to flows with varying rotational and vibrational temperatures. As seen in Fig. 28, the model appears to give a good representation of the relative band intensities. However, the failure of the model to adequately describe the distribution of intensities within the bands is symptomatic of the omission of an important excitation or de-excitation mechanism.

Since the γ bands result from resonant transitions, self-absorption of the emitted radiation may provide an important means of excitation.

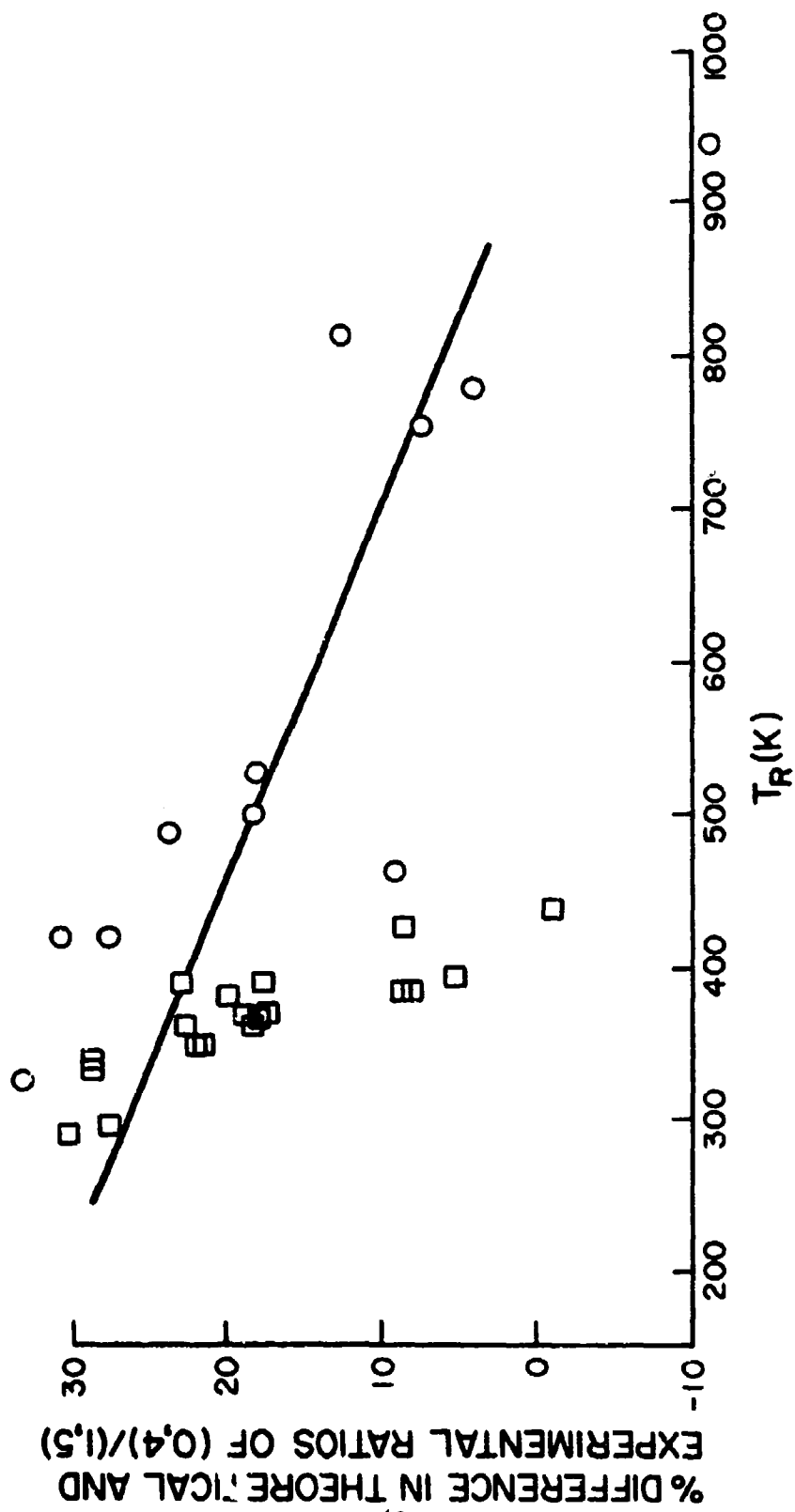
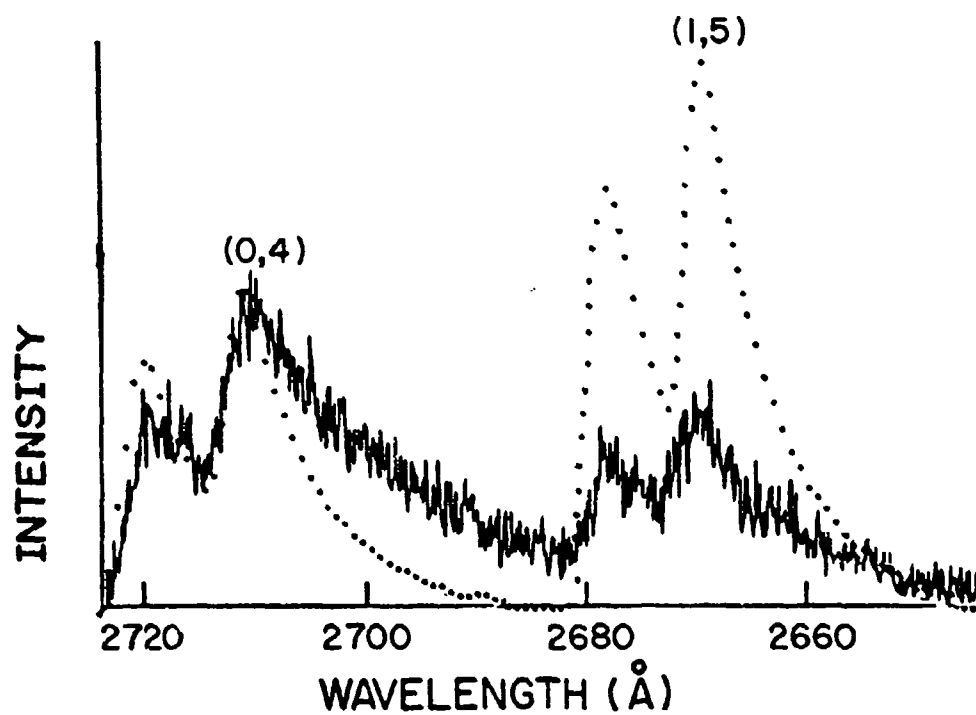
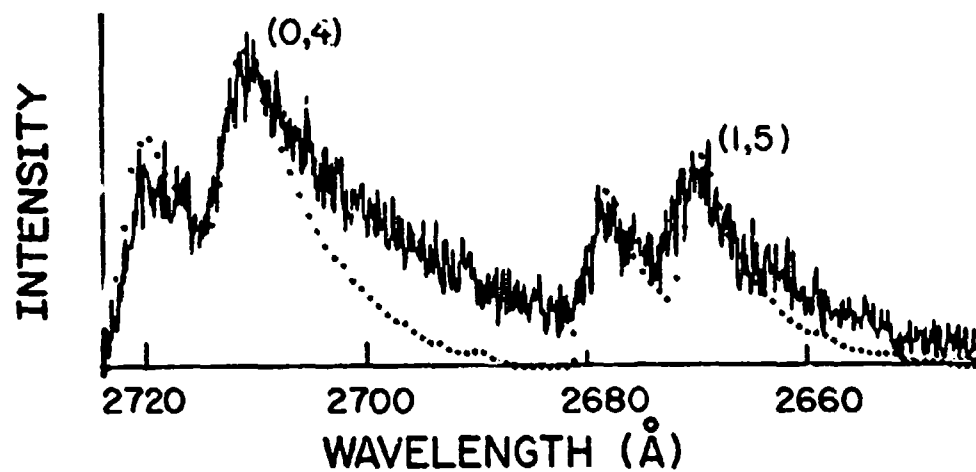


Figure 27. Percent difference in theoretical and experimental intensity ratios for the NO γ (0,4)/(1,5) bands; \circ nozzle N1; \square nozzle N2.



a) Direct Excitation Theory



b) Vibrational Relaxation Model

Figure 28. Comparisons of measured and predicted band profiles for NO γ (0,4) and (1,5) bands.
theoretical; ——— experimental;
 $T_R = 437$ K, $T_V = 3450$ K.

The studies of Ref. 5 show for bands other than those involving the ground vibrational energy level in the $^2\pi$ state that self-absorption will not alter the emitted radiation intensities. However, the cumulative effects of self-absorption in providing a path for excitation to the $^2\Sigma^+$ may be significant. This effect can be modeled in a crude way by expressing the rate of excitation to a particular vibrational energy level in the $^2\pi$ state as

$$\phi(v') = n_e v_s n_g Q_0(v_e) X_{NO} + h\nu^3 A n^* R(n^*, X_{NO}) \quad (31)$$

where n^* is the number density of excited species in the v' level of the $^2\Sigma$ state, $R(n^*, X_{NO})$ is the rate of reabsorption by ground state NO of photons emitted in fluorescence, and all other terms have meanings as previously defined. The radiation intensity resulting from this excitation can be written as

$$\frac{I_0}{I} = 1 - R(n^*, X_{NO})/n^* A \quad (32)$$

where I_0 is the intensity in the absence of absorption.

Melton and Klemperer³⁰ show that

$$R(n^*, X_{NO})/n^* A = \frac{\sum_i \frac{A_i}{A} (k_i p_{NO} t/2)^{1.2}}{0.33 + (k_i p_{NO} t/2)^{1.2}} \quad (33)$$

Eq. (33) is formulated for population of a single rotational energy level and the index i runs over all branches in the band originating from the level. (A_i/A) is the fraction of photons emitted in the i -th branch of the $(v', 0)$ band.

The analysis leading to Eq. (33) applies only when the gas can be considered as an infinite slab of thickness t with atomic line radiation (rather than band radiation) normal to the slab. The quantity k_i is the absorption coefficient of the i -th branch and p_{NO} is the NO partial pressure. Ref. 30 gives estimates for $R(n^*, X_{NO})$ which show that in pure NO at a few tenths of a torr the intensity can be increased by as much as 60% by self-absorption.

Inclusion of self-absorption in the analytical model of the excitation-emission process requires terms similar to that of Eq. (33) for each rotational line in the NO spectrum. Further, a realistic representation of the intensity distribution within the electron beam would be required to adequately describe the absorption process. If such a theoretical model could be developed, it might not only describe the intensity distributions within the bands but might also eliminate the need to include upper-state vibrational relaxation to account for the observed relative band intensities.

5. Molecular Oxygen Results

Comparative scan of the spectral region near the $O_2^+(3,3)$ and $(4,3)$ bands obtained from the wind tunnel and static chamber tests are shown in Fig. 29. The wind tunnel data from nozzles N1 and N2 were obtained at equivalent pressures of 4.20 torr and 0.14 torr, respectively. The static chamber data were obtained at a pressure of 0.40 torr in pure O_2 .

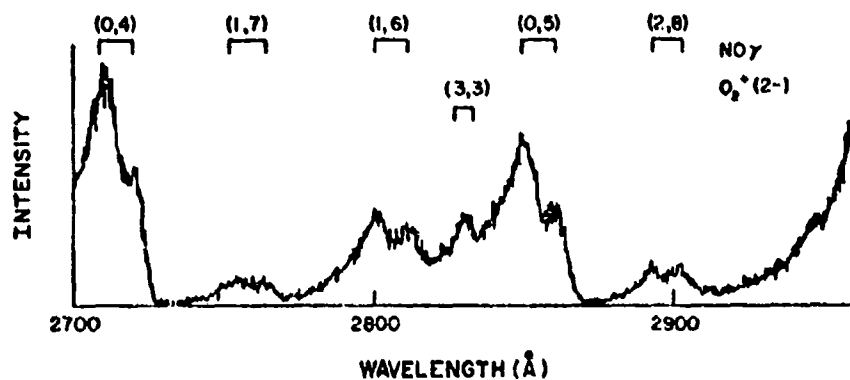
At the high density conditions of nozzle N1, the $O_2^+(3,3)$ band is completely overlapped by the $NO \gamma (0,5)$ and N_2 second positive $(3,0)$ bands. However, at the low density conditions of nozzle N2, the overlap is much less severe. In fact, in the region near the $O_2^+(3,3)$ band the low density wind tunnel data resemble very closely that obtained in the static chamber with pure O_2 .

The variation of the overlap of the O_2^+ bands with changing density indicates that the O_2^+ radiation is quenched more effectively than is the $NO \gamma$ radiation as the density increases. To investigate this effect in more detail, a series of sensitivity experiments was conducted in the static test chamber. It was determined that the minimum beam current-equivalent O_2 pressure product for measurable intensities in the $O_2^+(4,3)$ band is approximately 0.1 torr-mA, ignoring any effects of collision quenching.

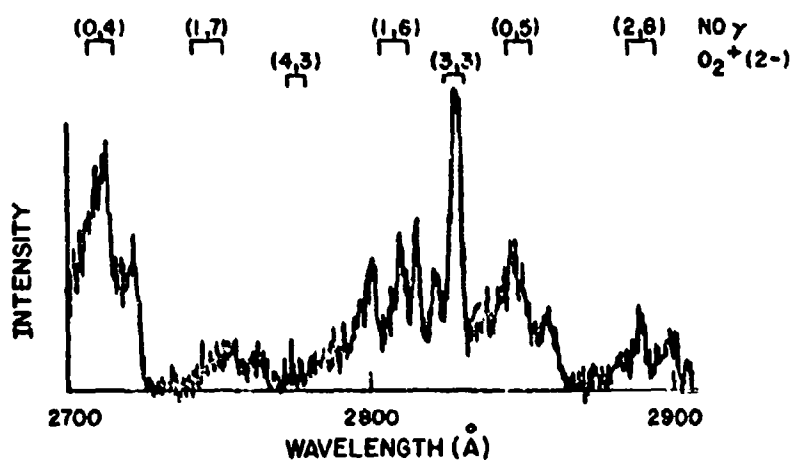
The $(4,3)$ band is observable only in the static chamber data. In the high density data, it is completely overlapped by the tail of the $NO \gamma (1,6)$ band. However, for the high density wind tunnel conditions of Fig. 29, the current- O_2 pressure product was 0.26 torr-mA. Since this value is well above the quenching free sensitivity level of 0.1 torr-mA, the absence of detectable O_2^+ radiation in the $(4,3)$ band indicates that the O_2^+ system is highly quenched at the higher density levels. In fact, the $NO \gamma$ bands are so much more intense than the O_2^+ bands that it is difficult to separate the O_2^+ bands from the overlapping $NO \gamma$ radiation.

The $O_2^+(4,3)$ band also could not be observed in the low density wind tunnel data. However, the O_2 concentration in the low density data was approximately $1.6 \times 10^{14} \text{ cm}^{-3}$ ($p_{O_2} = .007 \text{ torr}$) giving a current- O_2 pressure product of approximately .07 torr-mA; hence, the absence of observable radiation in the $O_2^+(4,3)$ band in these wind tunnel experiments agrees with the results of the sensitivity analyses.

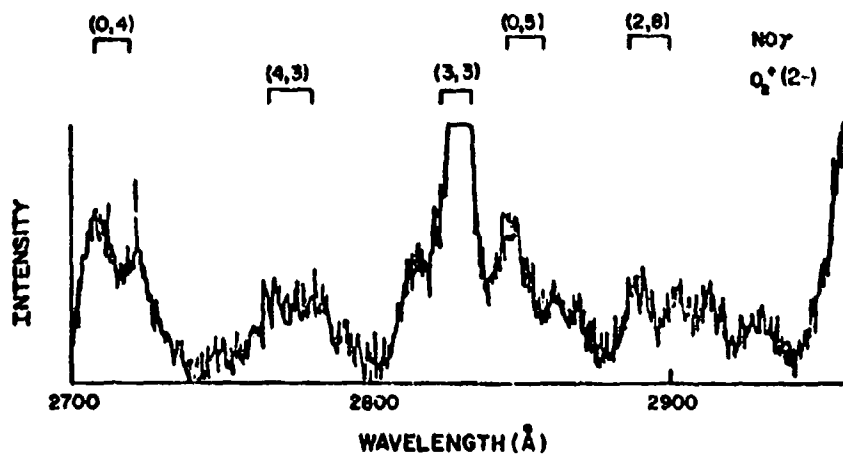
The radiation in the O_2^+ second negative bands at the low density wind tunnel conditions was clearly distinguishable from the other band systems present in the spectrum. In addition, the radiation intensities



a. Nozzle N1; $N_{O_2} = 2.4 \times 10^{16} \text{ cm}^{-3}$.



b. Nozzle N2; $N_{O_2} = 1.5 \times 10^{14} \text{ cm}^{-3}$.



c. Static chamber, $N_{O_2} = 1.3 \times 10^{16} \text{ cm}^{-3}$.

Figure 29. Spectral scans for wind tunnel and static chamber conditions.

agreed with those reported earlier^{7,8}. At the high density conditions of nozzle NI ($p_{\text{NO}} > 2.0$ torr), the severe overlap of the O_2^+ bands by the NO γ bands precludes use of the O_2^+ system for measuring O_2 temperatures and densities with the spectral resolution of these studies (0.2\AA max) and electron beam currents at least up to 10 mA.

C. BEAM SHAPE

An important concern in utilizing an electron beam is the spatial extent of the luminescence. For density measurements it is imperative that the entire beam be viewed at a given location along the beam so that calibrations of intensity vs. density at a known beam current can be applied. As the beam spreads with increasing density and beam length, the spatial resolution of density measurements will degrade. For temperature measurement, there is no need to view the entire beam cross-section. The spatial resolution is limited only by the volume viewed by the optical system. However, as the beam spreads, the intensity of the luminescence within a volume of fixed size decreases. Hence, for temperature measurements the main effect of beam spread is to reduce the signal-to-noise ratio of the measuring system.

The shape of an electron beam is determined by the interaction of many complex phenomena, particularly at high densities. For very low densities and short path lengths, the beam electrons can be assumed to suffer only one collision as they traverse the field of interest. Theoretical analyses of this single scattering phenomena can be conducted and are discussed in Ref. 1. As the gas density is increased, both multiple and plural scattering occur and gas focusing effects must be considered.

Low energy ions, created by the primary excitation process, can be trapped within the potential well of the beam. These ions can reduce the space charge repulsion effects within the beam and lead to phenomena generally termed gas focusing. Secondary electrons are also created by the excitation process and their presence within the beam and the surrounding region may have a marked effect on the beam shape. The secondary electron concentration has been estimated by Harbour, et al,³¹ and rather large electron number densities were predicted at certain operating conditions. Magnetic pinch effects are also possible, although these are expected to be weak for electron energies typical of beams used for diagnostic purposes.

Gas focusing and scattering of the beam electrons within the beam generator further modify the beam shape in the test gas. Most beam generators employ a small exit orifice for the electrons to pass from the generator into the test gas. A dynamic pumping system is employed to maintain the generator region at a sufficiently low pressure (e.g., less than 10^{-4} torr). As the test gas pressure is raised, scattering of the electrons within the generator occurs. The effects of this scattering are cancelled, in part, by adjusting internal deflection and

focus control systems to maximize the beam current within the test gas. At high densities, maximization of the beam current can have large influences on the electron trajectories through the generator and in the test gas.

Reliable analytical models of the structure of the beam-generated plasma within the test gas are not available because of the extreme complexity of the region. Estimates of electron trajectories must include the effects of focusing and scattering within the beam generator, in addition to the mechanisms active in the high density test region. Empirical correlations of the beam shape must generally be used to describe the variations of beam size with gas density, accelerating voltage, and path length.

Some guidance in developing empirical correlations can be obtained from the results of multiple and plural scattering theories summarized in Ref. 1. The scattering can be characterized in terms of the mean number of scatterings, Ω , occurring in a length L of gas with a number density of n_g , a mass m and an atomic number of Z . The mean number of scatterings is given by¹

$$\Omega = 2.5 \pi Z^{1/3} (Z + 1) n_g L h^2 / m^2 v_e^2 \quad (34)$$

where v_e is the electron velocity. Data summarized in Ref. 1 show that the angle subtended at the beam origin, θ , by one-half of the characteristic lateral spread of an electron beam in air and nitrogen can be represented over most of the range of the data by

$$\theta = c \Omega^a \quad (35)$$

where c and a are empirical constants.

Camac³² gives correlations of the beam width at the half-intensity point, $W_{1/2}$, for a 100 keV beam as

$$W_{1/2} = .044 \left[\frac{pL^3}{(v_e/1000)^2} \frac{300}{T} \right]^{1/2} \quad (36)$$

where p is in torr, L in cm, v_e in kV, T in K, and $W_{1/2}$ in mm. This can be put in the form of Eq. (35) by observing that the angle θ is approximately $(W_{1/2}/2L)$. Hence, in mks units, Eq. (36) becomes

$$W_{1/2}/L = 6.6 \times 10^{-3} [pL/v_e^2 T]^{1/2} \quad (37)$$

or, combining Eqs. (34) and (37) for air,

$$W_{1/2}/L = .16 \sqrt{\Omega} \quad (38)$$

Camac includes data only for a beam accelerating potential of 100 kV and there are insufficient data to judge the goodness of fit of Eq. (36).

Wallace¹³ gives correlations of $W_{1/2}$ for a 40 keV beam at test gas pressures of .85 and 1.6 torr. Although the spatial resolution of these measurements was relatively poor for determining beam shape, that portion of the data for which the beam size was larger than the area viewed by the optical system agreed reasonably well with the correlation of Eq. (36).

Detailed experiments were conducted in the static chamber to determine the form of the variation of $W_{1/2}$ over a wide range of pressure, beam voltage, and beam path length. The accelerating voltage was varied from 20 to 40 kV with air pressures from 0.2 to 30 torr. The width of the half-intensity point within the beam was obtained by scanning across the beam with the spectrometer set to view the head of the N_2^+ first negative (0,0) band at 3914 Å. Hence, the half-width data reflect only the radiation from the first negative system; radiation from other systems, particularly the N_2 second positive system, was not included in the beam shape measurements. This will affect the width measurements, but gives data most meaningful in applications of an electron beam to temperature measurements at high densities.

The experimental data are presented as $W_{1/2}/L$ vs. pl/v_e^2 in Fig. 30. In this form, Camac's equation is

$$W_{1/2}/L = .7[p_e(\text{torr})L(\text{in.})/v_e^2(\text{kV})]^{1/2} \quad (39)$$

where p_e should be interpreted as equivalent pressure. The fit of Eq. (39) to the data of Fig. 30 is relatively poor, due primarily to the initial beam size.

The form of Eq. (39) can be justified in terms of multiple scattering theory when $W_{1/2}/L$ is taken as a measure of the angle of the beam electrons. When the beam spreading is small, a better measure of the angle of the electrons can be obtained by examining the change in the half-width as the beam transverse the test gas. Accordingly, the half-width of the beam at the exit orifice was subtracted from the measured half-width. The data are presented in the form $(W_{1/2} - W_0)/L$ vs. pl/v_e^2 in Fig. 31, where W_0 is the minimum beam half width.

Equation (39) is seen to give a much better representation of the beam shape when it is applied in terms of the change in beam width. The scatter in Fig. 31 results from the complex interaction of the phenomena causing beam spreading which cannot be represented by a simple scattering theory. In addition, the effects of flow on the beam shape have not been included either in the development of the correlation from scattering theory or in the experimental measurements. The gas flow will remove both ions and secondary electrons from the beam region, changing the focusing effects observed in the static case. However, the correlation of Eq. (39) is adequate for estimating the beam size in air and nitrogen test gases for both static and flow conditions.

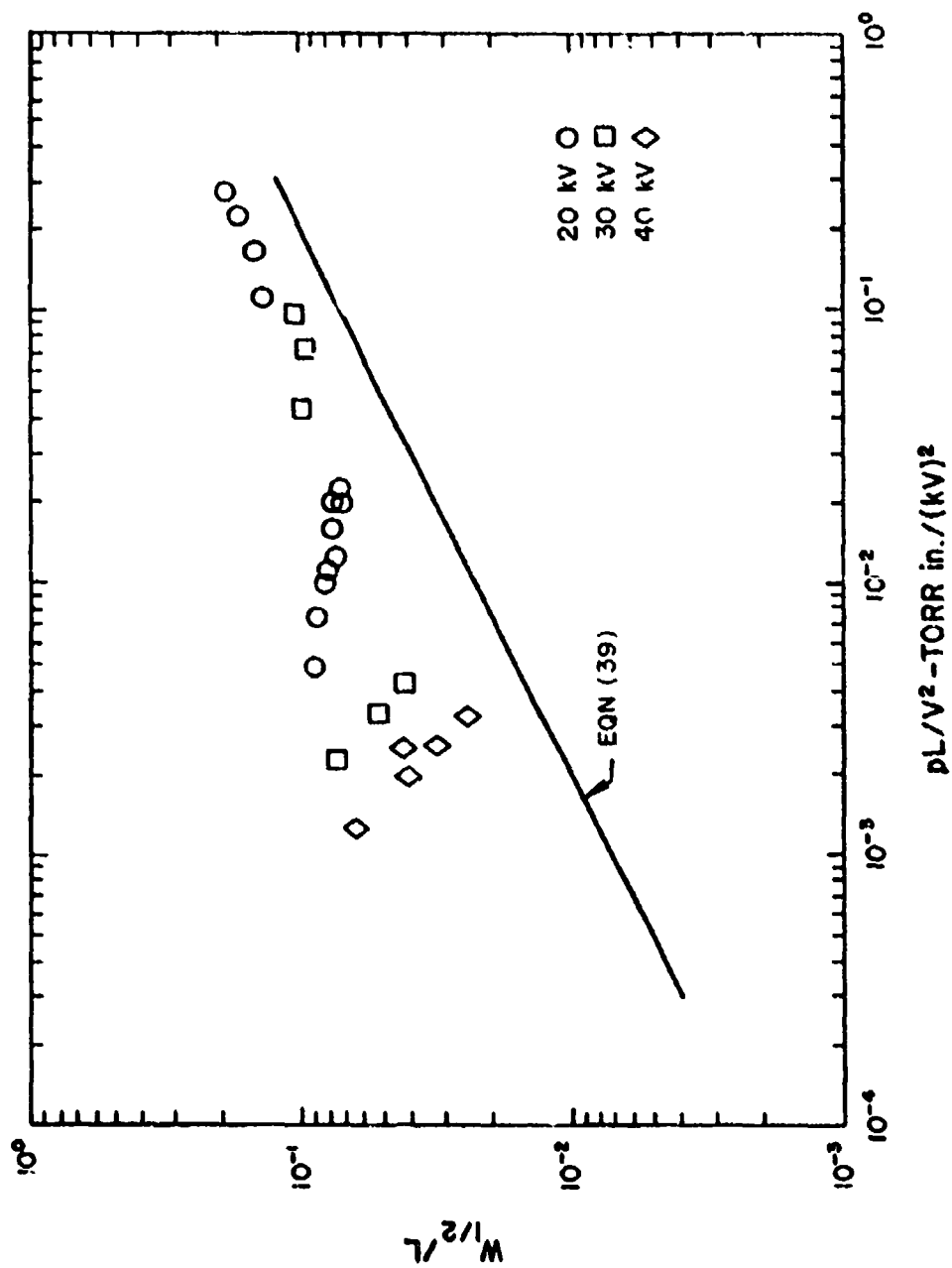


Figure 20. Correlations of beam half-width

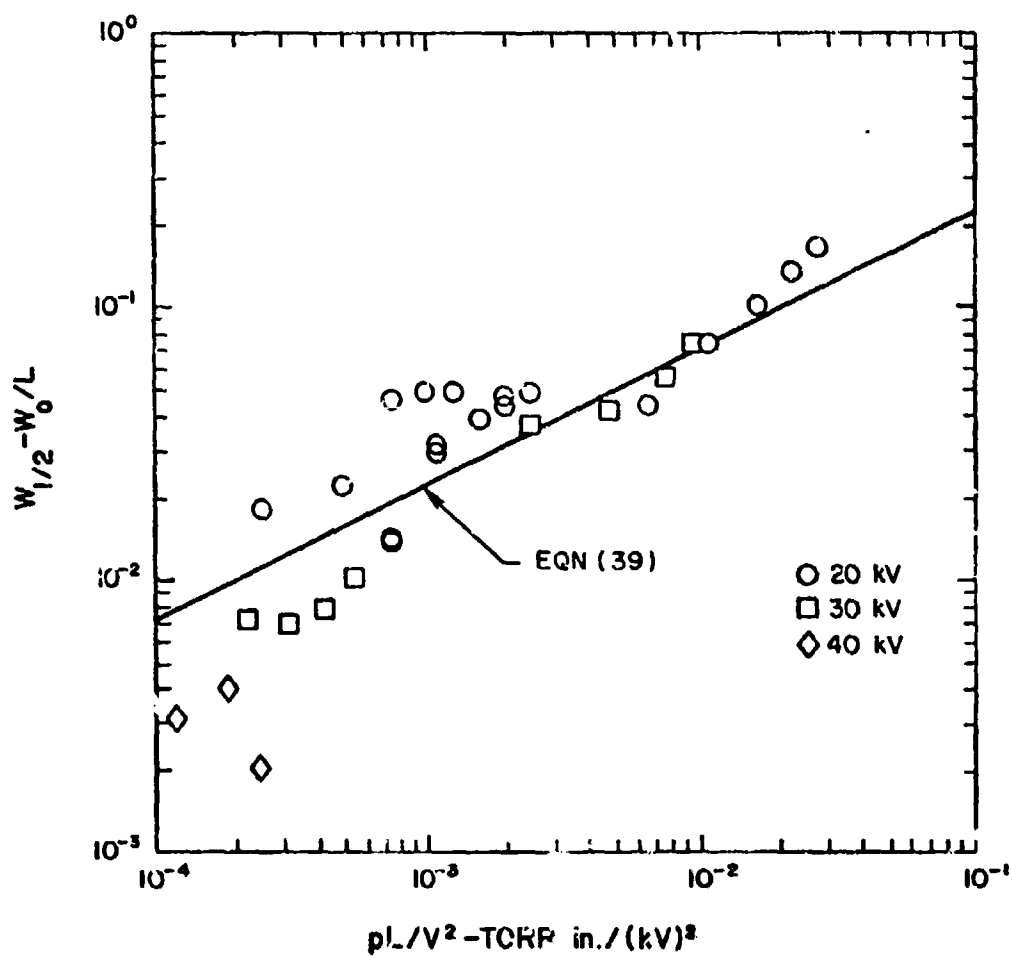


Figure 31. Correlation of beam half-width increment;
 W_0 = initial beam half-width

V. EFFECTS ON PREVIOUS MEASUREMENTS

The studies discussed here were motivated, in part, by certain disparities in predicted and measured nitric oxide number densities and vibrational temperatures in previous tests conducted in the AFFDL Electrogasdynamic Facility (EGF). It was suspected that these disparities might result from inapplicability of the usual excitation-emission model used to interpret the measurements⁶. A summary of the previous data obtained in the EGF is given in Table V. The tests conducted here with nozzle N2 simulated the conditions obtained in the EGF with the 19 inch nozzle. Evaluations of the possible effects on the previous data resulting from the present studies are given below.

A. MOLECULAR NITROGEN

The vibrational temperature and number density of molecular nitrogen were measured in the EGF with both the 19 inch and 7 inch nozzles; the N_2 rotational temperatures were measured only in the 19 inch nozzle. As seen in Table V, N_2 rotational temperature data were obtained at equivalent pressures below approximately 0.25 torr. At these equivalent pressures it is well known¹ that N_2 rotational temperature data can be obtained with errors no greater than 5%.

The studies conducted here demonstrate that N_2 vibrational temperatures can be measured at densities at least an order of magnitude greater than those employed in the EGF. Hence, there are no errors introduced in the previous vibrational temperature data due to elevated densities.

The accuracy of the N_2 number densities is directly related to the accuracy of the quenching constants employed to reduce the data⁶; however, since the maximum equivalent pressure in the EGF was approximately 2 torr, relatively large errors (30%) in the quenching constants can be tolerated before errors greater than 10% in the number densities result. Hence, no additional errors in N_2 number densities result from the present studies.

B. MOLECULAR OXYGEN

Data for molecular oxygen were obtained in the EGF only with the 19 inch nozzle where the equivalent pressures were below 0.25 torr. The present studies demonstrate that there are no particular anomalies in the O_2^+ second negative system at these density levels. However, under the high density conditions of nozzle N1 the O_2^+ radiation is completely overlapped by NO γ bands. While oxygen data for the 7 inch EGF nozzle have not yet been obtained, it is likely that radiation systems other than the O_2^+ second negative system will have to be investigated for use in measuring O_2 vibrational temperatures in high density air flows.

Table V. Previous EGF Run Summary

EGF NOZZLE	P _O (psia)	H _O (Btu/lb)	T _O (K)	P _{EQ} (torr)	T _R	N ₂ T _V	NN ₂	O ₂ T _V	NC ₂	NO T _V	NNO	O N _O	REF AFFDL-TR-
19 inch	200 350	7500 3500	7100 4654	0.37 0.34	X X	X X	X						71-161
19 inch	250 350 500	7000 3500 2500	7001 4714 3973	0.09 0.14 0.21	X X X			X X	X X			X X X	73-10
19 inch	250 350 500	6000 3500 2500	6564 4714 3973	0.10 0.14 0.21						X X	X X		74-8
7 inch	250 350 500	6000 3500 2500	6564 4714 3973	0.69 1.25 2.21		X X	X X			X X	X X		74-8

X - Indicates quantities measured

C. NITRIC OXIDE

Nitric oxide vibrational temperature and number density data were collected in the EGF with both the 19 inch and 7 inch nozzles and the data were interpreted with the direct excitation model. While the results of the present studies show that the direct excitation model is not applicable to nitric oxide, the use of the scaled band intensity ratios as previously discussed eliminates the gross error in band intensity ratios introduced with the direct model.

As can be seen in Fig. 26, over the entire density range investigated the scaled band intensity ratios agree as well with the direct excitation model as they do with the vibrational relaxation model. Neither model adequately describes the variation of band intensity ratio with vibrational temperature and excitation/de-excitation mechanisms not presently included in these models may be important. Because of the uncertainties in the models, there is at present no justification for use of one over the other so long as the measured band intensity ratios are scaled by their room temperature values. In all cases, this scaling of the band intensity ratios was employed in Ref. 6 so that further corrections to the data are not warranted.

VI. CONCLUSIONS

A new, systematic study of electron beam induced emission has been conducted at density levels well above those normally used in application of the technique. Emphasis was placed on the fluorescence induced in air flows, since there is much interest in applying the electron beam diagnostic technique to flows generated by arc-heated wind tunnels.

The results of the wind tunnel studies show that the vibrational temperature of molecular nitrogen can be measured with good accuracy at densities at least up to those corresponding to an equivalent pressure of 20 Torr. The high density limit for application of the diagnostic technique to N_2 could not be determined from the present measurements. Studies should be performed at equivalent pressures at least up to 100 Torr to establish this high density limit.

Comparisons of the wind tunnel and static chamber data demonstrate that the static chamber is unsuitable for examining the character of electron beam induced radiation at high density. Accumulation of secondary electrons, low energy ions, and molecules in metastable electronic energy states contribute to the excitation of the ground state molecules. Such low energy particles are not present in meaningful concentrations in flow fields with high velocities. Similarly, the overlap of the N_2^+ first negative system by the N_2 second positive system prevalent in the static chamber, was not observed in the wind tunnel studies.

Since it is known that the second positive system is excited primarily by secondary electrons, this is further indication that results from the static chamber bear little resemblance to those obtained at the same density in the wind tunnel flow field. This is not meant to be a condemnation of all previous static chamber results. The degree of excitation by secondary particles will undoubtedly be a complex function of the mechanical and electrical arrangement of the static test chamber. However, such experiments must be conducted with great care and the data must be carefully analyzed to remove extraneous effects which may not be present in high speed flow fields.

Comparisons of theoretical and measured band intensities for the NO γ system show that the direct excitation model does not lead to the proper relative intensities within a given band sequence. A new theoretical model of the excitation-emission process has been formulated to allow for transitions between vibrational energy levels in the excited electronic energy state of the NO γ system. A relative $v' = 1 \rightarrow v' = 0$ transition probability was determined from static tests and applied to the wind tunnel data. Comparisons of the theoretical and experimental data show that the model properly accounts for the general trend of band intensity ratio with vibrational temperature but that more detailed studies are required to substantiate the validity of the model.

Wind tunnel and static chamber experiments were conducted with the O_2^+ second negative system. At equivalent pressures above 4.0 torr, the observed O_2^+ radiation was severely overlapped by the NO γ system. Sensitivity studies conducted in the static chamber show that the expected O_2^+ radiation intensity was well above the minimum detectable level. The results indicate that the O_2^+ radiation is more severely quenched than is that in the NO γ system. The spectral proximity of the O_2^+ and NO γ bands coupled with the decreased relative intensities of the O_2^+ bands at high density cause the NO γ system to completely overlap the O_2^+ system at the spectrometer resolution required for these experiments.

Beam shape experiments were conducted in a static chamber to establish an empirical correlation of beam half-width with density and acceleration potential. An analysis based on the angle of divergence of the beam leads to an acceptable form of the correlation.

REFERENCES

1. Muntz, E. P., "The Electron Beam Fluorescence Technique," AGARDograph 132, (Dec. 1, 1968).
2. Robben, F. and Talbot, L., Physics of Fluids, 10, 521 (1967).
3. Petrie, S. L., AIAA Journal 4, 1680 (1966).
4. Petrie, S. L., Boiarski, A. A., and Lee, H. F., "Electron Beam Flow Field Analyses in the AFFDL 2-Ft. Electrogas dynamics Facility," AFFDL-TR-71-161, (1971).
5. Petrie, S. L., and Komar, J. J., "Application of Electron Beam Fluorescence Technique to the Measurement of the Properties of Nitric Oxide in Nonequilibrium Flows," AFFDL-TR-72-144, (1972).
6. Petrie, S. L., and Komar, J. J., "Electron Beam Analysis of the Properties of Molecular Nitrogen and Nitric Oxide in the AFFDL 2-Ft. Electrogasdynamic Facility," AFFDL-TR-74-8, (1974).
7. Petrie, S. L., Boiarski, A. A., and Lazdinis, S. S., "Electron Beam Studies of the Properties of Molecular and Atomic Oxygen," AFFDL-TR-71-30, (April 1971).
8. Petrie, S. L., and Komar, J. J., "Electron Beam Analyses of the Properties of Molecular and Atomic Oxygen in the AFFDL 2-Ft. Electrogas dynamics Facility," AFFDL-TR-73-10, (January 1973).
9. Ashkenas, H., Physics of Fluids, 10, 2509 (1967).
10. Hunter, W. W., paper presented at ISA 21st Annual Conference, New York, Oct. 24-27, (1966).
11. Maguire, B. L., "Density Effects on Rotational Temperature Measurements in Nitrogen Using the Electron Beam Excitation Technique," Rarefied Gas Dynamics, Vol. 2, Academic Press, (1969).
12. Petrie, S. L., "An Electron Beam Device for Real Gas Flow Diagnostics," ARL 65-122, (1965).
13. Petrie, S. L., "Flow Field Analyses in a Low Density Arc-Heated Wind Tunnel," Proc. of the 1965 Heat Transfer and Fluid Mechanics Institute, Stanford University Press, (1965).
14. Sebach, D. I., "An Electron Beam Study of Vibrational and Rotational Relaxing Flows of Nitrogen and Air," Proc. of the 1966 Heat Transfer and Fluid Mechanics Institute, Stanford University Press, (1966).

15. Sebacher, D. I., "A Correlation of N_2 Vibrational, Translational Relaxation Times," AIAA Journal, 5, 819 (1967).
16. Sebacher, D. I., and Guy, R. W., "Vibrational Relaxation in Expanding N_2 and Air," NASA TM X-71988, (1974).
17. Harbour, P. J., private communication, (1967).
18. Herzberg, G., Molecular Spectra and Molecular Structure, I: Spectra of Diatomic Molecules, D. van Nostrand Co., Princeton, N.J. (1964).
19. Churchill, D. R., Hagstrom, S. A., and Landshoff, R. K. M., Journal of Quantitative Spectroscopy and Radiative Transfer, 4, 291 (1964).
20. Deezi, I., Acta Physica, 9, 125 (1959).
21. Clarke, J. F. and McChesney, M., The Dynamics of Real Gases, Butterworths (1964).
22. Pearse, R. W. B., and Gaydon, A. G., The Identification of Molecular Spectra, John Wiley and Sons (1963).
23. Mitchell, A. C. G. and Zemansky, M. W., Resonance Radiation and Excited Atoms, Cambridge Univ. Press (1971).
24. Petrie, S. L., Pierce, G. A., and Fishburne, E. S., "Analysis of the Thermochemical State of an Expanded Air Plasma," AFFDL-TR-64-191, (1965).
25. Hickman, I. S., AFOSR 66-2509, (1966).
26. Lordi, D. A., Mates, R. E., and Moselle, J. R., "Computer Program for Numerical Solution of Nonequilibrium Expansions of Reacting Gas Mixtures," NASA CR-472, (1968).
27. Glowacki, W. J., and Anderson, J. D., "A Computer Program for CO_2 - N_2 - H_2O Gas Dynamic Laser Gain and Maximum Available Power," NOLTR-71-210, (1971).
28. Anderson, J. D., "The Effect of Kinetic Rate Uncertainties on Gasdynamic Laser Performance," AIAA Paper No. 74-176, (1974).
29. Sebacher, D. I., Guy, R. W., and Lee, L. P., "Vibrational Energy Transfer in Expanding Mixtures of N_2 and CO_2 as Measured By an Electron Beam," NASA TN D-6445 (Sept. 1971).
30. Melton, L. A. and Klemperer, W., Planet Space Sci. 20, 157 (1972).
31. Harbour, P. J., et al., Physics of Fluids 11, 4, 800 (1968).

32. Camac, M., "Boundary Layer Measurements With An Electron Beam," AVCO Research Rept. 275 (1967).
33. Wallace, J. E., "Hypersonic Turbulent Boundary Layer Measurements Using An Electron Beam," Cornell Aero Lab Rept. AN-2112-Y-1, (1968).